THE MEASUREMENT OF RAMAN OPTICAL ACTIVITY

A dissertation submitted to attain the degree of

DOCTOR OF SCIENCES of ETH ZURICH
(Dr. sc. ETH Zurich)

presented by

CARIN RAE LIGHTNER

MSc., Cornell University

born on 06.03.1991

accepted on the recommendation of:

Prof. Dr. David J. Norris (ETH Zurich), examiner
Prof. Dr. Romain Quidant (ETH Zurich), co-examiner
Prof. Dr. Christian Johannessen (University of Antwerp), co-examiner
Dr. Jessica Wade (Imperial College), co-examiner

2022

Dedicated in loving memory to Barbara and Archie Lightner.

I think of you both every time I see something beautiful.

ABSTRACT

The use of light to understand the world around us is one of oldest areas of science. Called spectroscopy, the measurement of light-matter interaction has led to the elucidation of everything from the structure of atoms to the composition of our atmosphere. And yet, mysteries still remain. One, great unsolved question relates to the origin of life on earth, and the propensity of all biological molecules (amino acids, sugars, DNA) to prefer a certain structure, called chirality.

Chiral molecules are those which exist in two forms which are mirror images of one another but non-superimpossable. This class of molecules accounts, almost exclusively, for the molecules that make up life. And curiously, they prefer one chiral version over the other. The origin of this preference, and whether it is a prerequisite for life, or just a molecular twist of fate, is a field of active study. To better understand chirality, spectroscopy techniques to study it are essential. This thesis focuses on one such technique, called Raman optical activity (ROA).

ROA is a spectroscopy technique which gives both the vibrational structure of a material as well as its chirality. ROA has the potential to help unravel the mysterious origins of chirality, and also give detailed information on protein secondary structure and binding. However, ROA is a very weak effect requiring high polarization precision. This means that the measurement of ROA remains challenging. The work outlined in this thesis is focused on improving the measurement of ROA through advancement in instrumentation, improved understanding of polarization artifacts, and the potential use of surface-enhancement to increase the ROA signal. Finally the application of ROA to study biological materials with the newly developed instrument is demonstrated. With the advances outlined here, and additional progress in the field, ROA can finally fulfil is potential as a tool to help scientists understand the origin and function of chirality in life.

ZUSAMMENFASSUNG

Die Nutzung des Lichts um die Welt um uns herum zu verstehen ist einer der ältesten Bereiche der Wissenschaft. Die Messung der Wechselwirkung zwischen Licht und Materie, die so genannte Spektroskopie, hat zur Klärung vieler Fragen geführt, von der Atomstruktur bis zur Zusammensetzung unserer Atmosphäre. Dennoch bleiben immer noch Rätsel. Eine große ungelöste Frage betrifft den Ursprung des Lebens auf der Erde und die Neigung aller biologischen Moleküle (Aminosäuren, Zucker, DNA), eine bestimmte Struktur, die so genannte Chiralität, zu bevorzugen.

Chirale Moleküle sind Moleküle, die in zwei Formen existieren, die Spiegelbilder voneinander sind, aber nicht superimponierbar. Moleküle dieser Klasse machen fast alle Moleküle aus, aus denen das Leben besteht. Noch geheimnisvoller ist, dass sie die eine chirale Form der anderen vorziehen. Der Ursprung dieser Vorliebe und die Frage, ob es sich dabei um eine Voraussetzung für Leben oder nur um eine molekulare Fügung des Schicksals handelt, ist Gegenstand aktiver Forschung. Um die Chiralität besser zu verstehen, sind Spektroskopietechniken zu ihrer Untersuchung unerlässlich. Diese Arbeit konzentriert sich auf eine solche Technik, die sogenannte optische Raman-Aktivität (ROA).

ROA ist eine Spektroskopietechnik, die sowohl die Schwingungsstruktur eines Materials als auch seine Chiralität liefert. ROA hat das Potenzial, die mysteriösen Ursprünge der Chiralität zu entschlüsseln und detaillierte Informationen über die Sekundärstruktur und Bindung von Proteinen zu liefern. Allerdinges ist ROA ein sehr schwacher Effekt, der eine hohe Polarisationspräzision bei sehr geringem Signal erfordert. Dies bedeutet, dass die Messung von ROA eine Herausforderung bleibt. Diese Arbeit konzentriert sich auf die Verbesserung der Messung von ROA durch Fortschritte in der Instrumentierung, ein besseres Verständnis der Polarisationsartefakte und den möglichen Einsatz von Oberflächenanreicherung zur Erhöhung des ROA-Signals. Schließlich wird die Anwendung von ROA zur Untersuchung biologischer Materialien mit dem neu entwickelten Instrument demonstriert. Mit den hier skizzierten Fortschritten und weiteren Fortschritten auf diesem Gebiet kann ROA endlich sein Potenzial als Instrument zum Verständnis des Ursprungs und der Funktion der Chiralität im Leben ausschöpfen.

ACKNOWLEDGEMENTS

The journey to writing this thesis has been a long one and the list of those to thank is even longer. I will start with thanking Prof. Dr. David Norris for accepting me into his lab and for giving me the freedom to pursue my own topic as well as our many scientific and non-scientific discussions and debates over the last few years. Thanks also to Prof. Dr. Romain Quidant, Prof. Dr. Christian Johanessen and Dr. Jess Wade for serving on my committee. Also Pascale Bachmann, for all of her help behind the scenes making sure everything runs smoothly (especially since I always seem to require a bit of extra paper work!). I also owe my thanks to Philippe Knuessel first for introducing me to David and OMEL, and later for being a sounding board for all things legal-related.

My thanks to Stefan Meyer, not only for helping me with many technical aspects of the ROA build, but also for working together exploring some of the options for the future of ZROA. Thanks to Henar for so much help in the wetlab and also the many coffee-chats and encouragement over the last years. My fellow chirality enthusiast and doctoral student Robert, was always game for a good discussion about parity, time reversal and the merits of achromatic vs. zero order half wave plates and also has read through and revised sections of this thesis. Thanks to Felipe and Raphi for looking through my set-up with me during the long years before it was working and helping me brainstorm new things to try. Thanks to Ann-Katrin for many coffees, discussions, interesting side projects together and encouragement. My office mate Sergio has been a constant source of discussion, ideas and Italian swear words these last four years: thanks for all three! I have to especially thank Alex, for being a friend and support and also for reading and revising a section of this thesis. Andrew also read and revised a section and has patiently answered all of my chemistry related questions. I would also like to thank Hannah Niese, for being a great student (and adapting to a COVID friendly project!) and for all of her illustration help with the table of content images for Chapters 2 and 3. Also a huge thank you to Valentina for patiently learning to use the ROA and working together on the hydrogels in Chapter 4. Also Julia, Fabian, Jonas, Stefan and Clemens for working with me as students and each teaching me how to be a better supervisor. Overall I have to thank all of the current and past members of OMEL for making a great environment to work and learn in during my doctoral studies.

This project would not have been possible without the support of Daniel Gisler and his coworkers at IRSOL and SUPSI. Daniel has patiently worked with me these many years to keep first ZIMPOL II and now ZIMPOL III running smoothly at OMEL and also to teach me how to use and interpret results from the camera. Thank you Daniel for giving me (and ROA) a chance, working with you and learning also about the original uses of ZIMPOL in solar physics has truly been one of the

CONTENTS

NOTATION

1

INTRODUCTION

Freedom is never very safe.

— Ursula K. LeGuin

Every day, we use light to understand the world around us. The color of the sky at dawn hints at the weather for the day, a traffic light tells us to stop or slow down, and the color of our tea indicates when its ready for drinking. In science, we call this process of getting information from light– spectroscopy. In the lab, chemists use spectroscopy to play molecular detective and determine the chemical components in reaction products. Spectroscopy is used to study everything from astronomy and explosives detection to early diagnosis of Alzheimer's. [1–3]

The beginning of "modern" spectroscopy is perhaps as early as 1666, when Newton began his study on the origin of colors. Using a glass prism, Newton was able to separate sunlight into its component colors. [4] Additional work by Fraunhofer, Kirchoff and Bunsen led to the startling realization that the lines in the solar spectrum are related to the chemical elements that made up the sun. And so, even early in its history, the science of spectroscopy became quickly intertwined with understanding the details of the composition of atoms and elements.

Despite the early use of spectroscopy in discerning the structure of atoms, it wasn't until the early 20th century that the phenomena of light scattering was studied in detail. The scientists Mie, Rayleigh and Raman all studied different aspects of light scattering and are now known by the effects that bear their names. [5] Even today, new spectroscopy techniques are still being discovered and developed.

The development of new types of spectroscopy gives scientists more tools to extract information from light. This thesis reports the investigation into the measurement of a type of spectroscopy called Raman optical activity (ROA). The aim of this introduction is to give the reader the necessary information needed to understand the basic motivation of this thesis, while also keeping it relatively brief. The interested reader is directed to *The*

Raman Effect by Derek Long and *Molecular Light Scattering and Spectroscopy* by Laurence Barron for further detail. [6, 7]

1.1   LIGHT-MATTER INTERACTION

Light exists both as a particle (photon) and co-propagating and perpendicular electric and magnetic waves, as shown in Figure 1.1.
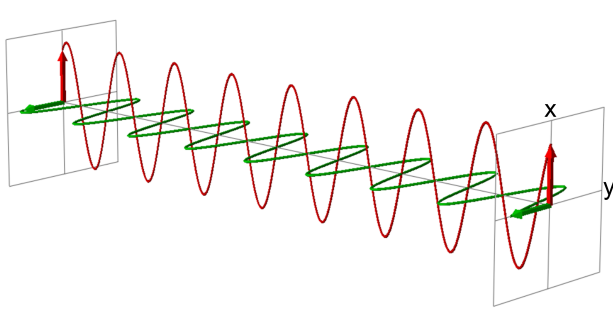
FIGURE 1.1: Illustration of light as the combination of the electric (red) and magnetic (green) waves propagating in time and space. Figure adapted from: [8]

Mathematically, light can be defined as shown in Eq. 1.1 and Eq. 1.2 as plane waves propagating in the z-direction. [9] The angular frequency (ω) is defined as $\omega = 2\pi f$, where f is the linear frequency defined as oscillations in a given time, k is the wave number or propagation constant defined as 2π over the wavelength (λ), $k = (2\pi)/\lambda$ and ϕ is the phase factor.

$$E_x = E_0 cos(kz - \omega t + \phi) \tag{1.1}$$

$$B_y = \frac{E_x}{c} = \frac{E_0}{c} cos(kz - \omega t + \phi) \tag{1.2}$$

More generally, the total electric and magnetic fields can be represented as shown in Eq. 1.3 and Eq. 1.4, where $\mathbf{k} = (k_x, k_y, k_z)$. [9]

$$E(r, t) = E_0 cos(\mathbf{k} \cdot r - \omega t + \phi) \tag{1.3}$$

$$B(r,t) = B_0 cos(\mathbf{k} \cdot r - \omega t + \phi) \tag{1.4}$$

The science of spectroscopy measures the interaction between light and matter by quantifying the change in light during or after this interaction. Generally this means studying changes in intensity ($I \propto E_0^2$), wavelength (color) and polarization. While wavelength and intensity can be easily understood, the concept of polarization can be more challenging and requires further explanation.

By convention, polarization is defined according to the propagation of the electric field. The six degenerate polarization states are shown below in Figure 1.2. Vertical and horizontal polarization are defined when the electric field, propagating in the z direction, is oscillating in the y and x directions, respectively. The subsequent polarization states can be thought of as combinations of the E_x and E_y waves with a phase difference (δ) between them. The polarization of light is often used to increase contrast in images. The most common example being polarized lenses in sunglasses, which increase contrast and decrease glare. Polarized spectroscopy measures the differences in interaction with the different polarization states of light, or the change in polarization that occurs when light passes through materials.
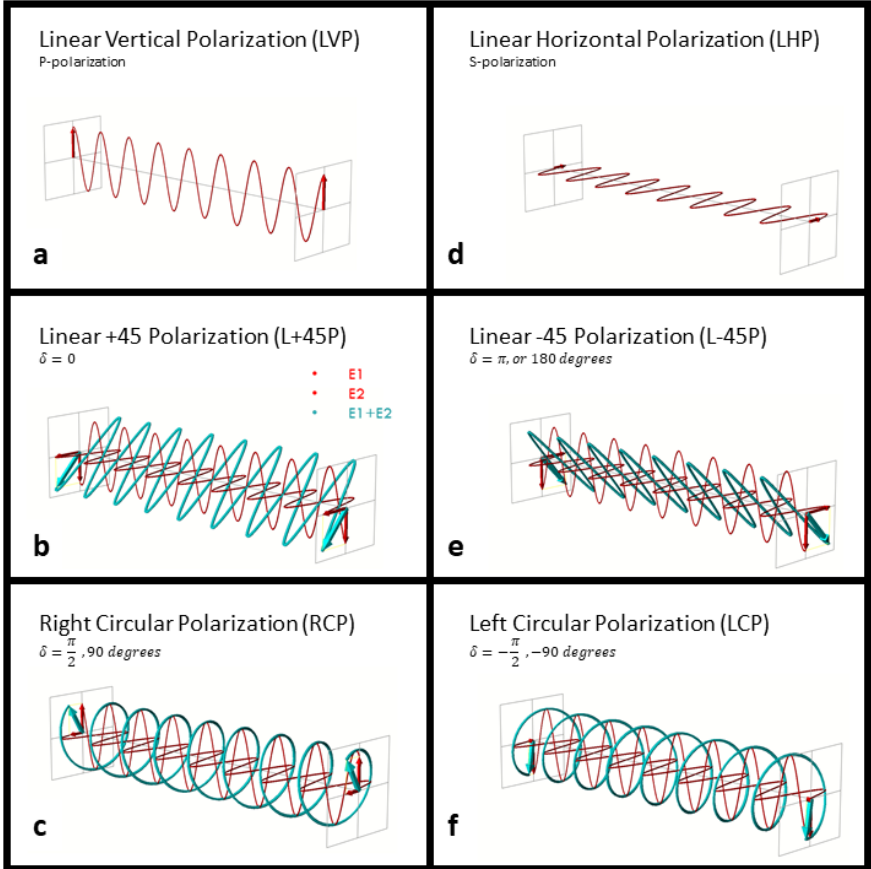
FIGURE 1.2: Figure depicting the six degenerate polarization states, adapted from [8] and [10]. (a) and (d) show the linear vertical and horizontal polarization states (red). (b) and (e) show the linear +45 and -45 degree polarization states (blue), shown as a combination of the vertical and horizontal polarization states (red) with a 0 or 180 degree phase difference. (c) and (f) show the right- and left-circularly polarized states (blue), which can also be composed from two linear polarization states + or - 90 degrees out of phase (red).

With a description of the quantities used to study light–matter interaction developed, the interaction phenomena itself can now be defined. At a small scale, matter is a grouping of protons, neutrons and electrons, and can be thought of in terms of energy levels. Some of the ways light can interact with a material are illustrated in Figure 1.3. The incoming light is repre-

sented as the red wave, and the various energetic states are represented by the horizontal black and grey lines.
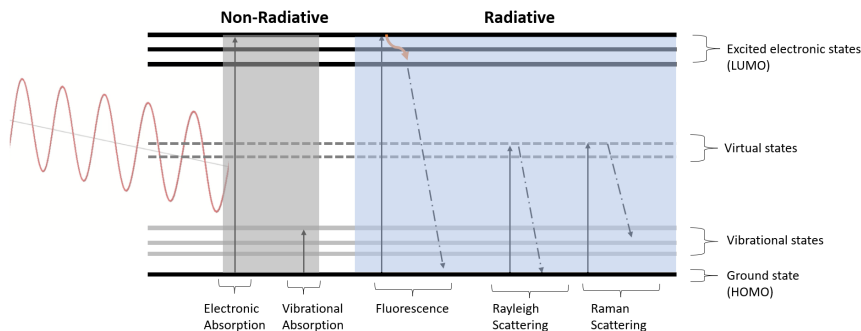
FIGURE 1.3: A pictorial description of the various radiative (light emitting) and non-radiative (non-light emitting) ways that light can interact with a material, represented here by an energy band diagram.

One of the simplest forms of spectroscopy is absorption spectroscopy. The change in intensity of white light as it passes through a material is measured. A slightly more complicated version is wavelength-resolved absorption spectroscopy, which looks at the change in intensity absorbed over a range of wavelengths. By changing the wavelength of light that is used, absorption into the vibrational or electronic states can be studied. Even this extremely simple spectroscopy can be used to understand complex phenomena such as the electronic structure of semiconducting nanocrystals. [11]

Absorption is a non-radiative process, meaning that you expect to measure less light after it passes through the material. Another class of light–matter interaction is radiative processes, including (but not limited to) fluorescence and scattering. Fluorescent materials absorb incident light and then emit light of a different wavelength. Scattering, shown in 1.3 as Rayleigh and Raman scattering, is a phenomena where incident light interacts with the material and light of the same, or slightly different, wavelength is emitted. The difference between fluorescence and scattering will be discussed in detail below. Importantly, in radiative processes, the effect of both the incident and emitted photon can be studied, meaning that there

are typically more variations of spectroscopy techniques involving radiative processes.

Though different types of spectroscopy measure different parameters (intensity, wavelength, polarization,etc.) and probe different materials parameters (electronic structure, vibrational states, etc.), the core function of the study of light–matter interaction remains the same. This thesis focuses on a type of spectroscopy based on the phenomena of light scattering, which is treated in detail below.

1.2   LIGHT SCATTERING

Light scattering, as shown in Figure 1.3, results when a photon interacts with a material, and then a second photon is emitted. While from an observers perspective, this is similar to the phenomenon of fluorescence, the physical mechanism is very different. In fluorescence, the incident photon must be sufficiently energetic to excite an electron from the ground state to an excited electronic state. In this first step, energy is conserved. In the second step of fluorescence, the electron relaxes to the lowest excited state and then is re-emitted as a photon, with the wavelength corresponding to the energy gap between the excited state and ground state.

Though light scattering may seem similar, i.e. it is a photon in, photon out process, it does not relate strictly to the electronic structure of the material. It is the result of a non-energy conserving perturbation of the material. [7] This is why the term "virtual state" is used to represent the effect of the incident photon, because though scattering can occur from incident light that corresponds to a specific energy gap in the material (resonance scattering), it is not a requirement for scattering to occur.

Light scattering can be split into two categories, inelastic and elastic. During elastic light scattering, such as Rayleigh and Mie scattering, the frequency of the scattered light (ω_s) is the same as the incident light ($\omega_i = \omega_s$), and no energy is transferred. Inelastic scattering, such as Raman scattering is an active process which involves the transfer of energy and the light is scattered at a different frequency than the incident light ($\omega_i \neq \omega_s$). [7]

The change in frequency which occurs in inelastic scattering should not be confused with the difference in the intensity of the light scattered. For example, both Rayleigh and Mie scattering are elastic processes, which occur at different length scales and depend on the frequency of the incident light. When the size of a particle is on the order of the wavelength of light, then Mie scattering occurs, and when the size of the particle is much smaller that the wavelength of light, Rayleigh scattering occurs. The intensity of Mie scattering does not depend on wavelength, whereas the intensity of Rayleigh scattering scales with $I_{Rayleigh} \propto \frac{1}{\lambda^4}$. [6] This is commonly used to explain why clouds, which are composed of water vapor droplets (c.a. 10μm), are white, and the sky, composed of diatomic nitrogen and oxygen molecules (c.a. 0.2 nm), appears blue. The scattering of light from clouds is dominated by Mie scattering and is not wavelength dependent, whereas atmospheric scattering is dominated by Rayleigh scattering and preferentially scatters the shorter-wavelength blue light. For the purposes of this thesis we will narrow the focus to scattering from molecules or length scales much smaller than the wavelength of light.

1.2.1 *Rayleigh and Raman Scattering*

This thesis will focus on light scattering from molecules, which is dominated by Rayleigh and Raman scattering. As mentioned above, scattering is a perturbation-based process. If we first consider Rayleigh scattering, the molecule can be thought of a set of fixed nuclei surrounded by a "cloud" of electrons. Upon interaction (perturbation) with an incident electric field, the electron cloud will respond by shifting with respect to the nuclei. When the incident electric field is oscillating (as with light) the electron cloud then oscillates in response. The oscillating electron cloud is now essentially an electric dipole (μ). This oscillating dipole then acts as the source of an oscillating electric field (E_s) with an intensity (I_s), as shown in Eq. 1.5. θ is the angle between the electric field of the incident radiation with respect to the axis of the dipole.

$$I_s = k'_\omega \omega_s^4 \mu_0^2 sin^2\theta \tag{1.5}$$

The magnitude of this induced dipole is a function of the electric-dipole–electric-dipole polarizability (α), as shown in matrix form in Eq. 1.6 and

using the summation convention in Eq. 1.7. [6, 7]

$$
\begin{pmatrix} \mu_{x_0} \\ \mu_{y_0} \\ \mu_{z_0} \end{pmatrix} = \begin{pmatrix} \alpha_{xx} & \alpha_{xy} & \alpha_{xz} \\ \alpha_{yx} & \alpha_{yy} & \alpha_{yz} \\ \alpha_{zx} & \alpha_{zy} & \alpha_{zz} \end{pmatrix} \begin{pmatrix} E_{x_0} \\ E_{y_0} \\ E_{z_0} \end{pmatrix}
\tag{1.6}
$$

$$
\mu_{\rho_0}(\omega_i) = \alpha_{\rho\sigma}^{Ray} \cdot E_{\sigma_0}(\omega_i)
\tag{1.7}
$$

Raman scattering, on the other hand, does not assume that the nuclei are fixed and in fact studies the energy states in the molecule that are the result of molecular vibrations (where the nuclei are moving with respect to one another). Raman scattering is inelastic, meaning that energy is exchanged, and the frequency of the radiating dipole is shifted as shown in Eq. 1.8. [7]

$$
\mu_{\rho_0}(\omega_i \pm \omega_{vibration}) = \alpha_{\rho\sigma}^{Ram} \cdot E_{\sigma_0}(\omega_i)
\tag{1.8}
$$

The difference between $\alpha_{\rho\sigma}^{Ray}$ and $\alpha_{\rho\sigma}^{Ram}$ is that the Raman tensor is actually the change in polarizability with respect to a molecular vibration (Q) as shown in Eq. 1.9.

$$
\alpha_{\rho\sigma}^{Ram} = \frac{\partial \alpha_{\rho\sigma}}{\partial Q}
\tag{1.9}
$$

For a mode to be "Raman active", the change in polarizability over the vibrational motion must be non-zero, i.e. $\frac{\partial \alpha_{\rho\sigma}}{\partial Q} \neq 0$. The number of possible vibrational modes for a molecule with N atoms, is 3N-5 for a linear molecule and 3N-6 for a non-linear molecule. [12] This means, for instance, that for H_2O, a non-linear molecule, a total of 3 vibrational modes exist, and because all of them cause a change in the polarizability, all are Raman active.

In subsequent sections, for simplicity, we will refer only to $\alpha_{\rho\sigma}$, but the reader should note that in the case of Raman scattering this always refers to the transition polarizability as shown in Eq. 1.9. It is the transition polarizability because it represents the change in the polarizability from the initial vibrational energy state (v_i) to the final vibrational energy state (v_f), represented in Eq. 1.9 as ∂Q. As will be explained in a later section, Eq. 1.7 and Eq. 1.8 are actually simplifications which are only valid for a certain class of molecules, and for other groups more polarizability terms come into play.

1.3 SYMMETRY AND NEUMANN'S PRINCIPLE

For certain less-symmetric molecules, additional polarizability terms can contribute to μ_{ρ_0}. The basis for understanding when these terms do and do not contribute to scattering, is molecular symmetry. Molecules can be described purely in terms of their symmetry and this can be very useful for understanding the properties of large groups of molecules. There are five basic symmetry operations, identity (E), rotation (C_n), reflection (σ), inversion (i) and rotation–reflection (S_n), which is a rotation followed by a reflection perpendicular to the axis of rotation. [12]

A molecule "possesses" a symmetry operation when that operation leaves the molecule unchanged. For instance, if a water molecule is rotated 180 degrees with the axis of rotation through the oxygen atom, the resulting molecule will look the same, so the water molecule "possesses" an axis of rotation. A comprehensive review of molecular symmetry is outside of the scope of this introduction, but the interested reader is directed to Chapter 4 of *Inorganic Chemistry* by Gary L. Miessler and Donald A. Tarr, which gives an excellent introduction to symmetry and group theory. [12]

Molecular symmetry is important in our discussion because the symmetry possessed by the molecule must also be possessed by the molecular properties— a concept known as Neumann's principle. [6] For instance, if we consider that the water molecule possesses a rotation axis, then that same rotation must leave the polarizability tensor (α) unchanged. This determines then, which terms in α are zero and which have a finite value.

When describing the induced dipole (μ) previously, we only included one polarizability term α, when in fact the electric field also induces an oscillating electric quadrupole, and the magnetic field induces a magnetic dipole term. The electric quadrupole polarizability term (A) and the magnetic dipole polarizability term (G) both can also contribute to the induced electric dipole moment (μ), although this contribution to the scattered intensity is typically several orders of magnitude lower than the contribution of the α term. A more complete equation of the induced electric dipole, including these additional terms, is shown in Eq. 1.10.

$$\mu_{\rho_0} = (\alpha_{\rho\sigma} + \frac{i\omega}{3c}n_\gamma^i A_{\rho,\gamma\sigma} + \frac{1}{c}\epsilon_{\gamma\delta\sigma}n_\delta^i G_{\rho\gamma})E_{\sigma_0} \qquad (1.10)$$

These new polarizability tensors G and A transform differently under symmetry operations. The equations for the induced electric quadrupole (Θ) and the induced magnetic dipole (m) are shown below.

$$\Theta_{\rho_0 \sigma_0} = (A_{\gamma, \rho\sigma}) E_\gamma \qquad (1.11)$$

$$m_{\rho_0} = G_{\rho\sigma} E_{\sigma_0} \qquad (1.12)$$

Importantly, because the quadrupole polarizability A relates a second rank tensor (the quadrupole moment Θ) and the electric field, which is a first rank tensor, A itself is a third rank tensor. The magnetic dipole polarizability m is still a second rank tensor, but because the E and B fields are necessarily perpendicular, m is a polar tensor. While the details here are rooted in tensor algebra, for this case it is enough to say that for molecules without a rotation–reflection (S_n), both the A and G terms contribute to the molecular scattering terms.

This group of molecules is called "chiral". Chiral molecules exist in two distinct forms, which are mirror images of one another, but cannot be super-imposed on top of one another. The common example of chirality is left and right hands, which are mirror images and yet not exactly the same. This distinct lack of symmetry gives rise to the additional polarizability terms in Rayleigh and Raman scattering, which can be observed by looking at the difference in scattering of circularly polarized light. This leads to a separate but related aspect of Raman spectroscopy called Raman optical activity (ROA), detailed below.

1.4   RAMAN OPTICAL ACTIVITY

ROA combines the measurement of Raman scattering with the measurement of optical activity, to characterize chiral systems. Optical activity refers specifically to an optical response which differs for left- and right- circularly polarized light (LH-CPL and RH-CPL). In the same way that α defines Rayleigh scattering and $\frac{\partial \alpha_{\rho\sigma}}{\partial Q}$ defines Raman scattering. Rayleigh optical activity is governed by the so-called "optical activity" tensors A and G and ROA is governed by the changes in those tensors over a vibrational mode. When the difference in Raman scattering of circularly polarized light is

measured $(I_R - I_L)$ a ROA spectrum is obtained. Unlike the Raman spectra, which is the sum of LH-CPL and RH-CPL $(I_R + I_L)$, the ROA spectrum will reflect the chirality of the molecule. For two molecules of opposite chirality (enantiomers), the ROA spectra will be mirror images of one another, but the Raman spectra will be identical. Because the A and G terms are, on average, much weaker than the α term, ROA intensity is typically 3-5 orders of magnitude weaker than the Raman intensity. This is quantified by the dissymetry factor (Δ) shown in Equation 1.13. [6]

$$\Delta = \frac{(I_R - I_L)}{(I_R + I_L)} = \frac{ROA}{Raman} \approx 10^{-3} - 10^{-5} \tag{1.13}$$

The ROA spectra of the two enantiomers (left- and right handed version of the same molecule) of β-pinene are shown in Figure 1.4. Because the ROA spectra are defined by contributions from the G and A polarizability terms while Raman $(I_R + I_L)$ spectrum is determined only by the $\alpha_{\rho\sigma}^{Raman}$ term, the Raman signal is the same for both enantiomers, but the ROA spectrum for each enantiomer is a mirror image. ROA therefore enables the probing of chirality at the molecular level, which is key for understanding the influence of chirality in the natural world. [13]
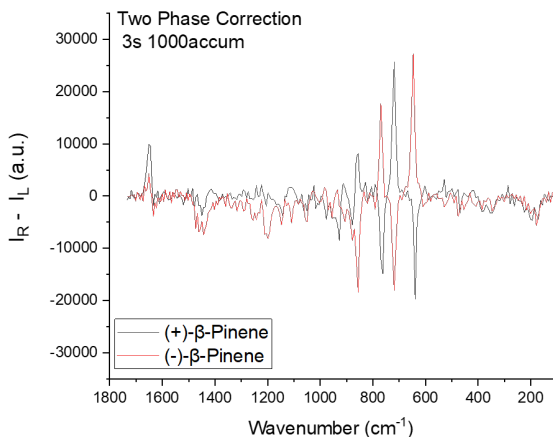
FIGURE 1.4: ROA spectrum of (+) (black) and (-) (red) β-pinene.

Because ROA is able to simultaneously discern the vibrational spectra and the chirality of a molecule, it is an incredibly valuable probe of biochemistry. [14] But because of the relative weakness of ROA scattering, developing instruments which are able to discern small differences in polarization in low–light conditions has proven to be an engineering and scientific challenge.

ROA Instrumentation

ROA was first predicted by Barron and Atkins in 1969, and then demonstrated experimentally in 1973. [15] Because the intensity is so much weaker than Raman scattering, measuring the effect at all was very difficult. The development of ROA instrumentation benefited greatly from advances in laser engineering and sensor development. In 1991, Werner Hug developed the precursor to the only currently commercially available ROA spectrometer. [16] Hug also developed a system to reduce the contributions of polarization artifacts (which will be discussed further in Chapter 3). [17] Despite Werner Hug's advances in instrumentation, the use of ROA has remained limited to only a few research groups and the advancement of the instrumentation has essentially been frozen since Hug retired 20 years ago. The requirement of simultaneous high polarization precision, spectral resolution, low polarization artifacts and efficient light collection remain difficult even now.

This thesis focuses on the development of ROA measurement and instrumentation, first through the design and construction of a new ROA instrument, then through advancing the understanding of polarization artifacts in Chapter 2 and 3, respectively. Chapter 4 then discusses the possible use of surface enhancement effects to solve the problem of weak ROA signal. Finally, Chapter 5 explores the application of the newly developed ROA instrument to the measurement of biological molecules.

1.5 THESIS OUTLINE

CHAPTER 2 Instrumentation

In the first chapter, the development of a new ROA instrument is discussed. This instrument, called ZROA, is the first report of the use of high-frequency polarization modulation to measure ROA. This chapter focuses on the development of the instrumentation and measurement of the relevant controls on the new system.

CHAPTER 3 Artifacts

Instrumental artifacts have been a persistent problem in chiroptical spectroscopy generally and ROA specifically. This chapter focuses on the use of Mueller-matrix modeling to understand the origins of artifacts in ROA, and outlines the necessary controls needed to ensure that true spectra and not artifacts are being measured.

CHAPTER 4 Enhancement

Despite advances in instrumentation and artifact reduction or suppression, applications of ROA are still limited by the low ROA scattering cross-section. The use of surface enhancement has been successful as a method to increase Raman scattering (SERS), but the extension of this to ROA has remained challenging. In this chapter, the complexities associated with extending surface enhancement to ROA are discussed in detail and first proof-of-concept measurements of surface-enhanced ROA in forward scattering are shown.

CHAPTER 5 Forward-Scattered ROA of Biological Molecules

One of the most widely investigated applications of ROA is the measurement of biological molecules. Despite this, few reports exist of forward-scattered ROA of small biological molecules and no reports of forward-scattered ROA spectra of proteins. In this section, the use forward-scattered ROA for the investigation of large and small biological molecules is studied. First ROA spectra of proteins in foward scattering are shown, and the role secondary protein structure in the circular depolarization is discussed.

Conclusions and Outlook

Finally, some general conclusions about the measurement of ROA are discussed and an outlook into future work possible for each section is given.

INSTRUMENTATION

It's kind of fun to do the impossible.

— Walt Disney

The following text has been adapted from "Measurement of Raman Optical Activity with High-Frequency Polarization Modulation", published in J. Phys. Chem. by Lightner et al. [18]

2.1 ABSTRACT

Raman Optical Activity Spectra of β-Pinene
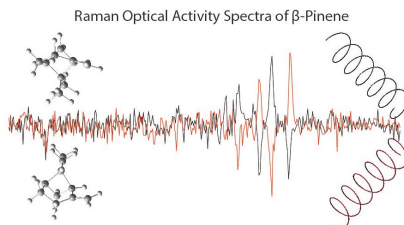
Many chiroptical spectroscopic techniques have been developed to detect chirality in molecular species and probe its role in biological processes. Raman optical activity (ROA) should be one of the most powerful methods, as ROA yields vibrational and chirality information simultaneously and can measure analytes in aqueous and biologically relevant solvents. However, despite its promise, the use of ROA has been limited, largely due to challenges in instrumentation. Here, we report a new approach to ROA that exploits high-frequency polarization modulation. High-frequency polarization modulation, usually implemented with a photoelastic modulator (PEM), has long been the standard technique in other chiroptical spectroscopies. Unfortunately, the need for simultaneous spectral and polarization resolution has precluded the use of PEMs in ROA instruments. We combine a specialized camera system (the Zurich Imaging Polarimeter, or ZIMPOL) with PEM modulation to perform ROA measurements. We demonstrate performance similar to the current standard in ROA instrumentation while reducing complexity and

polarization artifacts. This development should aid researchers in exploiting the full potential of ROA for chemical and biological analysis.

2.2   INTRODUCTION

The measurement of ROA presents unique instrumentation challenges. The dysymmetry factors are, at most, on the scale of 10^{-3}. This results in the requirement that, in order to measure ROA, the LH- and RH-CPL must be separated with a precision exceeding this. In addition, because the fundamental effect (Raman scattering) itself is relatively weak, the measurement must be done in a relatively "photon-starved" environment. These challenges have meant that the progression of ROA instrumentation has been slower than sister techniques such as vibrational circular dichroism (VCD) and circular dichroism (CD).

In most chiroptical spectroscopy techniques, a linear polarizer and a variable phase modulator, typically a photoelastic modulator (PEM), are used to create CPL in the excitation path or to measure the circular component in the emitted light in the collection path. [19, 20] PEMs rely on photoelasticity, i.e. the change in optical properties of a material under mechanical deformation to create a variable retarder for the optical phase. A strain is induced in the PEM material, leading to a desired retardation. [21] While other devices such as Pockels cells or liquid crystal retarders (LCR) can also be used as variable phase retarders, PEMs have several significant advantages. They produce reliable phase retardations, have large optical apertures, are stable over long periods of time, and can modulate at high frequencies (20–84 kHz). [22] This is in contrast to LCRs, which exhibit hysteresis, and Pockels cells, which have small (< 10 mm) optical apertures. [16, 22]

Another advantage of PEMs is that they can be combined with a lock-in amplifier to extract polarization information with high signal to noise. [22, 23] However, this approach must then use fast point detectors to collect the scattered light. Such detectors can be synchronized with the high-frequency modulation of the PEM. This presents a challenge for ROA, because a spectrum of the scattered light should be obtained. Ideally, one would like to use a spectrometer to disperse the signal onto a charge-coupled-device (CCD)-sensor-based camera and obtain the spectral information in parallel. Unfortunately, read out of a CCD chip is too slow to be coupled to the high-speed modulation of the PEM. Consequently, one instead scans a

monochromator, collecting one wavelength at a time with the fast point detector. This approach, which, by necessity, was used in early ROA instruments, leads to instrumental artifacts and prohibitively long measurement times that impede the general use of ROA. [15, 24]

Here, we present a different route that exploits fast polarization modulation with a PEM to collect ROA spectra. We employ a unique optical detector, a Zurich Imaging Polarimeter (ZIMPOL) system, and combine it with a PEM. The ZIMPOL system is built around a CCD imaging detector, but it allows the modulation speed of the PEM to be decoupled from the slow CCD readout speed. This is achieved by using a partially masked CCD detector and shifting the charges from the unmasked area of the CCD to the masked areas. [22, 25] The shifting of the charges can be synchronized with the PEM such that the different polarization states are sorted onto different rows of the CCD. Meanwhile, a grating in the detection path disperses the wavelength information onto different columns of the CCD. The CCD output can then be processed to obtain ROA spectra. The use of a PEM means that polarization artifacts inherent in other forms of polarization modulation, such as LCRs, can be avoided. Consequently, the stability and reliability of PEMs, which have long been preferred for polarization modulation in other commercial chiroptical measurement systems, can be exploited in ROA measurements. After describing our new apparatus, we compare it to other more traditional ROA instruments. We find that our first-generation device offers similar performance while greatly reducing instrument complexity. Thus, we demonstrate a new approach to ROA instrumentation that can potentially bring ROA spectrometers to the level of other chiroptical techniques.

2.3 METHODS

ROA can be measured either by modulating the polarization of the incident laser light (ICP) or by measuring the circular component in the scattered light (SCP). [26] The ROA spectra from ICP and SCP measurements should be identical. [6] Indeed, this has been confirmed by several experimental reports. [16, 27] The choice between SCP and ICP is then one of experimental convenience. For the construction of our instrument (see Figure 2.1), the SCP configuration was selected to facilitate comparison with other reported ROA data, which were collected using SCP. Our apparatus should work

equally well with ICP, in which case, the PEM would be used to modulate the incident laser beam.
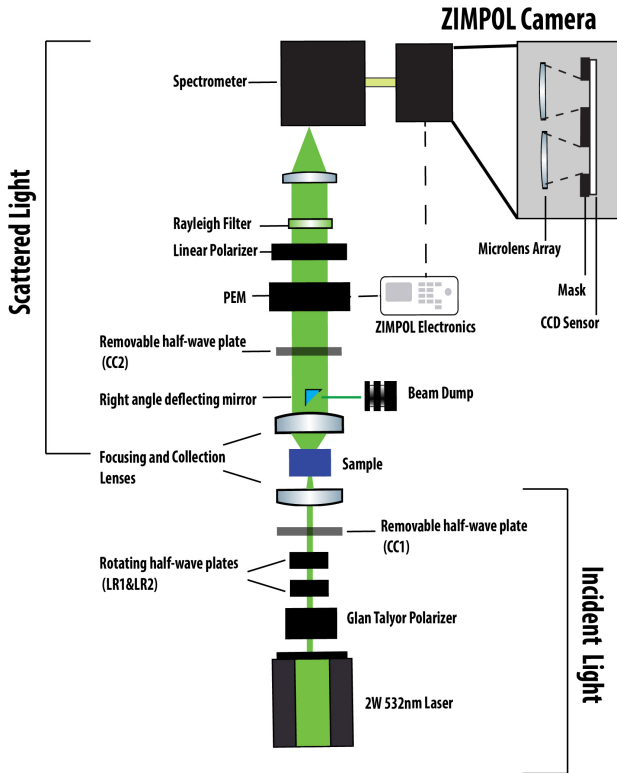
FIGURE 2.1: Schematic of the Z-ROA instrument. LR1 and LR2 are zero-order half-wave plates in custom-made rotating mounts. CC1 and CC2 are zero-order half-wave plates mounted in sliding mounts. The inset (top right) shows a schematic of the ZIMPOL camera system showing the microlens array that focuses the light onto the open (unmasked) pixel rows. The charges below the mask are shifted in synchrony with the photoelastic modulator (PEM) to sort light of different polarization states onto different rows of the CCD pixel array.

The second choice in the construction of our ROA instrument was the angle from which to collect the scattered light. In the literature, back-scattering, 90-degree-scattering, forward-scattering, and so-called "magic-angle-scattering" have all been used. [20] Each of these configurations leads to different contributions from the optical-activity tensors and therefore different ROA spectra. [28] This choice is therefore more consequential than the choice of SCP versus ICP. Back-scattering is generally preferred because it exhibits higher dissymmetry due to lower contributions from standard Raman scattering. The experimental realization of SCP-ROA with the back-scattering configuration is, however, challenging. Traditional optical techniques such as using a beam-splitting cube to excite and collect in the same path are not possible because they introduce polarization artifacts. To avoid this while still using back-scattering, the laser can be launched into the sample path via two small right-angle prism mirrors. [16, 29] Unfortunately, this approach, which has been employed in several successful ROA instrument variations, introduces a large amount of birefringence and alignment sensitivity.

Therefore, we chose forward-scattering instead. This configuration has been previously demonstrated experimentally and, while fewer features appear in the resulting ROA spectra, forward-scattering is still able to easily distinguish enantiomers. [30, 31] Constructing the instrument in forward-scattering also allows all of the polarization conditioning optics to be in the same plane, as shown in Figure 2.1. This reduces polarization artifacts and alignment issues. A small 3 mm right-angle silver mirror is still used, but now it deflects the laser beam out of the signal path after interacting with the sample. Therefore, this optical element does not affect the polarization of forward-scattered light that is collected.

The current standard in ROA instrumentation was introduced by Hug et al. in 1999. [16] It utilizes a liquid-crystal retarder followed by polarizing beam splitters to separate the polarization states into two separate optical paths which are then imaged into the detector simultaneously. This design revolutionized ROA instrumentation because imaging the polarization states simultaneously eliminated many sources of error. However, it relies on specialized fiber optics to couple to the spectrometer, as well as a specially shaped detector and is generally very alignment sensitive, additionally, it uses a liquid crystal retarder which are known to exhibit some hysteresis, all of which can present a significant challenge in widespread

use.

The main advantage of our instrument is its use of a PEM to separate the polarization states in the collected signal. Invented in 1966, PEMs exploit the inverse piezoelectric effect in optical materials to produce strain-induced birefringence using an electrical signal. This allows PEMs to act as high-frequency variable phase retarders. The retardation follows a sinusoidal pattern where the maximum retardation can be set by the PEM electronics. Our PEM (Hinds Instruments, II/FS42) operates at 42 kHz and is set so that at its maximum retardation it is approximately a quarter-wave plate. At this point, the CPL incident on the PEM is converted to linearly polarized light at $\pm 45°$ to the PEM optical axis. (+ is defined as a clockwise rotation looking in the direction of light propagation.) This light then passes through a linear polarizer set at at $+45°$ to the PEM optical axis. The polarization state in the beam incident on the PEM is therefore converted after the linear polarizer to a beam with sinusoidally varying intensity at the PEM operating frequency.

Unfortunately, it has not been possible to use high-frequency modulators such as PEMs in ROA measurements because of the difficulty of coupling a modulator at > 1 kHz to a CCD detector. Typically, imaging arrays used in scientific cameras or spectrometers are based on either CCD or CMOS sensors, which have relatively slow read out times in the range of 20 ms. [9] The detector read-out speed is too slow to allow high-frequency polarization modulation. This has limited PEMs to setups with high-speed point detectors. [16] Our instrument avoids this problem with the use of the ZIMPOL detection system. [22], [1, 32] The original ZIMPOL system was developed in the early 1990s by Povel et al. at ETH Zürich for use in solar physics. [25] By examining polarimetric images of the sun and occasionally other astronomical objects, ZIMPOL has enabled researchers to make important observations about the magnetic fields and atmospheres of these bodies, leading to several important discoveries in the field of astronomy. [9, 22] ZIMPOL was developed in part to address the problem of seeing noise i.e. polarization states caused by atmospheric disturbances in the observation path, which had previously precluded the measurement of high resolution polarimetric images. By measuring at modulation frequencies above 1 kHz, ZIMPOL is able to compare polarization states with the same seeing noise, allowing ZIMPOL systems to reach polarization resolutions of 10^{-5}. [22] Three generations of ZIMPOL instruments have been developed,

ZIMPOL III , developed in 2007, is a compact (c.a. 150x100x60 mm) system, portable enough to be moved to different telescopes worldwide. Because applications have (until this work) been limited to astronomy, only 3-4 working ZIMPOL systems currently exist. Continued development of the ZIMPOL system is now done by teams at the Solar Institute of Locarno (IRSOL) and the Institute for Systems and Applied Electronics (ISEA) at the University of Applied Science of South Switzerland (SUPSI). ZIMPOL utilizes a partially masked CCD and then synchronizes the movement of the charges between rows of the CCD with the PEM, effectively decoupling the speed of the polarization modulation from the read-out speed of the camera. [25]

The ZIMPOL system used in our ROA instrument masks three of every four pixel rows on the CCD (which has 560 pixel rows total) and then moves the charges between rows such that during one PEM modulation cycle the signal is distributed over the four pixel rows in time. This allows the LH- and RH-CPL spectra to be separated onto rows 1 and 3 and the 45° linear polarization spectra onto rows 2 and 4 (see Figure A.1 in the Appendix A.1). Additionally, a microlens array is mounted in front of the mask so that the optical signal is efficiently channeled through the holes in the mask (see inset in Figure 2.1).

Our overall instrument design (Figure 2.1) was heavily influenced by Hug et al. [16, 30] For excitation, a 2 W 532 nm continuous-wave (cw) laser (Coherent, Verdi 2W) is sent through a Glan-Taylor laser prism with an extinction ratio of 1:100,000 to improve the polarization purity of the input beam. This is followed by "linear rotators," which consist of two counter-rotating zero-order half-wave plates. [17] These are rotated at approximately 300 rpm in custom-made rotating mounts. [17] Such rotation is necessary because a significant source of artifacts in ROA measurement is birefringence in the excitation path. By rotating the plane of linear polarization over all angles, depolarized light is created on the time scale of a single spectral acquisition, effectively canceling out any birefringence in the excitation path. Additionally, two half-wave plates can be moved in and out of the optical path before and after the sample. These act as circular converters (CC1 and CC2, Figure 2.1) and are part of the virtual enantiomer correction scheme, [17] which is discussed in detail in the next section.

Light is focused onto the sample using a 25.4 mm diameter lens with a 100 mm focal distance. The sample is held in either a glass vial or a custom-made sample holder. After the sample, the scattered signal is collected using a 25.4 mm diameter lens with a 30 mm focal distance, while the transmitted laser beam is deflected from the center of the path into a beam dump using a 3 mm right-angle mirror positioned in the center of the lens using a custom mount. When in use, the second circular converter (CC2) is positioned behind the beam deflector, after which the light is incident on the PEM. As mentioned above, after the PEM a linear polarizer is set at 45° to the PEM optical axis, followed by a Rayleigh filter (Iridian, Dielectric Super Notch Plus Filter). The signal is then focused onto a 50 μm slit and launched into an Andor Holospec high-throughput spectrometer, after which it is measured by the ZIMPOL camera system. The spectrometer uses a transmission grating to spatially disperse the light so that the lateral distance in the collected image corresponds to the wavelength of the scattered light, and the vertical lines on the final image are the corresponding spectral peaks. Detailed information about all of our optical components, including manufacturer and part number, are included in Appendix A.1. Also included in Appendix A.1 are a list of the chemicals used.

2.4   RESULTS AND DISCUSSION

Calibration and Control Measurements. To evaluate the performance of our ROA spectrometer we measured experimental variables that have already been reported for comparable instruments. For this, we identified the depolarization ratio (*DR*) and the degree of circularity (*DOC*) of carbon tetrachloride (CCl_4) as useful parameters for which data exists in the literature. [16, 30] CCl_4 is an achiral molecule, and has no ROA signal. However, the vibrational modes in CCl_4 are highly polarized, meaning that because of anisotropic invariants in the standard Raman tensor, they exhibit strong differences in their response to perpendicular linear polarization states. [7] The level of polarization of a mode is quantified by the depolarization ratio (*DR*), defined as Eq. 2.1.

$$DR(0°, +45°^{,i}) = \Delta = \frac{I^s_{+45}}{I^s_{-45}} = \frac{I^s_{\perp}}{I^s_{\parallel}} \tag{2.1}$$

The first term in the parentheses indicates the direction of the collected Raman-scattered light ($0°$ is forward-scattering), and the second term, $+45°,i$, indicates the polarization of the light incident on the sample, here at $+45°,i$ with respect to the PEM optical axis. DR is calculated by dividing the intensities of perpendicular linear polarization states measured in the scattered light indicated by I^s_{+45} (or $I^s_\perp$) and I^s_{-45} (or $I^s_\parallel$). A mode is considered polarized when Eq. 2.2 holds. [7]

$$0 < DR(0°, +45°,i) < \frac{3}{4} \tag{2.2}$$

The determination of DR is useful for quantifying the precision of linear polarization that an optical setup can measure as well as its sensitivity to the amount of linear polarization in the incident path. The degree of circularity (DOC) measures the same tensor invariants but with incident circularly polarized light according to Eq. 2.3.

$$DOC(0°, I^i_R) = \frac{I^s_R - I^s_L}{I^s_R + I^s_L} \tag{2.3}$$

Here, I^s_R and I^s_L are the intensities of Raman-scattered RH- and LH-CPL, respectively. Figure 2.2 shows DOC (top), DR (center) and Raman spectra for CCl_4.

A second useful control is to compare the DR value measured with incident linearly polarized light to the calculated DR from the DOC. We can exploit the fact that DOC and DR are related by Eq. 2.4. [7]

$$DR(0°, +45°,i) = \frac{1 - DOC(0°, I^i_R)}{3 + DOC(0°, I^i_R)} \tag{2.4}$$

where $DOC(0°, I^i_R)$ is the degree of circularity in forward-scattering, measured with incident right-circularly polarized light.
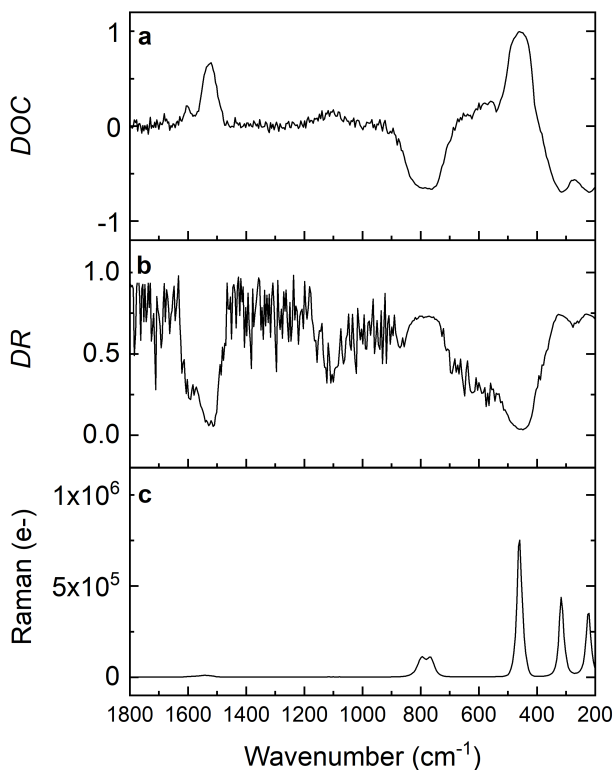
FIGURE 2.2: (a) The degree of circularity (*DOC*), (b) depolarization ratio (*DR*), and (c) Raman spectra ($I_R + I_L$) of CCl_4 measured with our Z-ROA experimental setup. These reference measurements on achiral CCl_4 give an indication of how the instrument discriminates circular (*DOC*) versus linear (*DR*) polarization in the scattered light.

By taking measurements of the *DR* and *DOC* on CCl_4 and comparing the values to those reported in the literature, the performance of the new ROA instrument can be evaluated. Because *DOC* and *DR* are normalized quantities, they can be easily compared across instruments, rather than the intensities and shapes of ROA spectra which depend strongly on the exact experimental set-up. The use of both measurements (*DOC* and *DR*) reveals how a given instrument interacts with linear versus circularly polarized light, and since the separation of perpendicular linear polarization states

is often much easier than the separation of opposite circularly polarized states, this also acts as a useful instrumental reference.

	Raman Mode (cm⁻¹)	Degree of Circularity	Calculated Depolarization Ratio	Measured Depolarization Ratio
Theoretical values	316	−0.710	0.750	–
	460	0.960	0.010	–
Instrument of Hug *et al.*	316	0.689	0.730	0.740
	460	−0.979	0.005	0.005
Z-ROA	316	−0.693	0.734	0.734
	460	0.994	0.002	0.038

TABLE 2.1: Comparison of the values of the degree of circularity (*DOC*), the measured depolarization ratio (*DR*), and the depolarization ratio calculated from the *DOC* for two Raman modes of CCl_4. The theoretical values are shown in the top two rows [7], then values measured from the back-scattering instrument of Hug et al., [16] and finally values measured from our instrument (Z-ROA). The sign differences between the measurements of Hug et al. and those of Z-ROA are due to backward- versus forward-scattering, respectively.

Table 2.1 compares measurements from our instrument (Z-ROA) to those from the instrument of Hug et al. as well as calculated values for two CCl_4 vibrational modes. [7, 16] We find good agreement for the *DOC* values for both modes and relatively good agreement for *DR* measured and calculated at 316 cm^{-1}. The measured value for DR at the 460 cm^{-1} mode in this instrument is, however, much larger than expected (0.038 measured versus 0.002 calculated). This reflects the fact that this instrument, though able to measure linearly polarized light, is optimized for circularly polarized light. For modes that are almost completely polarized (like the 460 cm^{-1} mode in CCl_4), very little signal exists for one polarization state, leading to a less precise *DR* ratio measurement. Similarly, in the *DR* spectra in Figure 2.2, noise increases in the regions without peaks because two values with very low signals are being divided. In comparison, because *DOC* is the difference over the sum of the CPL, the values in regions with no features will always be close to zero because the total signal (i.e., the denominator) will always be orders of magnitude larger than the difference signal.
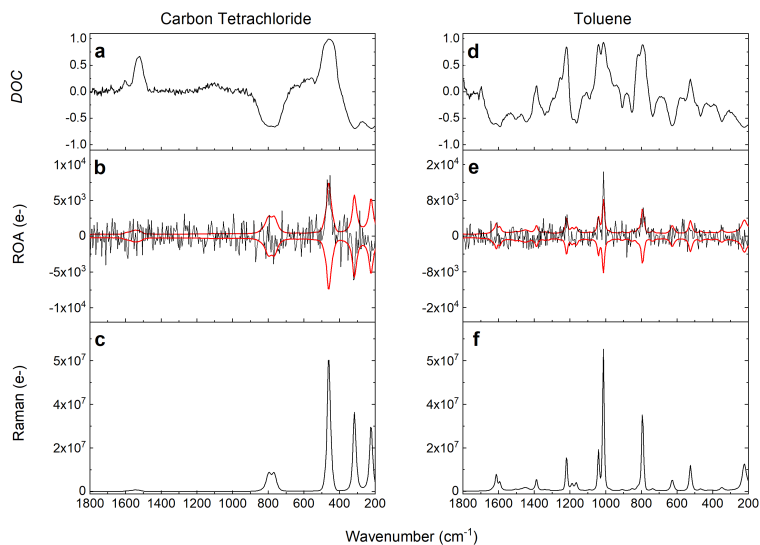
FIGURE 2.3: Control ROA measurements of achiral molecules. The left and right panels show results for CCl_4 and toluene, respectively. (a,d) *DOC* measured with incident circularly polarized light. (b,e) Spectra of the difference in scattered intensity $I_R - I_L$ (i.e. the ROA signal) with incident depolarized light. The expected error due to shot noise, calculated as the square root of the Raman spectra, is shown with the red line. (c,f) Spectra of the sum $I_R + I_L$ (i.e. the Raman signal) measured with unpolarized light. The measurements were taken with 0.5 W of laser power, 1 mL of sample volume, and roughly 2 min of measurement time, with no virtual-enantiomer correction.

The *DOC* is also a useful control measurement because it indicates which bands are strongly polarized (*DOC* close to 1 or −1). Strongly polarized modes tend to result in a circular signal that is the result not of the chirality of the molecule but the anisotropic invariants of the standard Raman scattering tensor. Figure 2.3 shows the forward-scattered ROA spectra for two achiral molecules, toluene and carbon tetrachloride, and compares these signals to the expected shot noise, which is calculated as the square root of the Raman signal. [30] Because the incident light is depolarized and the molecules are achiral, zero signal in the circular difference spectra is expected. For both molecules, the peaks in the ROA spectra are largely

below the noise except those that correspond to strongly polarized modes, as indicated by the *DOC* spectra in the top panel. Artifacts caused by strongly polarized modes are of even greater concern when measuring chiral molecules, and for this reason we show the *DOC* spectra in the top panel of each ROA measurement below. Modes that appear in the ROA spectra and are also strongly polarized, as indicated by the *DOC*, should always be closely examined. Additional control measurements, with varying laser powers and accumulation times, are shown in Figures A.3-A.6 in the Appendix A.1.

ROA Measurements Figure 2.4 shows ROA measurements for two chiral molecules (α-pinene and β-pinene). The β-pinene measurement was made in just 4 minutes while α-pinene required longer (40 min) to achieve the desired signal-to-noise for the ROA signal. Both α-pinene and β-pinene show mirror-image spectra for enantiomers, and the peaks are similar to those reported from other forward-scattering ROA instruments. [30, 31] Because the goal of this study was to test whether it would be possible to measure SCP-ROA using a PEM in the scattered path, rather than compete with the commercially available ROA systems, larger measurement volumes (1 mL) were typically used. With further effort the sample volume could likely be reduced. Unlike other ROA instruments, our apparatus requires little to no re-alignment, and once the optical path is fixed the measurements are consistent. This is likely due to the simplified optical path that was achieved with forward-scattering and the stability and reliability of the PEM. ROA of limonene was also measured and is shown in Figure A.6.
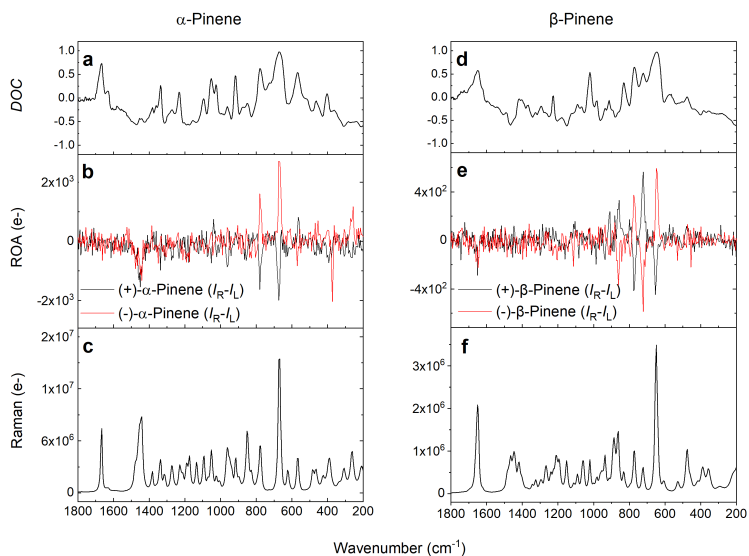
FIGURE 2.4: ROA measurements of chiral molecules with two-phase virtual enantiomer correction. The left and right panels show results for α-pinene and β-pinene, respectively. (a,d) *DOC* measured with incident circularly polarized light. (b) ROA spectra ($I_R - I_L$) for (+)-α-pinene and (-)-α-pinene. (e) ROA spectra for (+)-β-pinene and (-)-β-pinene. (c,f) Raman spectra ($I_R + I_L$) for (+)-α-pinene and (+)-β-pinene, respectively. The measurement conditions for (+)-α-pinene were 0.75 W of laser power, 1 mL of sample volume, and 40 min of measurement time. The measurement conditions for β-pinene were 1.5 W of laser power, 1 mL of sample volume, and 4 min of measurement time.

Virtual Enantiomer Scheme The virtual enantiomer scheme was introduced first by Hug et al. as a way to overcome sources of systematic instrumental offset and is now widely used in most ROA instruments. [17] The scheme involves using a series of half-wave plates to reverse the sense of circular polarization, creating the so-called "virtual" enantiomers. These measurements are then subtracted from one another to correct for offsets. Both measurements in Figure 2.4 were taken with two-phase correction, meaning that for each ROA spectrum a measurement was first taken without CC1 and CC2 in the optical path (see Figure 2.1) and then a second measurement was taken with CC1 and CC2 in the optical path. The two

measurements are then subtracted from each other to remove any offsets caused by instrumentation. In our Z-ROA instrument, the only offsets present appear to be those generated from the strongly polarized modes, such as the one at ca. 640cm $^{-1}$ in β-pinene.

Figure 2.5 shows measurements of β-pinene taken without phase correction (without CC1 and CC2 in the optical path), with 2-phase correction and with 4-phase correction. The 4-phase correction scheme consists of taking four separate measurements, with CC1 in, CC2 in, CC1 and CC2 in, and a final measurement with no half-wave plates in the path. The 4-phase measurement also corrects for the small discrepancies caused by the half-wave plates themselves. [17] The largest difference between the measurement without correction and with 2-phase and 4-phase correction is the flipping of the strongly polarized mode at 640 cm^{-1}. This suggests that the largest source of offsets in this instrument are those caused by the strongly polarized modes of the measured molecules. This appears to differ from other instruments where the virtual enantiomer scheme of Hug et al. corrected for larger offsets caused by birefringence in the optical path. [17] A possible reason for this is the use of forward-scattering which avoids the difficult beam deflection scheme. More investigation is needed to compare this instrument with others and understand the sources of the offsets in each.
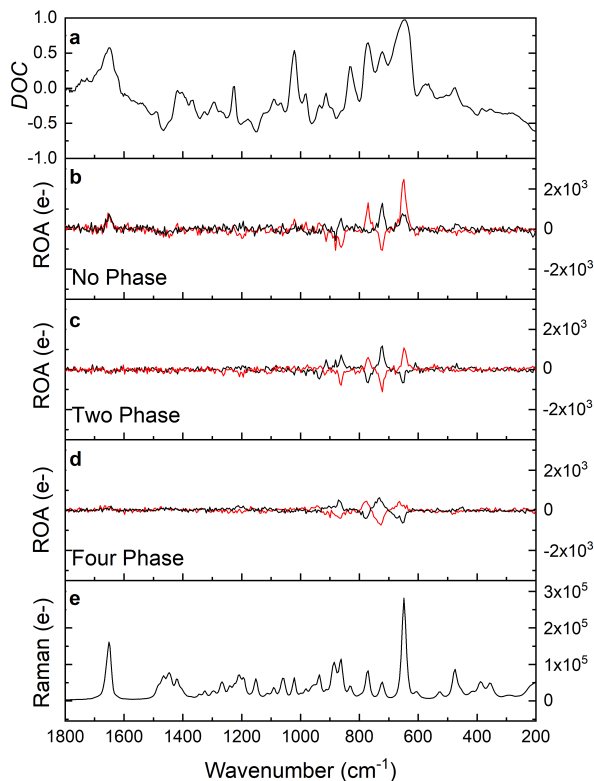
FIGURE 2.5: ROA measurements of chiral molecules with virtual enantiomer correction. (a) DOC of β-pinene. (b) ROA spectra ($I^R - I^L$) of (+)-β-pinene (black curve) and (-)-β-pinene (red curve) without any virtual-enantiomer correction (no phase). (c,d) ROA spectra ($I^R - I^L$) of (+)-β-pinene (black curve) and (-)-β-pinene (red curve) with two-phase and with four-phase virtual enantiomer correction, respectively. (e) Raman spectrum ($I^R + I^L$) of (+)-β-pinene. All measurements were taken with 1.5 W of incident laser power, 1 mL of sample volume, and 2, 4, and 8 min of measurement time, respectively, for no, two- and four-phase correction.

2.5 CONCLUSION

In this work we have demonstrated that high-frequency modulation, in the form of a PEM, can be used to measure ROA. This was made possible by using the ZIMPOL system to couple the PEM modulation to a CCD detector. The performance of this newly developed ROA instrument was compared with previous reports through measurements of the depolarization ratio and the degree of circularity. Several achiral molecules were also measured to determine the influence of chiral artifacts and offsets. The development of ROA instrumentation has lagged behind those for other chiroptical techniques because of its high sensitivity to artifacts and its requirement for spectral resolution. The instrument developed here shows that the benefits of using highly stable PEMs for polarization modulation can now be applied to ROA, greatly simplifying instrumentation and reducing measurement artifacts.
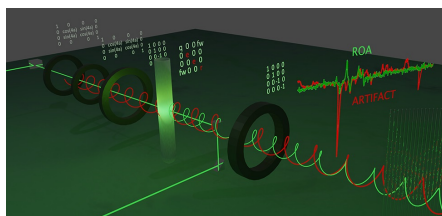
3

ARTIFACTS

3.1 ABSTRACT

The following text has been adapted from "Understanding Artifacts in Chiroptical Spectroscopy", in preparation, by Lightner et al.

The problem of polarization artifacts is ubiquitous in chiroptical spectroscopy. Unwanted polarization effects are often much larger than the weak effects being studied, leading to confusion about which spectral features belong to the effect, and which are the result of artifacts. Here, we present a comprehensive study of artifacts in Raman optical activity (ROA), one of the most challenging techniques in terms of artifact control. A Mueller-matrix model is developed, comparison of spectra across multiple ROA instruments is made and a list of essential control measurements is proposed. We show that artifact spectra can be mirror-imaged for enantiomers, debunking the idea that mirror-imaged spectra of enantiomers is proof of a functioning chiroptical set-up. It is our hope that this paper will act as a useful resource for those working in chiroptical spectroscopy and hoping to better understand how to identify and avoid the problem of artifacts.

3.2   INTRODUCTION

Though the observation of chiroptical phenomena dates back to 1811, recently this field has seen a resurgence. [6, 33–35] As the field expands, the problem of instrumental artifacts and offsets has become even more important. [17] We use the term "artifact" to refer to any circular differential signal resulting from a non-chiral effect. Artifacts and their confusion with "true" chiroptical effects has long been a challenge in chiroptical spectroscopy. [17]

Chiroptical spectroscopy exploits the tendency of enantiomers to have a different optical response to different handedness of circularly polarized light, quantified by the dissymmetry (Δ), as described previously. Any optical element that impacts the polarization on the scale of Δ has the potential to result in an artifact. [16] To put this into perspective— most linear polarizers have extinction ratios ranging from $10^{-2} - 10^{-3}$ and silver optical mirrors typically have a reflectance difference of 2% for differential polarization states. In fact, almost every conventional optical element will impact the polarization of the light more than the effect under study.

The most common forms of chiroptical spectroscopy are circular dichroism (CD) and vibrational circular dichroism (VCD). CD measures the difference absorption of left- and right-circularly polarized light incident on a sample. VCD similarly measures the differential absorption but specifically for the vibrational modes of a molecule. [36] Because both of these methods rely on incident circularly polarized light, ensuring the purity of the polarization of the incident beam is paramount to ensuring artifact-free spectra. This is typically achieved through the use of high-frequency polarization modulation and synchronized detection. [37] However, both CD and VCD are still prone to artifacts, particularly in the presence of sample anisotropy. [38, 39] The presence of circular differential optical absorption (CDOA) in anisotropic samples can also easily be confused with chiral effects, as shown by Wilson et al. [39]

Raman optical activity (ROA) can be considered the most challenging form of chiroptical spectroscopy from an artifact perspective. It is a scattering-based effect, wherein the polarization states of both the incident and scattered photons must be considered. It measures the scattering from the vibrational modes of a molecule, leading to an inherently a weak effect. Modern ROA instrumentation owes much to Werner Hug, who de-

veloped the artifact correction scheme that is used in most modern ROA instruments. [17] Hug's innovations have allowed the routine measurement of ROA using established tools. However, artifacts still present a significant problem in ROA, as in other chiroptical measurements, particularly in the construction of new instruments or the development of new measurement methods.

Though virtually every paper involving chiroptical spectroscopy mentions the problem of artifacts in spectra, very few thorough descriptions of artifact spectra exist, and no criteria for the necessary control measurements has been accepted. Using ROA as an example case, we present a theoretical approach to understanding the origin of artifacts, concrete examples of artifact spectra, a list of suggested control measurements, and comparisons to multiple existing ROA instruments.

3.3 THEORY

ROA is based on the phenomenon of Raman scattering. When light hits a molecule, the majority of the light is scattered out at the same frequency (Rayleigh scattering), a small fraction of the light is scattered inelastically, resulting in a slight frequency shift (Raman scattering). The frequencies at which peaks occur correspond to the vibrational modes in the molecule. [7] The intensity of the observed peaks is determined by the change in the electric-dipole–electric-dipole polarizability (α) over a given vibrational mode. Standard Raman scattering measures only intensity vs. wavelength and is "chiral-blind", meaning that the Raman spectra of two enantiomers will be identical. However, by measuring the circular component in the scattered light or the difference in scattering intensities with incident circularly polarized light, enantiomers can be distinguished from one another. In such measurements, the differential spectra $I_R - I_L$ will be mirrored about the y-axis for the two enantiomers.

ROA can be measured either with incident circularly polarized light (ICP), in which case the total differential intensity of light scattered from incident right- and left-circularly polarized light is measured. ROA can also be measured by examining the circular component in the scattered light (SCP) with arbitrary incident polarization. Dual-circular polarization (DCP) measurements are also possible, where both the incident and scattered polarization states are controlled/measured, but not often used. ICP and

SCP ROA measurements have been shown to give equivalent spectra in the far-from-resonance approximation. [6] An experimental choice that does result in different spectra is the angle of collection. In ROA, collecting at different angles results in different spectra. [30]. The most common angles of collection in ROA are forward- and backward-scattering, which will be the focus of the discussion here.

A useful method for understanding the polarization of light, and also the artifacts, is the Stokes-Mueller formalism. [10] Using this formalism, the polarization of light is represented by the stokes vector S, which has four components, S_0, S_1, S_2 and S_3, that satisfy Eq. 3.1.

$$S_0^2 \geq S_1^2 + S_2^2 + S_3^2 \tag{3.1}$$

S_0 represents the total intensity (I). S_1, S_2 and S_3, sometimes also denoted Q, U and V respectively, are defined according to the ellipticity angles ψ, χ and degree of polarization (P) according to Eq. 3.2, 3.3 and 3.4.

$$S_1 = S_0 P \cos(2\chi) \cos(2\psi) \tag{3.2}$$

$$S_2 = S_0 P \cos(2\chi) \sin(2\psi) \tag{3.3}$$

$$S_3 = S_0 P \sin(2\chi) \tag{3.4}$$

Eq. 3.1 is an equality when the light is fully polarized ($P = 1$). When the light is partially polarized ($P < 1$) the inequality holds. The Stokes vector can also be usefully described using a column matrix, shown below.

$$S = \begin{pmatrix} S_0 \\ S_1 \\ S_2 \\ S_3 \end{pmatrix} \tag{3.5}$$

Light which is completely unpolarized ($P = 0$) can be represented by the S_{UP}.

$$S_{UP} = \begin{pmatrix} 1 \\ 0 \\ 0 \\ 0 \end{pmatrix} \tag{3.6}$$

Partially polarized light can be represented as a combination of polarized and partially polarized light.

$$S_{partially\ polarized} = (1 - P)S_{UP} + (P)S \tag{3.7}$$

With the Stokes vectors now quantifying the polarization state of the light, we need a method to describe how various optical elements modify the polarization. Mueller matrices (MM) are 4x4 matrices that represent these optical elements. By multiplying the incident Stokes vector by the MM of the corresponding optical element, the output polarization state can be determined.

The use of Mueller matrices to understand artifacts in ROA was first introduced by Hug et al. in his seminal paper on the suppression of ROA artifacts. [17] In this paper, Hug used MMs to describe the use of rotating half-wave plates (HWP) to depolarize the incident light and the use of HWPs to create virtual enantiomers. Together, the depolarization of incident light and the use of virtual enantiomers represent the two most important innovations in artifact suppression. These tools allow for the routine measurement of ROA across several instrument variations today. In this work, we expand upon Hug's use of MMs by proposing MMs which represent Raman and ROA scattering.

The Stokes vectors of Raman-scattered light from a chiral molecule for forward-scattering (S_{FS}^R) and back-scattering (S_{BS}^R) in terms of the fundamental property tensors, and the ellipticity (χ and ψ) and degree of polarization (P) of the incident light are shown below. [7]

$$S_{FS}^R = \begin{pmatrix} \frac{\left(45a^2+7\gamma^2\right)+\left(\frac{4}{c}\right)\left(45aG'+\gamma_{G'}^2-\gamma_A^2\right)PS_0\sin[2\chi]}{45} \\ \frac{\left(45a^2+\gamma^2\right)PS_0\cos[2\chi]\cos[2\psi]}{45} \\ \frac{\left(45a^2+\gamma^2\right)PS_0\cos[2\chi]\sin[2\psi]}{45} \\ \frac{\left(45a^2-5\gamma^2\right)PS_0\sin[2\chi]+\left(\frac{4}{c}\right)\left(45aG'+\gamma_{G'}^2-\gamma_A^2\right)}{45} \end{pmatrix} \tag{3.8}$$

$$S_{BS}^R = \begin{pmatrix} \frac{\left(45a^2+7\gamma^2\right)+\left(\frac{8}{c}\right)\left(3\gamma_{G'}^2+\gamma_A^2\right)PS_0\sin[\chi]}{45} \\ \frac{\left(45a^2+\gamma^2\right)PS_0\cos[2\chi]\cos[2\psi]}{45} \\ \frac{-\left(45a^2+\gamma^2\right)PS_0\cos[2\chi]\sin[2\psi]}{45} \\ \frac{-\left(45a^2-5\gamma^2\right)PS_0\sin[2\chi]+\left(\frac{8}{c}\right)\left(3\gamma_{G'}^2+\gamma_A^2\right)}{45} \end{pmatrix} \tag{3.9}$$

These equations are written in terms of five tensor invariants of the molecular-scattering tensors (α, G' and A). The terms a^2 and γ^2 are the isotropic and anisotropic invariants of the electric-dipole–electric-dipole polarizability α, respectively. For achiral molecules only the α term contributes to scattering, but because chiral molecules are less symmetric, the higher order interaction terms A and G must also be considered. [6] A is the electric-dipole–electric-quadrupole interaction term and G is the electric-dipole–magnetic-dipole interaction term, both of which contribute to scattering from chiral molecules. The invariants aG', $\gamma_{G'}$ and γ_A are the the isotropic (aG') and anisotropic ($\gamma_{G'}$, γ_A) invariants of of the G and A terms. It should be noted that the most comprehensive understanding of Raman scattering from chiral molecules requires the consideration of the total 26 possible tensor invariants. Here we simplify to only 5 invariants, which is most valid for lower energy vibrational modes. This simplification is more than sufficient for our goal of understanding chiral artifacts. [7] We also note that Eqs. 3.8 and 3.9 are preceded by a factor relating to the total intensity, which can be found in Ref. 13, we leave out this term here for brevity.

Eqs. 3.8 and 3.9 give the expected Stokes vectors for forward and backward ROA scattering, but to use the Stokes-Mueller formalism to understand artifacts, we must first put the sample in terms of a Mueller matrix. Starting from Mueller matrices for back- and forward-scattering from asymmetric particles (from Savenkov et al.), and combining them with the Stokes

vectors in Eqs. 3.8 and 3.9, we can derive Mueller matrices which represent samples. [40] Eq. 3.10 represents the Mueller matrix for Raman and ROA scattering from a sample in the forward direction and Eq. 3.11 represents the same in back-scattering. Details of the derivation are in the appendix.

$$MM^R_{FS} = \begin{pmatrix} q & 0 & 0 & fw \\ 0 & e & 0 & 0 \\ 0 & 0 & e & 0 \\ fw & 0 & 0 & r \end{pmatrix} \tag{3.10}$$

$$MM^R_{BS} = \begin{pmatrix} q & 0 & 0 & bw \\ 0 & e & 0 & 0 \\ 0 & 0 & -e & 0 \\ bw & 0 & 0 & -r \end{pmatrix} \tag{3.11}$$

q term represents the total intensity of the scattering (ie. the $I_R + I_L$ term) and is defined in terms of tensor invariants as

$$q = a^2 + \frac{7\gamma^2}{45} \tag{3.12}$$

fw and bw represent the ROA scattering and in terms of the tensor invariants are

$$fw = \frac{4(45aG' - \gamma_A^2 + \gamma_{G'}^2)}{45c} \tag{3.13}$$

$$bw = \frac{8(\gamma_A^2 + 3\gamma_{G'}^2)}{45c} \tag{3.14}$$

"True signal" here is considered to be signal which originates from these two terms. e and r are common in both matrices and are perhaps the most important for understanding artifacts. In the context of this paper, we will refer to e as "linear depolarization" and r as "circular depolarization".

$$e = \frac{45a^2 + \gamma^2}{45} \tag{3.15}$$

$$r = a^2 - \frac{\gamma^2}{9} \tag{3.16}$$

As shown in Eqs. 3.15 and 3.16, both terms relate only to the achiral invariants a and γ but, as we will show in the following section, can be measured in the circular component of the scattered light and easily confused with "true" signal originating from fw or bw.

3.4   RESULTS

To test the sample Mueller matrices proposed in the previous section, we examine if they can be used to approximate artifact signal in experimental systems. First, the simplest case of an "artificial" artifact spectrum is examined. Eq. 3.17 shows the Mueller matrix equation for a circular polarizer placed immediately after the sample and before the detector. All of the examples going forward will use the forward-scattering sample Mueller matrix unless otherwise noted.

$$\underbrace{\begin{pmatrix} q \\ 0 \\ 0 \\ q \end{pmatrix}}_{output} = \underbrace{\begin{pmatrix} 1 & 0 & 1 & 0 \\ 0 & 0 & 0 & 0 \\ 0 & 0 & 0 & 0 \\ 1 & 0 & 1 & 0 \end{pmatrix}}_{circular\ polarizer} \cdot \underbrace{\begin{pmatrix} q & 0 & 0 & fw \\ 0 & e & 0 & 0 \\ 0 & 0 & e & 0 \\ fw & 0 & 0 & r \end{pmatrix}}_{sample} \cdot \underbrace{\begin{pmatrix} 1 \\ 0 \\ 0 \\ 0 \end{pmatrix}}_{input} \tag{3.17}$$

Eq. 3.17 shows that a circular polarizer after the sample converts the circular signal (S_3, the final term in the output stokes vector) into the q term, which represents the total intensity. This means that, in the equivalent experimental measurement, the circular ($I_R - I_L$) signal should be equivalent to the Raman ($I_R + I_L$) signal. This is confirmed with the experimental results shown in Figure 3.1. Figure 3.1 (a) shows the resulting circular signal ($I_R - I_L$) with a circular polarizer placed after the sample for the molecule β-pinene. Figure 3.1 (d) shows the same measurement for an achiral molecule, toluene. In both instances the circular spectra perfectly mimics the Raman ($I_R + I_L$) signal shown in Figure 3.1 (c) and (d), respectively.

The second test case is a circular polarizer before the sample, effectively converting the depolarized incident light to circularly polarized incident light. This scenario is shown in terms of Mueller matrices as

$$
\underbrace{\begin{pmatrix} q+r \\ 0 \\ 0 \\ r+fw \end{pmatrix}}_{output} = \underbrace{\begin{pmatrix} q & 0 & 0 & fw \\ 0 & e & 0 & 0 \\ 0 & 0 & e & 0 \\ fw & 0 & 0 & r \end{pmatrix}}_{sample} \cdot \underbrace{\begin{pmatrix} 1 & 0 & 1 & 0 \\ 0 & 0 & 0 & 0 \\ 0 & 0 & 0 & 0 \\ 1 & 0 & 1 & 0 \end{pmatrix}}_{circular\ polarizer} \cdot \underbrace{\begin{pmatrix} 1 \\ 0 \\ 0 \\ 0 \end{pmatrix}}_{input} \tag{3.18}
$$

The circular component in the output stokes vector in Eq. 3.18 is the sum of r, the circular depolarization term and fw, the ROA term. Because ROA scattering is so weak compared to its achiral equivalent, most of the signal here comes from the r term. Figure 3.1 (b) shows the resulting signal with the chiral molecule β-pinene and Figure 3.1 (e) shows the results for the achiral molecule toluene. Interestingly, in both cases non-unidirectional flipping of the difference $(I_R - I_L)$ spectra occurs. This is because, as shown in Eq. 3.16, the r term is proportional to the difference of the a and γ terms, meaning that for vibrational modes that have a stronger contribution from the anisotropy (γ) the circular signal will be negative. This explains an important concept in chiroptical artifacts— that circular signal can be the result of linear anisotropy rather than the chirality of the molecule.

This test case illustrates the importance of measuring the degree of circularity (DOC) for each molecule. The DOC is the ratio of the difference over the sum of light scattered from the molecule with incident circularly polarised light. Eq. 3.19 shows the DOC for forward ($0°$) scattered light with incident right-circularly polarized light (I_R^i) in terms of the left- and right-circularly polarized light scattered out (I_L^s, I_R^s). [6]

$$
DOC(0°, I_R^i) = \frac{I_R^s - I_L^s}{I_R^s + I_L^s} \tag{3.19}
$$

In the context of artifacts, the DOC is proportional to $\frac{r}{q}$, meaning that vibrational modes with high DOC values are likely to have a strong contribution from the circular depolarization term (r). Somewhat confusingly,
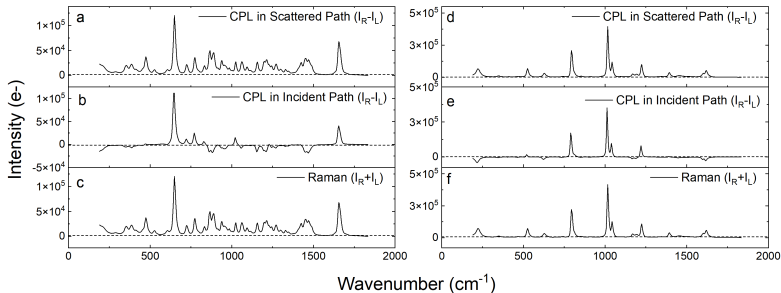
FIGURE 3.1: (a)-(c) Spectra of (-)-β-pinene and (d)-(e) spectra of toluene. (a) and (d) are spectra measured with a circular polarizer in the scattered path, immediately before the detector. (b) and (e) are measured with a circular polarizer in the incident path, immediately before the sample, (c) and (f) are the Raman spectra of (-)-β-pinene and toluene, respectively. All spectra are a measured on the forward-scattering Z-ROA instrument with 532 nm excitation

these modes are generally referred to in Raman as "strongly polarized" modes. [7]

Reducing the contribution of the r term is relatively simple when we use our Mueller matrix understanding of the sample. For perfectly depolarized light ($S = 1, 0, 0, 0$) the contribution of the r term is zero.

$$
\underbrace{\begin{pmatrix} q \\ 0 \\ 0 \\ fw \end{pmatrix}}_{output} = \underbrace{\begin{pmatrix} q & 0 & 0 & fw \\ 0 & e & 0 & 0 \\ 0 & 0 & e & 0 \\ fw & 0 & 0 & r \end{pmatrix}}_{sample} \cdot \underbrace{\begin{pmatrix} 1 \\ 0 \\ 0 \\ 0 \end{pmatrix}}_{input}
\tag{3.20}
$$

This realization is indeed what Hug et al. emphasized in his paper, where he suggested the use of two counter-rotating half-wave plates to create "depolarized" light from an incident laser. [17]

However, in reality, because light is never completely unpolarized, artifacts are still present in ROA spectra. Figure 3.2 shows uncorrected ROA

spectra from several instruments. Figure 3.2 (a) and (b) shows the ROA spectra of β-pinene from forward-scattering instruments in Zurich and Geneva, respectively (see appendix). Figure 3.2 (c) and (d) shows β-pinene spectra from back-scattering instruments in Antwerp and Geneva, respectively. Because the spectrum is not fully dominated by artifacts, the artifact features can be identified in these spectra as the features which are not mirror-imaged for enantiomers. The spectra all show clear artifacts at ca. 640 cm^{-1}, which is a "strongly polarized" mode, and has a large contribution from the r term. Other than the few features strongly polarized modes, the spectra are mirrored for the enantiomers.
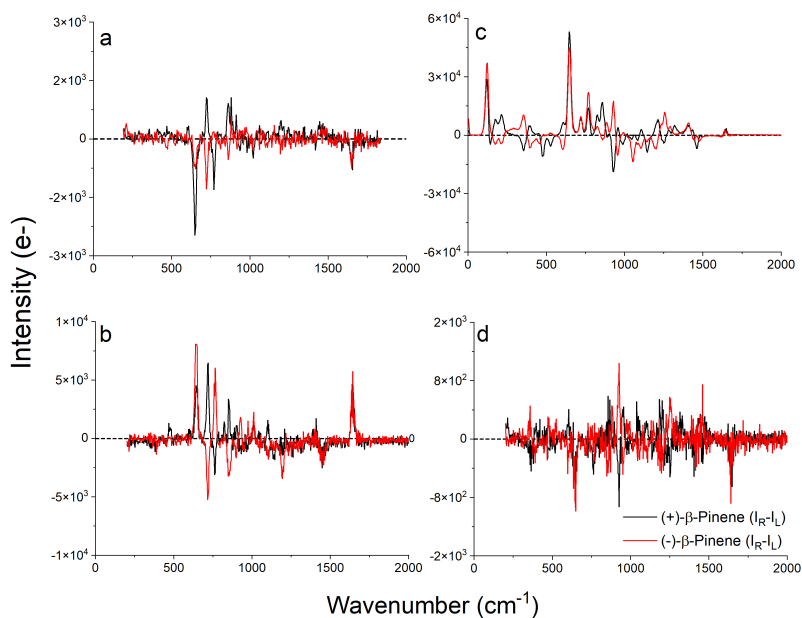

FIGURE 3.2: Uncorrected ROA spectra of (+/-)-β-pinene from three separate instruments: (a) Z-ROA (b) G-ROA-FW , (c) A-ROA-Holo, and (d) G-ROA-BW. (a) and (b) are forward-scatting instruments; (c) and (d) are back-scattering. All instruments use 532 nm excitation. The instrument details are given in the appendix.

These artifacts can be corrected by using Hug's virtual enantiomer scheme (VE), which involves moving a series of half-wave plates in and out of the

optical path to reverse the sense of polarization and then subtracting the measurements from one another to obtain the corrected spectra. [17] The appendix shows the virtual enantiomer correction scheme in terms of Mueller matrices. Figure 3.3 shows the virtual enantiomer corrected spectra of β-pinene for four separate instruments: (a) and (b) in forward-scattering and (c) and (d) in back-scattering. All except (a) use four-phase virtual enantiomer correction; (a) uses only two-phase virtual enantiomer correction.
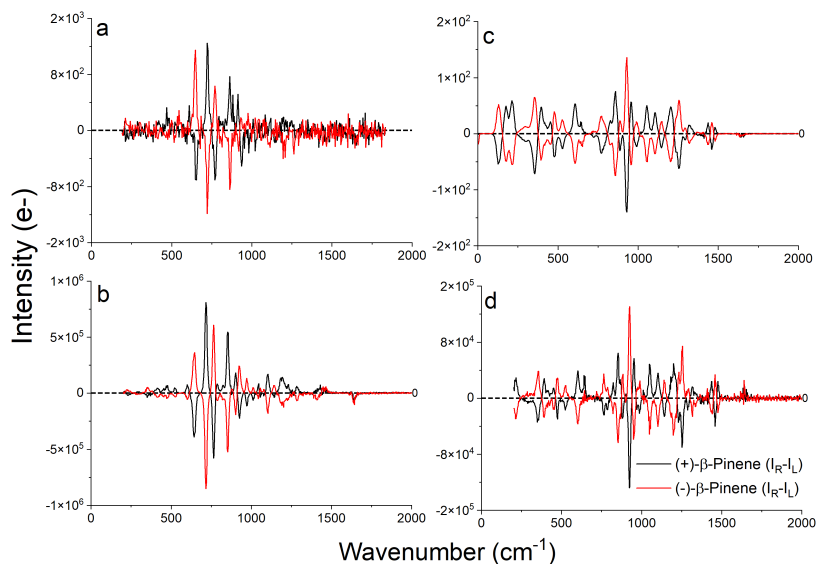

FIGURE 3.3: Corrected ROA spectra of (+/-)-β-pinene from three separate instruments (a)Z-ROA, (b)G-ROA-FW , (c)A-ROA-Holo, and (d)G-ROA-BW. (a) and (b) are forward-scatting instruments , (c) and (d) are back-scattering. All instruments use 532nm excitation. All instuments except the ZROA are four-phase corrected, ZROA is corrected with 2-phases.

Figure 3.3 illustrates the general effectiveness of virtual enantiomer correction. However, it is not fool-proof. Because half-wave plates are not perfect, cases exist when VE correction is not enough. When a realistic retardation error is included in the Mueller matrix model, both the circular and the linear depolarization terms can contribute to the circular signal in the output, according to

$$S_3^{out} \propto -fw + (-0.001e + r)P\sin(2\chi) - 0.03(e+r)P\cos(2\chi)\sin(2\psi)$$
(3.21)

The contribution due to incident circularly and linearly polarized light can also be shown in terms of the mean polarizability (a), anisotropy (γ), the ellipticity angles χ and ψ and the degree of polarization (P)

$$S_3^{out} \propto -fw + \underbrace{(a^2 - 0.1\gamma^2)P\sin(2\chi)}_{circular\ polarization} + \underbrace{(-0.004\gamma^2)P\cos(2\chi)\sin(2\psi)}_{linear\ polarization}$$
(3.22)

Because the ROA term (fw) is generally 3-4 orders of magnitude lower than the contribution from the achiral tensor invariants (a and γ), incident light that is fully circularly polarized ($\chi = \frac{\pi}{4}, P = 1$) or linearly polarized ($\chi = 0, \psi = \pi, P = 1$) would lead to the circular signal in the scattered light being dominated by the ($a^2 - 0.1\gamma^2$) and ($-0.004\gamma^2$) terms, respectively. This indicates that artifact spectra (spectra arising from achiral tensor invariants) for incident light with a small degree of linear polarization is significantly less than for incident light with a circularly polarized component because the LP term in Eq. 3.22 scales by 0.004 rather than 0.1. This also means that even with the use of virtual enantiomers, the ROA spectra of enantiomers measured with completely polarized incident light would reflect only the contributions from the achiral tensor invariants. Figure 3.4 shows the experimental result when the ROA ($I_R - I_L$) spectra of (+/-)-β-pinene are measured with incident light that is fully circularly polarized. The spectra are identical, because they are dominated by the contributions from the achiral tensor invariants (a and γ) which is the same for both enantiomers.
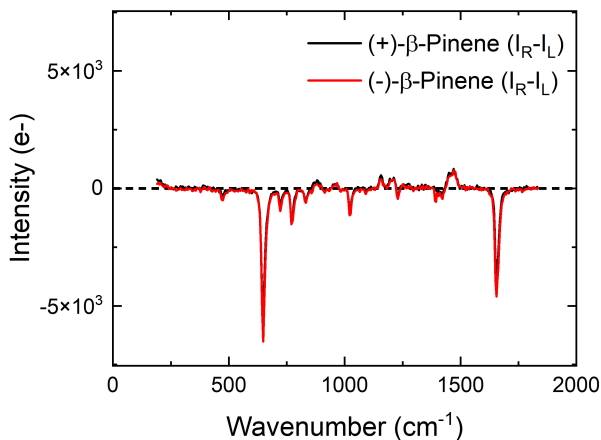
FIGURE 3.4: The $(I_R - I_L)$ spectra of $(+/-)$-β-pinene with (a) incident circularly polarized light. Measured using two-phase virtual enantiomer correction in a forward scattering, SCP configuration with 532 nm excitation on the ZROA instrument.

A more likely scenario in terms of artifacts is when a very small degree of circular polarization is present, due to some unwanted birefringence in an optical element. Because rotating half-wave plates are used in ROA instruments, it is also likely that the overall polarization state is not constant in time, creating artifact spectra that are very difficult to identify. To simulate this type of artifact spectra, a quarter-wave plate was placed in the incident path, before the sample, and the rotators used to create the depolarized incident light were slowed to 10rpm. Figure 3.5 shows the result for three molecules. It is possible to identify the spectra in Figure 3.5 as artifact spectra *only* because we can compare it with other measured ROA spectra and various theoretically predicted spectra in the literature. [30] While the spectra of the enantiomers are mirror images of one another, the intensity pattern of the peaks reflects the circular depolarization term (r) rather than the ROA scattering term fw.

The artifact spectra in Figure 3.5 are repeatable, but not reliable, meaning that if the same measurement is taken five times, only ca. three results would resemble the spectra shown, because it depends on the timing between the measurements and the virtual enantiomers. However, this artifact

can be demonstrated across several molecules, and looks very much like the mirror image spectra that are expected for ROA scattering, making it a particularly difficult artifact to identify.
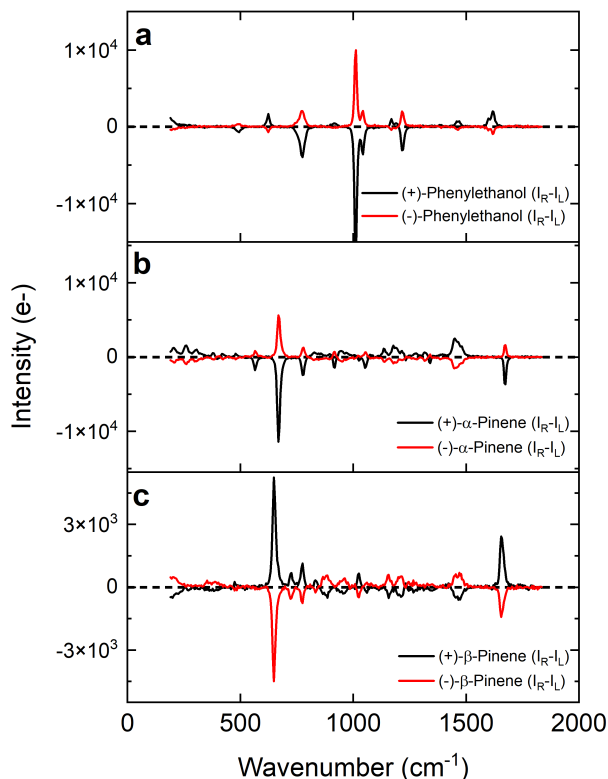

FIGURE 3.5: The $(I_R - I_L)$ spectra of (+/-)-phenylethanol (a), (+/-)-α-pinene (b) (+/-)-β-pinene measured with a small, time-varying degree of circularity in the incident light. Measured using two-phase virtual enantiomer correction in a forward-scattering SCP configuration, with 532 nm excitation on the ZROA instrument. All spectra are two-phase virtual enantiomer corrected.

Figures 3.4 and 3.5 show that even with virtual enantiomer correction artifacts still occur, and even mimic the mirror-imaged peaks imaging of true ROA spectra. In fact, the mirror-imaged spectra shown in Figure 3.5

can only be proven to be artifact spectra by comparing them with existing experimental and simulated ROA spectra. These results indicate the importance of establishing a clear criteria for validating ROA results, especially when new experimental set-ups are used.

3.5 DISCUSSION

As shown in the previous section, artifact spectra that are the result of interaction with the sample can be difficult to differentiate from "true" signal. To help researchers to distinguish true spectra from artifact spectra, we have collected data from different ROA instruments across several research groups. All of the tools used are in SCP, with 532 nm laser excitation. For a comprehensive list of the tools involved, as well as experimental details, see the appendix. Here, we first compile a list of common features of spectra dominated by artifacts, and we then propose a list of suggested control measurements with key comparisons across several instruments.

Several spectral characteristics can indicate that the signal is arising from an artifact. The list below includes the most common of these characteristics, as well as brief explanations.

- Unidirectional flipping of the peaks.

  EXPLANATION: If all of the peaks are in the same direction, this is a possible indicator of an artifact in the collection path (see Figure 3.1 (a) and (b)).

- The peak intensity mimics the Raman spectrum.

  EXPLANATION: If the strongest and weakest peaks in the "ROA" spectra are the same as the strongest and weakest peaks in the Raman, this is likely artifact spectra. The ROA peak intensities should be independent of the Raman peak intensities (see Figure 3.1).

- The intensity of the ROA spectra is not at least three orders of magnitude weaker than the Raman spectrum.

  EXPLANATION: In the case of standard ROA (no surface enhancement or other effects), the magnitude of the ROA signal should be at least three orders of magnitude weaker than the Raman

signal. If this is not the case, the signal is likely arising from the circular depolarization term.

In addition to checking measured spectra for the features listed above, we suggest that the following list of controls should be measured on any new instrument or on older instruments to periodically check that they are functioning as they should.

- **Achiral DOC**: DOC should be measured using incident circularly polarized light for either carbon tetrachloride or toluene. The absolute values for the peaks should be reported and compared against other instruments, as shown in Table 3.1.

No.	Instrument	Toluene (1012 cm^{-1})	Toluene (630 cm^{-1})	Toluene (1590 cm^{-1})	CCl$_4$ (316 cm^{-1})	CCl$_4$ (460 cm^{-1})
1	G-ROA-FW	0.822	-0.643	-0.654	-0.675*	0.963*
2	Z-ROA	0.936	-0.643	-0.660	-0.693	0.994
3	G-ROA-BW	-0.537	0.627	0.626	0.645	-0.919
4	A-BT-ChiralRaman2x	--	--	--	--	--
5	A-ROA-Holo	-0.753	0.486	0.445	0.622	-0.883
6	A-ROA-Kym	0.796	-0.507	-0.482	-0.605	0.876

TABLE 3.1: Values of the DOC of toluene at three vibrational modes and two modes of carbon tetrachloride (CCl_4) are shown for six different instrument configurations. The details of each instrument and measurement conditions is given in the appendix. *These values are taken from literature. [30]

- **Achiral Spectra with Error**: The spectra ($I_R - I_L$) of toluene should be measured and compared against the error (square-root of the Raman signal). In theory, the signal from an achiral molecule should be zero, but, as shown in Figure 3.6, this can vary widely across instruments. This measurement is a good indication of the expected contribution from the circular depolarization term.
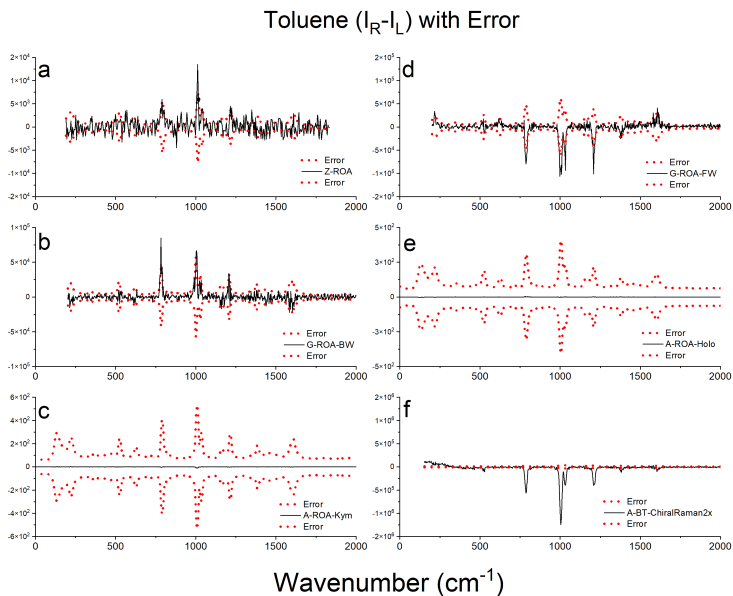
FIGURE 3.6: The $(I_R - I_L)$ spectra of toluene measured with six different instrument configurations, Z-ROA and G-ROA-FW are forward-scattering instruments, the others are measured in back-scattering. All spectra except that from the Z-ROA are measured with virtual enantiomer correction.

- **Chiral Spectra of Enantiomers**: The spectra of neat $(+/-)$-β-pinene should be measured and compared with data from other instruments in the same configuration (as shown in Figure 3.3). If no other similar configuration exists, then the data should be compared to simulated spectra. Since β-pinene is well studied and widely available in a high-quality neat solution, it represents an ideal control molecule.

These control measurements not only verify that a measurement is "true" signal, they also provide valuable insight into instrument performance and calibration. Different instruments often have slightly different efficiencies when dealing with certain polarization states, the small variations in Table 3.1 are likely due to this. Large variations can indicate that an instrument is not properly calibrated. Likewise, the variations in signal-to-noise shown in Figure 3.6 indicate the base level of polarization offset. The large signal seen from achiral toluene in Figure 3.6 (f) is from an older version of the commercial "ChiralRaman" instrument. The base level of polarization offset

here is much larger, probably due to the age of the instrument, but small enough to still be corrected by virtual enantiomers. If only the corrected spectra of chiral molecules was measured, there would be no indication that the baseline offset is high. Measuring the achiral control periodically acts as a check on instrument performance, so that improvements can be made before the offset level rises high enough to noticeably impact the spectra of chiral molecules.

In addition to the above controls, we also recommend that the DOC is measured and reported together with the ROA spectra as standard practice, since modes with the highest DOC values will have the highest contribution to the circular depolarization term. These relatively simple control measurements can act as a standard method to validate measurements from new instruments. Moreover, they allow measurements from different established instruments, to be compared, ensuring that spectra from artifacts are not mistakenly published as true spectra.

3.6 CONCLUSION

Here we have examined the issue of artifacts in chiroptical spectroscopy using ROA as an example case. As a weak effect with influence from sample anisotropy, ROA represents an ideal case to understand and study the issue of artifacts in chiroptical spectroscopies. First, we established a theoretical framework using Stokes-Mueller calculus to understand how the sample anisotropy in the form of the achiral tensor invariants contributes to circular signal in the scattered light. Then, we demonstrated the usefulness of this framework by simulating artifacts and comparing the results with experimentally measured spectra. Finally, we showed that certain artifacts can not be corrected by using conventional methods, leading instead to mirror-imaged spectra of enantiomers which are the result of artifacts. To avoid future reports of artifact spectra in the literature, we suggest several simple control measurements that can be used to validate results from new set-ups. It is our hope that, by demystifying artifacts and providing clear examples and control measurements, groups entering the field can have a better understanding of how to test for and avoid artifacts.

ENHANCEMENT

Say not the struggle nought availeth,
The labour and the wounds are vain,
The enemy faints not, nor faileth,
And as things have been they remain.

— A. H. Clough

4.1 ABSTRACT
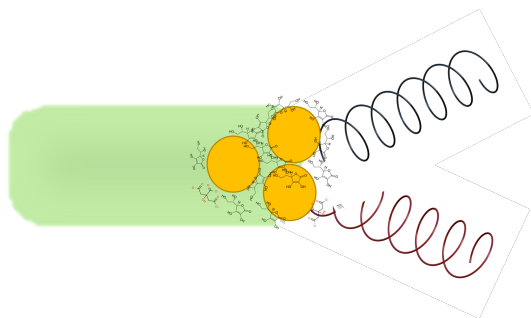
Despite advances in instrumentation and artifact suppression, the measurement of Raman optical activity (ROA) remains limited by the low ROA-scattering cross-section. Long measurement times and high laser powers are still the norm in ROA experiments, reducing potential applications. The use of surface enhancement to increase the ROA signal has long been a dream of ROA researchers. However, the application of experimental methods and theory from surface-enhanced Raman spectroscopy (SERS) theory and experimental methods to ROA presents several challenges. To date, only a few groups have successfully demonstrated so-called "SEROA", and none have demonstrated it in forward-scattering. Here, we discuss the experimental and theoretical challenges in SEROA measurements, present initial proof-of-concept measurements in forward-scattering, and outline a path to more reliable SEROA signals.

4.2   INTRODUCTION

Since the earliest reports of ROA, researchers have speculated that surface enhancement could be used to boost the naturally weak ROA signal. [41] However, the experimental realization of surface-enhanced ROA (SEROA) has proven more difficult, and while a few reports of SEROA have been published, it remains far from a routine measurement. [42–45] The reasons for the experimental hurdles are varied, but challenges relating to low signal and additional artifact errors have played a major part.

The simplest experiment to demonstrate SEROA is to measure a chiral molecule adsorbed onto a silver or gold surface. However, this simple Raman experiment already presents challenges for ROA. ROA is traditionally performed in solution. Solution-based measurements are advantageous for ROA because they allow for much higher sample volumes and for the use of higher laser powers without sample damage, can lead to sufficient signal to measure the weak ROA spectrum. Measuring ROA on a surface not only significantly reduces the effective measurement volume but also necessitates the use of lower laser powers, meaning that any surface-enhancement effect would need to overcome both of these significant reductions in signal. This has led most SEROA reports to use dispersions of gold and silver nanoparticles, a system which is more similar to those employed in traditional (solution-based) ROA measurements. [43, 44]

Unfortunately, measuring SEROA in a dispersion of nanoparticles presents its own challenges. The nanoparticles move freely in solution, meaning that the measurements can vary in time. Pour et al. solved this problem by using a hydrogel to "freeze" the silver particles in place and were able to successfully measure SEROA spectra of D- and L- ribose. [43] A related issue is the proximity of the analyte molecule to the metal surface. The enhancement of signal decreases exponentially with the distance from the metallic surface. [46] While this can be partially solved using Pour's method of hydrogel immobilization combined with high concentrations of the analyte, it still presents an additional reduction of signal. Other groups have exploited the use of linker molecules to attach the analyte to the metal nanoparticles. [44, 47] Despite these advances, the measurement of SEROA in solution still requires careful sample preparation to ensure that particles and analytes are relatively stable with time.

A few attempts at measuring SEROA directly on surfaces have been made, including a recent report of an all-dielectric SEROA substrate designed to selectively enhance the ROA signal. [48] However, even in this system measurement times of five and six hours were required. Additionally, because the instrument performance in this particular case was not verified with a reference ROA spectrum, it is difficult to rule out artifacts. Once surfaces are used, parameters like layer thickness, and orientation of the film stack also need to be carefully considered, since both of these effects can induce or enhance chirality. [49, 50]

The experimental reports of SEROA so-far have relied on the more common ROA experimental configurations, particularly back-scattering SCP or ICP based systems (see Chapter 2 for a description of these approaches). [43, 44] Because the contribution of the different scattering tensors in ROA vary based on the angle of collection, reports of SEROA in different measurement geometries could be useful in better understanding the origin of the effect and its interaction with the ROA scattering terms. [6] Here, we report ROA spectra of molecules in the presence of metallic nanoparticles, measured in forward-scattering, and examine the potential sources of this "SEROA" signal.

4.3   THEORY

Surface-enhanced Raman spectroscopy, known as SERS, was first reported in 1974 by Fleischman et al. [51] Traditional SERS relies on the enhanced localized electromagnetic field at a metallic surface caused by localized surface plasmon resonances (LSPR). Often, "chemical enhancement" is also listed as a contributor to the SERS effect, but is generally not well defined, and it is sufficient to say that close contact with the metal surface as facilitated by surface binding, increases the signal further. [52] The presence of these plasmonic resonances, particularly in nanoparticle aggregates or structured metallic surfaces, gives rise to dramatically increased Raman signal. [46] The main contributors to SERS signals are the plasmonic "hot-spots", which occur at junctions between metallic surfaces, leading to an area of very high field enhancement. [46]

Transferring the theory of SERS enhancement to ROA is not trivial. The introduction of higher-order scattering terms arising from the electric-dipole–

electric-quadrupole (A) polarizability and the electric-dipole–magnetic-dipole polarizability (G), in addition to the inherent polarization sensitivity and small signal of ROA, introduces considerable complexity. But before the enhancement of the ROA effect can be studied, the general considerations of measuring chirality at a surface must be examined.

Figure 4.1 shows a graphical representation of the possible modes of enhancement when discussing measurement of chirality at surfaces. The first important distinction is between enhanced chirality and induced chirality. Enhanced chirality is defined as the enhancement of a signal from chiral molecules that can be measured also with no surface present (i.e. in solution). Induced chirality refers to the phenomena that molecules that are achiral in three dimensions can become chiral when absorbed on a surface. [50] Typically, this phenomenon occurs in such a way that equal numbers of the left-handed and right-handed adsorbates form on the surface, but it is an important phenomenon to keep in mind, especially when measuring small numbers of molecules or single molecules at surfaces. Chirality can also be induced as a result of film thickness or macro-molecular ordering at the surface. [49, 50]
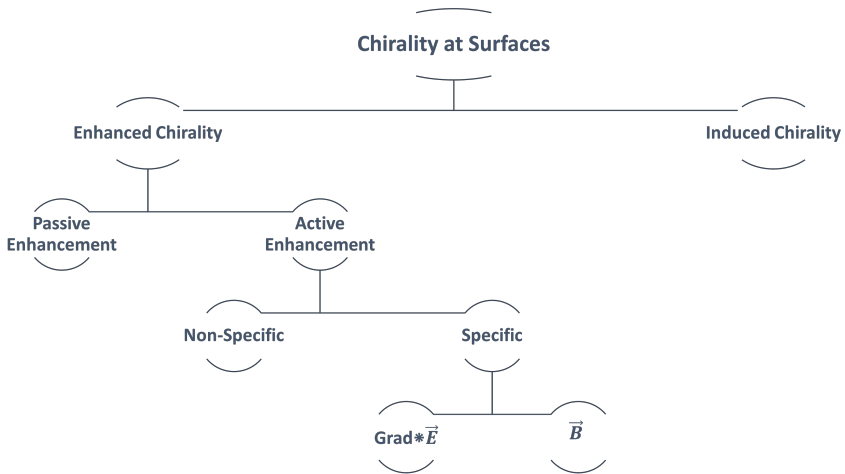
FIGURE 4.1: Illustrated diagram of the possible modes of "enhancement" of chirality at a surface.

Under the umbrella of enhanced chirality we can make another distinction between passive and active enhancement. Here again, the distinction is subtle but important. Passive enhancement refers to an increase of the chiral signal that occurs from anisotropic ordering at a surface. Sidler et al. showed that for vibrational circular dichroism (VCD), a sister-technique of ROA, the electric-dipole–electric-quadrupole term (A) is strongly enhanced when the sample is anisotropic. [53] This raises the possibility that because of the orientation on the surface, the ROA signal could be enhanced through the increased contribution of the A term. This type of enhancement of the ROA signal would occur independent of the surface material properties.

Finally, we arrive at active enhancement, which is enhancement of the ROA or chiral signal because of its interaction with an active surface. Here, an active surface is taken to be any surface specifically designed to interact with the incident or scattered field. Non-specific active enhancement occurs at a plasmonic surface that is not designed to specifically enhance the chiral signal. For instance, a standard SERS substrate will enhance the incident and scattered electric field as shown in Eq. 4.1, and thus the Raman and

ROA signal together. [46] The intensity of the SERS signal is shown in Eq. 4.1 as I_{SERS} , and is a function of the incident electric field $E_{\omega inc}$. [54]

$$I_{SERS} \approx |E(\omega_{inc})|^4 \qquad (4.1)$$

The real part of the oscillating electric dipole moment induced by an incident electric field is given by: [26]

$$\mu_\alpha = \underbrace{\alpha_{\alpha\beta}E_\beta}_{Raman} + \underbrace{\frac{2\pi c}{\lambda}G'_{\alpha\beta}\dot{B}_\beta + \frac{1}{3}A_{\alpha\beta\gamma}\nabla_\beta E_\gamma}_{ROA} \qquad (4.2)$$

Where μ_α is the induced dipole, $\alpha_{\alpha\beta}$ is the electric-dipole–electric-dipole polarizability, G is the electric-dipole–magnetic-dipole polarizability, and A is the electric-dipole–electric-quadropole polarizability. c is the speed of light, λ the wavelength, and E and B are the electric and magnetic field, respectively. The oscillating dipole, along with the other induced multipoles, are responsible for the emitted light. Signal that enhances only the E field would be classified as "non-specific". In this case, non-specific means that it would enhance either the Raman term only, or both the Raman and ROA terms, rather than selectively enhancing only the ROA terms.

"Specific" enhancement would selectively enhance the ROA scattering terms, either through enhancement of the B field or the ∇E field. This could be a surface designed to increase the gradient of the electric field, as proposed by Efrima et al., or a dielectric surface designed to enhance the magnetic field, as proposed by Xiao et al. [41, 48] Both of these forms of enhancement would act only on the optical activity tensors A and G, respectively, instead of enhancing only the general electric-field terms. Specific enhancement would then be expected to increase the ROA signal relative to the Raman signal.

The complex origin of SEROA signals also highlights the potential usefulness of SEROA as a probe of local-fields. Through the measurement of ROA from multiple scattering angles, the contributions from the different scattering terms can be isolated. [55] This unique functionality of ROA could be used to study the complexities of local field enhancement. As a first step, the measurement of SEROA from additional scattering angles is necessary.

4.4 EXPERIMENTAL METHODS

In addition to the complicated theoretical considerations of SEROA measurements, the practical limitations make the actual realization of SEROA measurements challenging. Here, we report the measurement of forward-scattered ROA spectrum of several molecules in the presence of silver and gold nanoparticles in dispersions. While these results demonstrate increased circular signal in the presence of nanoparticles, they also demonstrate the challenges with repeatability when using colloidal solutions as plasmonic substrates. The results here should be taken as a preliminary proof-of-concept only, in need further work to fully understand the system. Nonetheless, these results are a useful demonstration that forward-scattering ROA experiments can be used to contribute to the understanding of SEROA.

The citrate-stabilized gold and silver nanoparticles were prepared as described in the literature. [43, 56] Briefly, solutions of chloroauric acid (for gold nanoparticles) or silver nitrate (for silver nanoparticles) were boiled and sodium citrate was added drop-wise. The size of the particles could be controlled through the ratio of citrate added. Once made, the solutions were stored in the dark at 4°C. The silver nanoparticles were aggregated slightly through the addition of K_2SO_4 before measurements to increase the presence of hot-spots. This aggregation also meant that these dispersions were generally less stable with time. The gold nanoparticles were used as prepared. [47] Altering the size and shape of the particles would of course have an impact on the enhancement effects, but these effects were not explored here.

4.5 RESULTS AND DISCUSSION

To determine if signal enhancement could be observed in forward-scattered ROA, we focused on two systems: dispersions of nanoparticles and nanoparticles immobilized in hydrogels. Some enhancement was observed, but the signal in the case of the dispersions was, as expected, very unstable. The hydrogel system showed ROA signal, and was stable with time but needs additional study to increase the interaction of the nanoparticles with the analytes and thus the enhancement.

4.5.1 *Measurement of Colloidal Solutions*

Figure 4.2 shows the Raman and ROA spectra of D-ribose in the presence of both gold (AuNP) and silver (AgNP) nanoparticles. The signal is highest from the control sample D-ribose in a water solution for both the Raman and ROA spectra. This indicates that the ribose molecules are not interacting enough with the nanoparticles to benefit from the plasmonic enhancement.
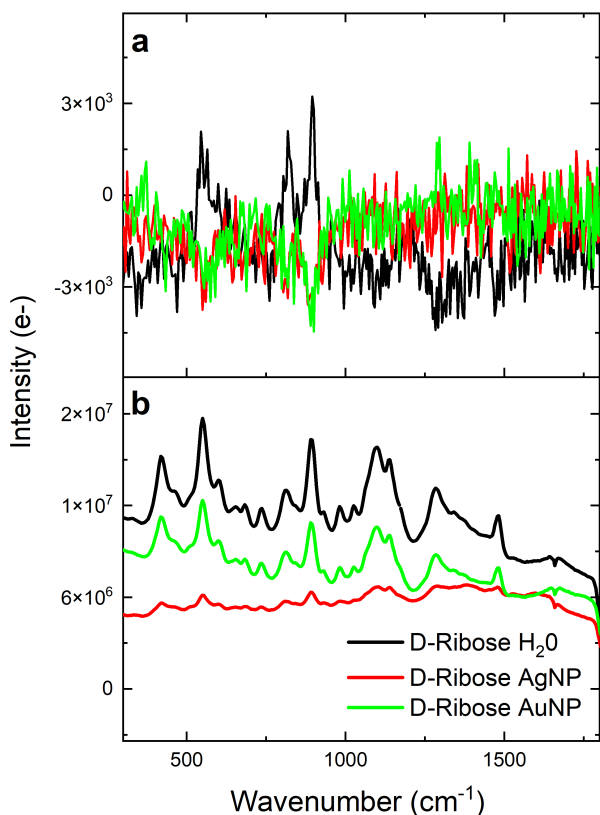

FIGURE 4.2: (a) ROA ($I_R - I_L$) (b) and Raman ($I_R + I_L$) signal of 400 mg/ml ribose in water (black) and with gold and silver nanoparticles prepared as described in the text. Each measurement was taken using 1.5 W of 532 nm excitation over 3 hours, with no virtual-enantiomer correction.

Interestingly though, the ROA spectra in Figure 4.2 (a) also show that the circular signal is flipped in the presence of the nanoparticles, indicating that at least some effect of the nanoparticles occurs in the ROA measurement. This is possible due to the depolarization from the nanoparticles themselves, but needs further investigation.

Because ribose can exist in ring form, which does not have any metal-binding groups, it is possible, even in a highly concentrated nanoparticle dispersion that it would not interact with the nanoparticles. To test if the presence of metal-binding functional groups would increase the nanoparticle-analyte interaction, we measured D- and L- arginine in dispersions of silver nanoparticles. Arginine has several potentially metal-binding functional groups and has been shown to bind to metallic nanoparticles. [57] The results, shown in Figure 4.3, suggest that interaction with the nanoparticles indeed exists, resulting in a circular signal in the arginine-nanoparticle dispersions, but not in the arginine-water solution. Figure 4.3 (b)-(d) also shows however that the circular signal is not constant. For the three solutions prepared and measured, the circular signal differed for each. This was also reflected in the SERS spectra, shown in Figure 4.4, where the signal was enhanced, but the enhancement was different for each prepared solution. The solutions themselves were also unstable with time and after about 12 hours, the nanoparticles would aggregate and settle to the bottom of the vial, with the circular signal going to zero. In-disperison changes and aggregation on the time scale of the measurement are possible explanations for the variable circular signal in different dispersions.
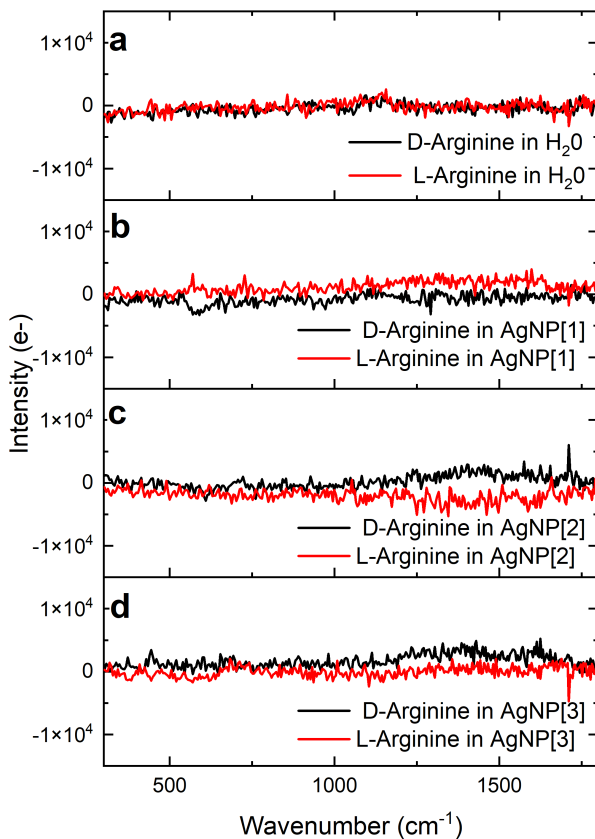
FIGURE 4.3: ROA ($I_R - I_L$) signal of 50 mg/ml arginine in (a) water and (b)-(d) in a solution of silver nanoparticles (AgNP). (b)-(d) represent three repeats of the same experiment. Each measurement was taken using 1.5 W of 532 nm excitation over 3 hours, with no virtual-enantiomer correction.
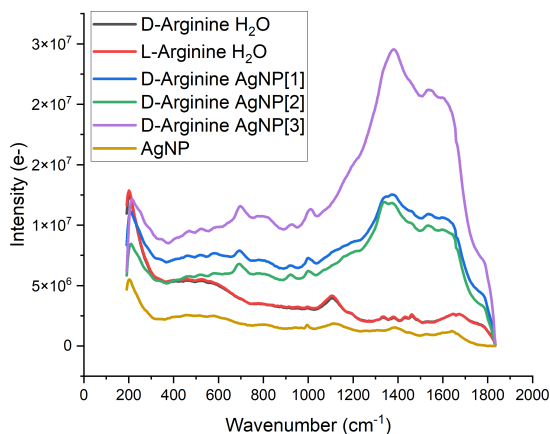
FIGURE 4.4: Raman $(I_R + I_L)$ signal of 50 mg/ml D-arginine in (a) water and (b)-(d) in a solution of silver nanoparticles (AgNP). (b)-(d) represent three repeats of the same experiment. Each measurement was taken using 1.5 W of 532 nm excitation over 3 hours, with no virtual-enantiomer correction.

To further explore this phenomenon, the spectra of D- and L-alanine in the presence of silver nanoparticles were also studied. Alanine, is a much smaller molecule than arginine, but has also been shown to bind with metallic nanoparticles. [57] The results are shown in Figure 4.5. Interestingly, initially the alanine-nanoparticle dispersions showed no circular signal, but when measured three and ten hours after preparation a circular signal started to emerge. This is possibly due to increased aggregation of the nanoparticles or diffusion of the alanine molecules into the hot spots of the existing aggregates, but would need further study. Enantiomers measured at the same time after preparation seemed to have different spectra, but because the signal is so unstable, this is difficult to verify.
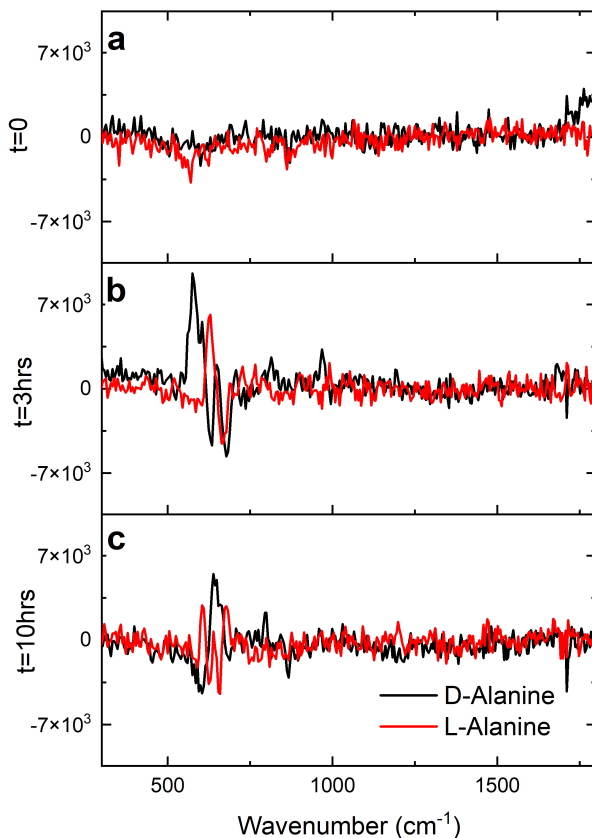
FIGURE 4.5: The ROA ($I_R - I_L$) spectra of 50 mg/ml D- and L-alanine solutions in silver nanoparticle solutions (AgNP) (a) immediately after preparation (b) three hours after preparation (c) and ten hours after preparation. Each measurement was taken using 1.5 W, 532 nm excitation over 3 hours, with no virtual enantiomer correction.

These results show that chiral molecules in dispersion with silver nanoparticles can have increased circular signal ($I_R - I_L$), but they also demonstrate the challenges of this system. The interplay of ligand binding on metallic particles, colloidal stability in the solution and solubility of analytes mean that even if enhancement occurs, it is unlikely to be useful from an interpre-

tation perspective. The goal of SEROA is ultimately to find a mechanism to enhance signal of a large class of molecules, rather than a select few under the correct conditions. To that end, we also investigated the use of hydrogel immobilization as a mechanism to observe SEROA.

4.5.2 *Measurement of Gels*

The use of a hydrogel-nanoparticle system to measure SEROA was demonstrated in 2015 by Pour et al. in a back-scattering ROA configuration. [47] They used a polyacrylic based hydrogel under the trade name Polycarbopol and silver nanoparticles to measure SEROA of D-ribose. We found replicating this system challenging. Thus we began tests using an acrylamide hydrogel with a high water content. [58] Because of the sensitivity of the acrylamide hydrogel to pH, the un-aggregated gold nanoparticles were used instead of the silver-nanoparticle aggregates. The gels were prepared as usual, except the gold-nanoparticle solution was used instead of water in the synthesis. After polymerization, the solutions were then allowed to swell over a period of 48 hours in a supersaturated solution of the analyte. Figure 4.6 shows the results with D-isoascorbic acid.
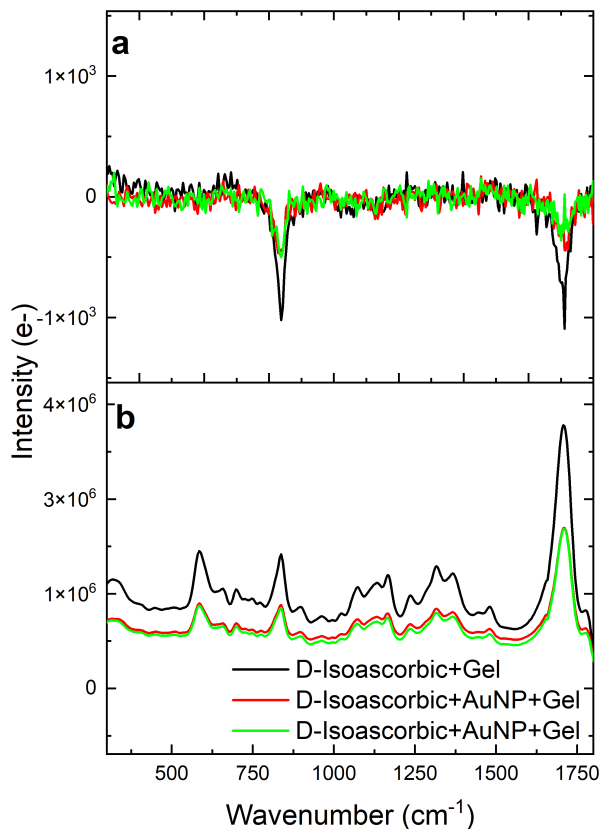
FIGURE 4.6: (a) The ROA ($I_R - I_L$) spectra (b) and the Raman ($I_R + I_L$) spectra of D-isoascorbic acid in an acrylamide based hydrogel without (black) and with (green and red) gold nanoparticles. The green and red spectra are repeated measurements on the same system with 12 hours in between.

Figure 4.6 (a) and (b) show that the gel without the nanparticles had the highest ROA signal, indicating that no enhancement occurred for either the Raman or ROA signal. However, the two repeated measurements with the nanoparticles show that the signal is stable over long periods of time, and the spectra clearly indicate that the D-isoascorbic was incorporated into the gel. By changing the nanoparticle concentration, and type or altering the swelling conditions, we hope that the nanoparticle-analyte interaction can

be enhanced and in time this system can be used to demonstrate a more stable SEROA signal in forward-scattering.

4.6 CONCLUSION

In this chapter, both the potential and the challenges associated with measuring surface enhanced ROA have been introduced. Several first proof-of-concept experiments have shown that measurement of enhanced ROA signal in forward-scattering is possible (Figures 4.3 and 4.5), but that the systems in colloidal dispersions are unstable and vary significantly with time. A first test with an acrylamide hydrogel system demonstrates that this system is much more stable and reproducible, but additional work needs to be performed to increase the nanoparticle-analyte interaction in the hydrogel system.

5

FORWARD-SCATTERED ROA OF BIOLOGICAL MOLECULES

The desire for symmetry, for balance, for rhythm in form as well as in sound, is one of the most inveterate of human instincts.

— Edith Wharton

5.1 ABSTRACT
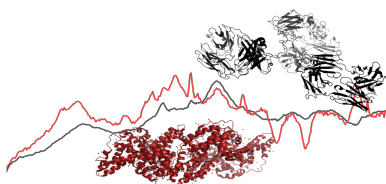
Chirality and the structure of chiral molecules is an integral part of the chemistry of life. Raman optical activity (ROA) is a powerful probe of the chirality of biological molecules, as it can be measured in aqueous solutions, is sensitive to the protein secondary structure and gives a near instantaneous snapshot of the molecule in time. Though ROA of biological molecules has been widely studied, almost all studies have relied on back-scattered ROA instruments. Here, we report the ROA spectra of small biological molecules and proteins measured in forward-scattering. These initial results demonstrate the potential utility of using multiple scattering angles for the measurement of ROA of biological molecules.

From vitamins and amino acids to peptides and proteins, chirality is a key part of the chemistry that makes up life. [6] The chirality and structures of biological molecules is important for understanding phenomena ranging from drug functionality to the origins of life on earth. [13, 59] ROA has several potential advantages in the investigation of biological molecules. First, because water is a weak Raman scatterer, molecules can be studied directly in aqueous systems. This is particularly important when studying large molecules such as proteins or peptides, whose structures can differ significantly based on the solvent in which they are studied. Since water is the "natural" solvent for biological molecules, the ability to study molecules directly in aqueous solutions is a huge advantage. [60] Second, unlike Raman scattering which is dominated by modes associated the side chains of the constitute amino acids, ROA is more sensitive to the backbone vibrations of larger biological molecules such as proteins and peptides, giving insight into secondary structure. [61] Finally, because the time scale of Raman scattering (c.a. 10^{-14}s) is much faster than conformational changes, theoretically time dependent phenomena can be studied. The large caveat being that currently ROA measurements of large biomolecules and proteins take several hours. [61]

Though investigation into biomolecules using ROA has been one of the most active areas of ROA research, reports have exclusively used back-scattering ROA instruments. [61] Since the first reports of forward-scattered ROA by Barron et al., and the construction of a stable forward-scattering based instrument by Haesler et al., virtually no investigation into biological molecules has been made using forward-scattering. [30, 31] This oversight is likely due to the fact that biomolecules are already difficult and time consuming to measure in back-scattering, often taking from 10 to 48 hours, and the signal is expected to be even weaker in forward-scattering. However, because the tensor contributions differ in backward- and forward-scattering, forward-scattered measurements are potentially valuable for understanding the origin of ROA scattering from this class of molecules. Here, we show initial results of ROA of biological molecules measured in forward-scattering. While additional work needs to be done to verify these spectra with computational methods, we hope that reporting these initial results will spur more research into using alternate ROA scattering angles to measure biological

compounds.

5.3 EXPERIMENTAL METHODS

The measurements were performed with the tool described in Chapter 2. Unlike the measurement of neat solutions reported in Chapter 2, ROA of large biomolecules such as proteins and peptides requires careful sample preparation. This includes the use of activated charcoal for purification and filtration to reduce the influence of fluorescent impurities. To further reduce fluorescence, samples are routinely left in the laser beam for several hours before measurement to quench any remaining fluorescence in the sample. [14] Additionally, the measurement times are much longer for ROA of small and large biological molecules, ranging from 3 to 20 hours. Because of this, as discussed below, not all of the measurements were performed with two-phase correction, which in our instrument requires two separate measurements, and is impractical for such long measurement times.

5.4 RESULTS AND DISCUSSION

Here, we report the measurement of ROA from several small biological molecules and proteins in forward-scattering. The reader should note, that especially the protein spectra should be treated as preliminary results only. While the spectra reported here are repeatable, further work needs to be done to compare these spectra with theoretical predictions to verify their origin.

5.4.1 *Small Biological Molecules*

In Figures 5.1-5.3 the spectra of small biological molecules in water are shown. Rather than subtracting the water background, the Raman spectra are shown with axes adjusted. Ribose, ascorbic acid and alanine were chosen because they represent three important classes of small biological molecules (sugars, vitamins and amino acids, respectively), are readily available, and have previously reported ROA spectra. [30, 47]
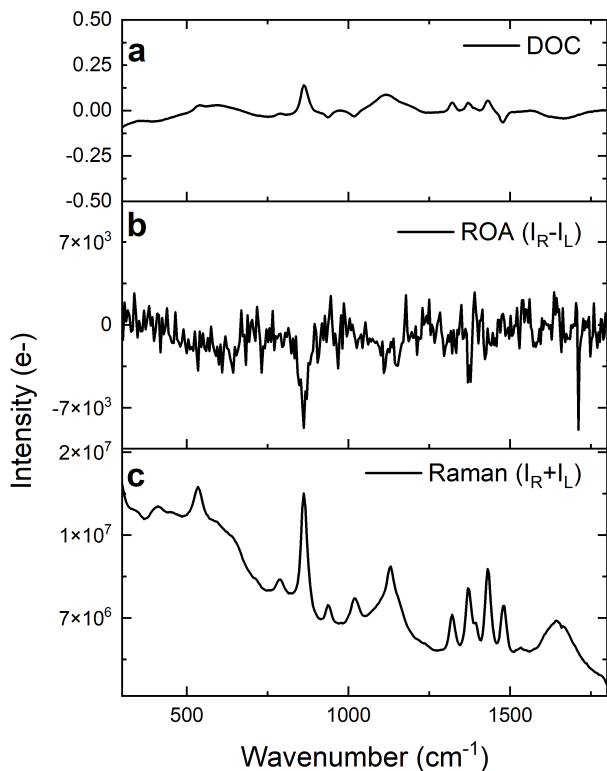
FIGURE 5.1: (a) The degree of circularity (DOC), (b) the ROA spectrum and (c) the Raman spectrum of 50 mg/ml L-alanine in water. All measured with 1.5 W of incident laser power, at 532 nm wavelength. The DOC was measured with incident circularly polarized light for a total of 1 hour; the ROA and Raman spectra were collected over 10 hours.
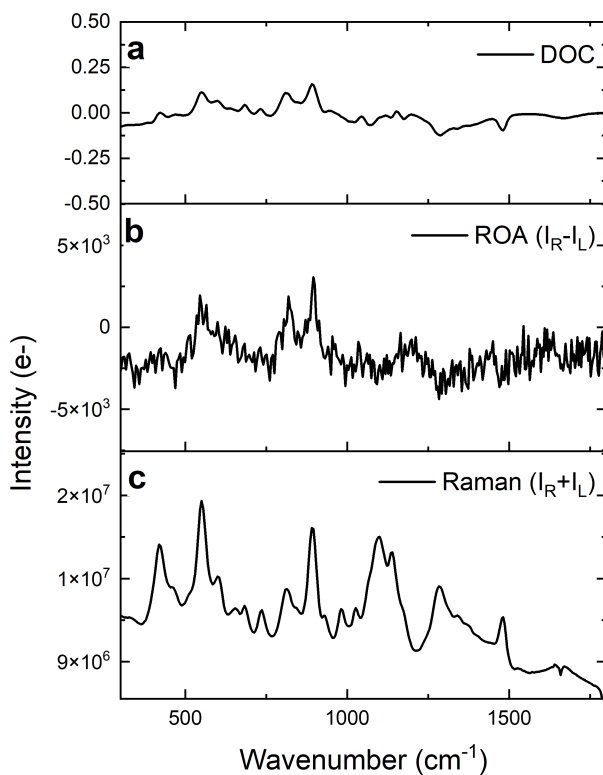
FIGURE 5.2: (a) The degree of circularity (DOC), (b) the ROA spectrum and (c) the Raman spectrum of 400 mg/ml D-ribose in water. All measured with 1.5 W of incident laser power, at 532 nm wavelength. The DOC was measured with incident circularly polarized light for a total of 1 hour; the ROA and Raman spectra were collected over 3 hours.

Because in-solution measurements take significantly more time than measurements of neat solutions, all the measurements here with the exception of L-ascorbic acid are taken without virtual enantiomer correction. The error level in our instrument is sufficiently low that the virtual enantiomer correction, as shown in Figure 5.3 gives spectra consistent with the non-corrected spectrum. While the ROA spectra are much noisier than the spectra of neat solutions shown in Chapter 2, Figure 5.4 shows that the signal exceeds the

expected shot-noise error, calculated as the square-root of the intensity of the Raman signal.
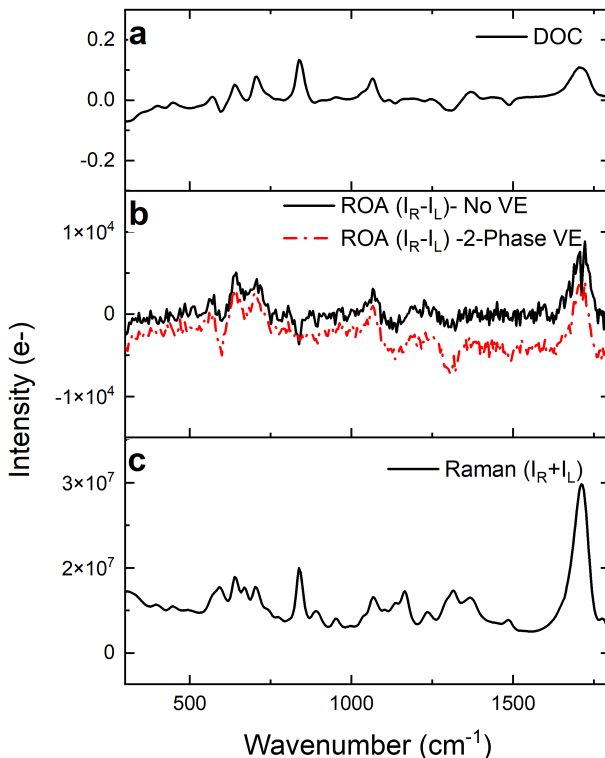

FIGURE 5.3: (a) The degree of circularity (DOC), (b) the ROA spectrum with 2-phase virtual-enantiomer correction (red dotted line) and without virtual enantiomer correction (black) and (c) the Raman spectrum of 400 mg/ml L-ascorbic acid in water. All measured with 1.5 W of incident laser power, at 532 nm wavelength. The DOC was measured with incident circularly polarized light for a total of 1 hour; the ROA and Raman spectra were collected over 3 hours.
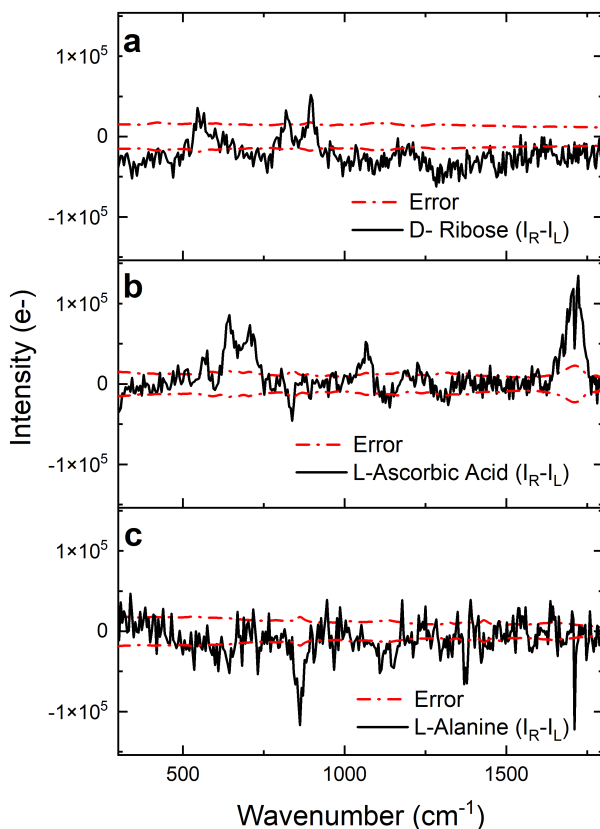
FIGURE 5.4: The ROA spectra of (a) D-ribose, (b) L-ascorbic acid and (c) L-alanine alone with the error estimates for each measurement, calculated as the square-root of the Raman signal. The measurement conditions are the same as described previously.

These measurements confirm that forward-scattering is a useful tool in measuring small biological molecules and lay the ground work for the measurement of proteins, as we show in the next section.

5.4.2   *Proteins*

Proteins are large biological molecules composed of chains of amino acids. They are responsible for many important functions in the body, and malformed proteins are often the cause of serious diseases such as sickle-cell anemia and Parkinson's disease. [62] The different levels of protein structure are described in four categories. The primary structure is the ordering of the constituent amino acids. Secondary structure describes the three-dimensional arrangement of the chain of amino acids. Secondary structures can be classified primarily as either α-helix or β-sheet. α-helicies are right-handed spirals and β-sheets are zig-zagging sheets of amino acid chains. The tertiary structure refers to the arrangement of the groups of α-helicies and β-sheets and quaternary structure is how large subunits form into a multi-unit protein complex. Understanding the structure of proteins and the relationships between the different structural levels and protein function, is an active area of research. [62]

To understand the potential utility of forward-scattering for the measurement of ROA of proteins, we selected three sample proteins for study: hen egg-white lysozyme, bovine serum albumin (BSA) and human immunoglobin G (hIG). The structure of BSA is dominated by α-helices, hIG is β-sheet-dominated and lysozyme is a mixture of the two. Comparing the measured spectra of these three proteins should indicate if the secondary structural changes can be measured with forward-scattered ROA. Lysozyme and hIG were prepared as described in Hecht et al., with the use of activated charcoal and filtration to reduce the presence of impurities. [14] BSA was dissolved in water and measured without further preparation. All of the proteins were left in the laser path for several hours before measuring to quench any fluorescence. The results are shown in Figures 5.5-5.7.
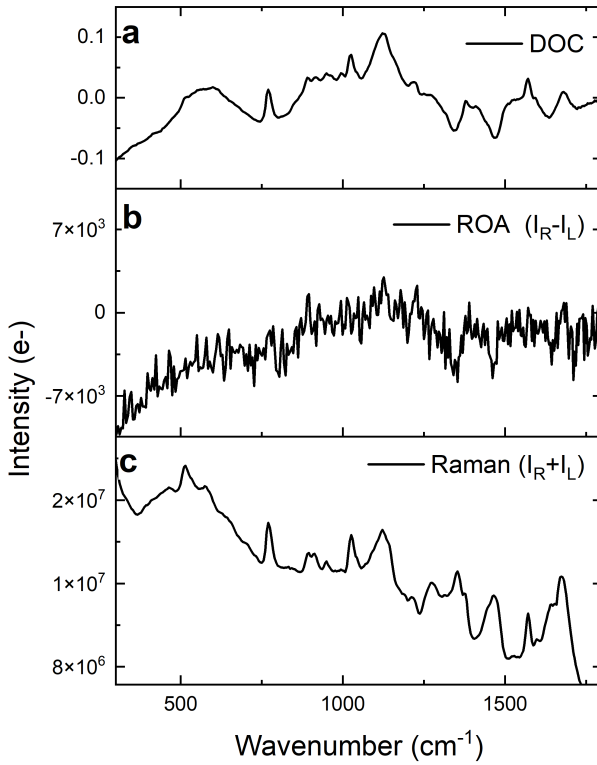
FIGURE 5.5: The (a) DOC, (b) ROA and (c) Raman spectra of hen egg-white lysozyme measured at 70 mg/ml in 100 mM acetate buffer at pH 4.6. Measurement time was 10 hours with 1.5 W incident laser power and 1 hour for the DOC.
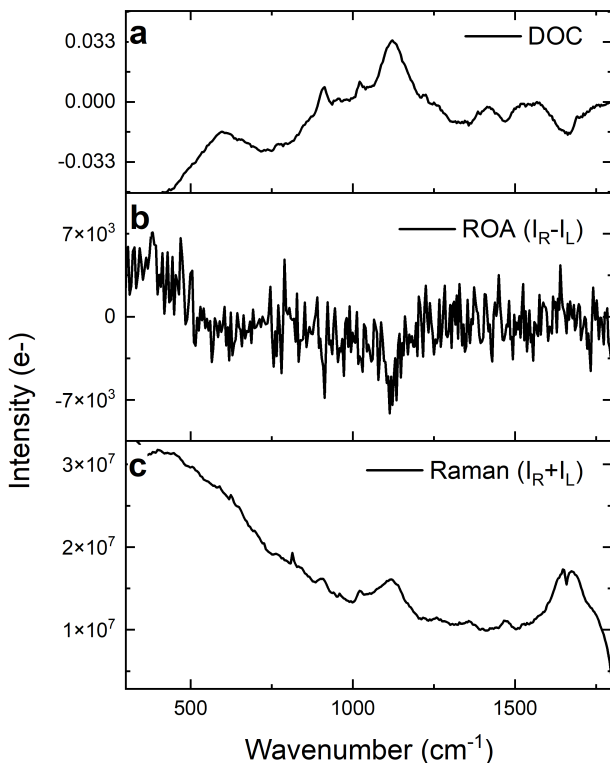
FIGURE 5.6: The (a) DOC, (b) ROA and (c) Raman spectra of human immunoglobin G measured at 12 mg/ml in 100 mM acetate buffer at pH 4.6. Measurement time was 20 hours with 1.5 W incident laser power and 1 hour for the DOC.

Because the measurement times for the proteins varied from 10 to 20 hours, the ROA spectra reported in Figures 5.5 and 5.6 are both without virtual-enantiomer correction. To check if this is a valid approach, BSA was also measured with 2-phase virtual-enantiomer correction. As shown in Figure 5.7(b), in the virtual-enantiomer-corrected spectra, the two peaks at 1360 and 1470 cm^{-1} seem to remain. This reinforces that the peaks are more likely to be related to true ROA signal.
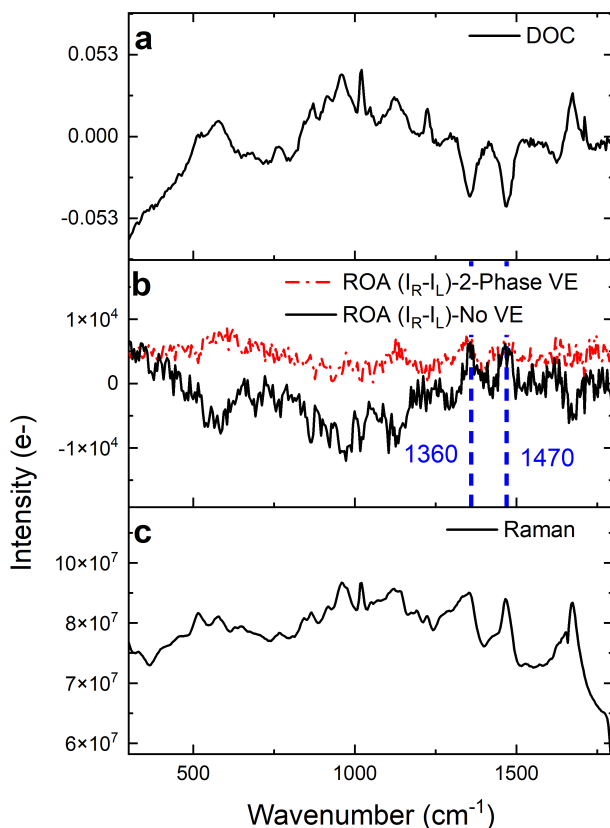
FIGURE 5.7: (a) The degree of circularity (DOC), (b) the ROA spectrum with 2-phase virtual-enantiomer (VE) correction (red dotted line) and without virtual-enantiomer correction (black) and (c) the Raman spectrum of 300 mg/ml bovine serum albumin (BSA) in water. All measured with 1.5 W of incident laser power at 532 nm wavelength. The DOC was measured with incident circularly polarized light for a total of 1 hour; the ROA and Raman spectra were collected over 20 hours.

To further test the reliability of the ROA signal from proteins, lysozyme was measured at two different concentrations (70 mg/ml and 140 mg/ml) and with two measurements at each concentration, as shown in Figure 5.8. While the spectra are still very noisy, the peaks at 1360 and 1470 cm^{-1} are a

consistent feature. This is further supported by plotting the expected error with the ROA signal as shown in Figure 5.9, where again the two peaks are above the expected error (shot noise).
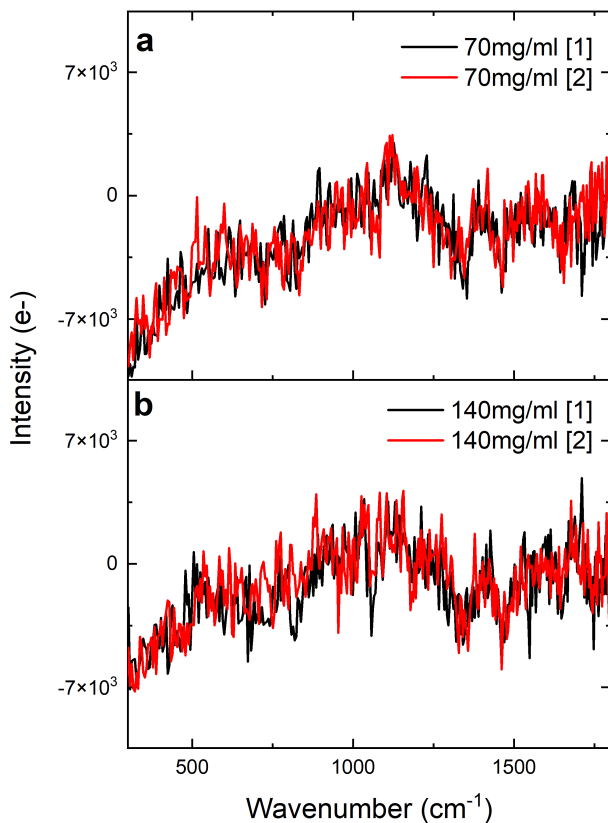

FIGURE 5.8: (a) The ROA spectrum of lysozyme measured at a concentration of 70 mg/ml, with two repeat measurements. (b) The ROA spectrum of lysozyme at 140 mg/ml also with two repeat measurements. Both samples were dissolved in 100 mM acetate buffer at pH 4.6, with 1.5 W of incident laser power at 532 nm and a 10 hour measurement time.
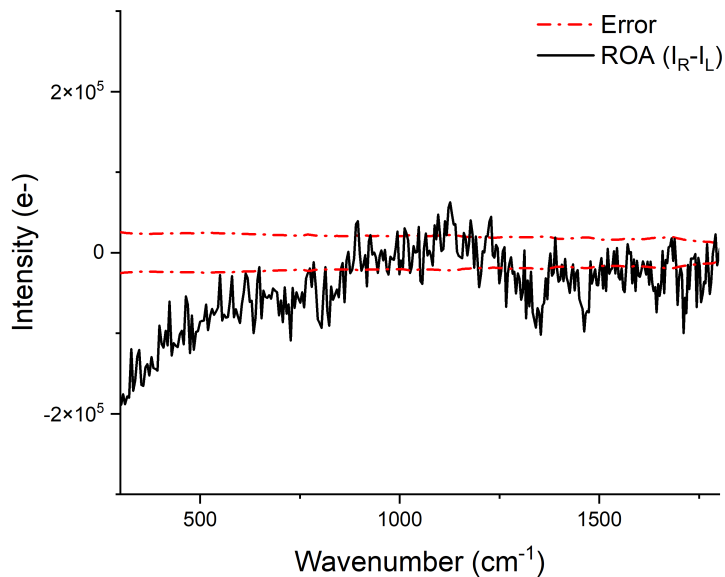
FIGURE 5.9: The ROA spectra of 70 mg/ml lysozyme in water together with the expected error calculated from the square root of the corresponding Raman signal. The sample was measured with the same conditions listed above in Figure 5.8.

Ideally, the measured spectra would now be compared with calculated spectra, but because calculated spectra are not available, we can also use comparative analysis to draw some preliminary conclusions. Figure 5.10 shows the smoothed ROA spectra of the three proteins along side images of the proteins structures. The structural images were rendered using PyMOL and the protein data bank (PDB) data files. [63–65]
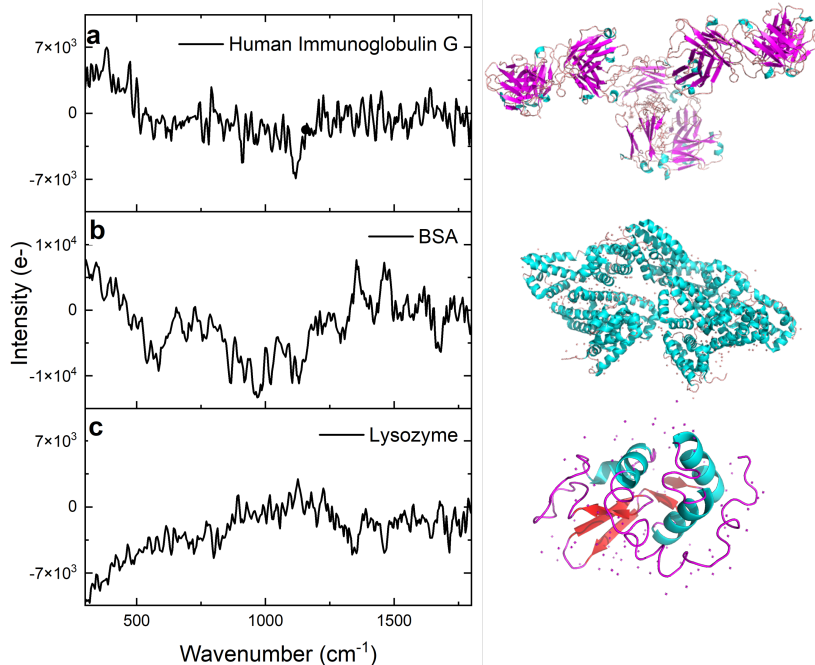
FIGURE 5.10: The ROA spectra for (a) human immunoglobulin G, (b) BSA and (c) hen egg-white lysozyme, measured as described above in Figures 5.5-5.7. The spectra here are smoothed in order to facilitate comparison (raw data included in appendix).

The protein structures are shown in Figure 5.10. BSA is dominated by α-helices (shown in blue) and human immunoglobulin G is dominated by β-sheets (shown in purple), while lysozyme is a mix of the two structures. Tentatively, the ROA structures seem to support this, with the peaks at 1360 and 1470 cm^{-1}, only being present in the BSA and lysoyzme structures where the α-helices dominate. These peaks are notably absent in the ROA spectra of human immunoglobulin G. Interestingly, the sign of the peaks at 1360 and 1470 cm^{-1} are inverted for BSA and lysozyme. Its unclear if this is due to an instrument artifact or the influence of differences in the tertiary structure.

As outlined in Chapter 3, artifacts can be caused by the depolarization terms which can overwhelm the (much smaller) ROA signal. Because the signal here is so low, it is important to try to understand the potential influence of artifacts/depolarization. To understand the depolarization caused by the proteins, the degree-of-circularity was measured as described in Chapters 2 and 3. Briefly, circularly polarized incident light was used rather than depolarized incident light, and the DOC is the circular difference $(I_R - I_L)$ over the total $(I_R + I_L)$. The DOC is a measure of how strongly depolarizing certain modes are, as depolarization can lead to a circular difference signal that is the result of achiral scattering terms.

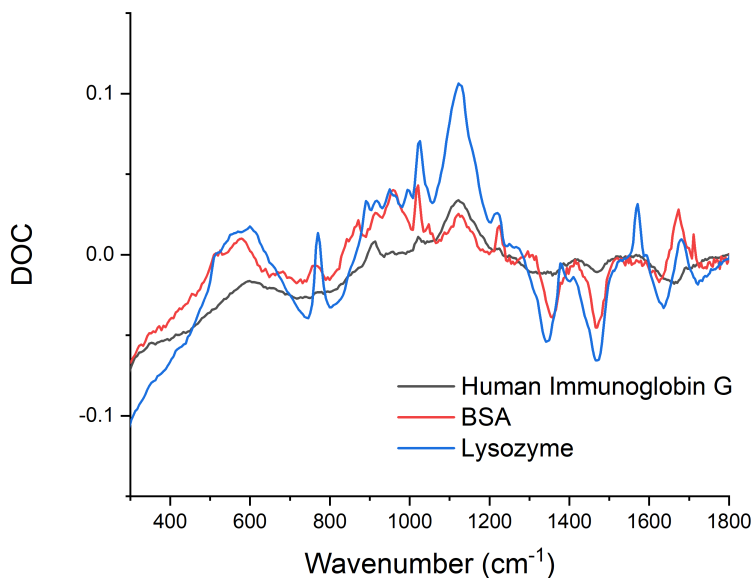

FIGURE 5.11: The DOC spectra of human immunoglobulin G (black), BSA (red) and hen egg-white lysozyme (blue), measured with incident circularly polarized light, with 1.5 W of laser power at 532 nm and purification as described above in Figures 5.5-5.7.

Figure 5.11 shows the resulting DOC measurements for each protein. Here, the y-axis is adjusted to show the features more clearly. Because the

proteins are measured in water, which gives some background signal, and in addition some residual florescence remains, the DOC values are much lower than for neat solutions. Interestingly the DOC results show a similar result as the ROA spectra. The two peaks at c.a. 1360 and 1470 cm^{-1} are present in BSA and lysozyme but not in human immunoglobulin G. This brings into question whether the previous ROA peaks were in fact from ROA scattering, or residual artifacts from the depolarization terms. A final answer to this question would only be possible with further experimentation and comparison with simulated spectra. Perhaps a more interesting question is if it matters. If the DOC spectra can differentiate the secondary structures in the proteins, it is perhaps the better tool to exploit.

5.5   CONCLUSIONS

We have shown the forward-scattered ROA spectra of several small biological molecules and proteins. The utility of forward-scattering for measurement of biomolecules is discussed and a demonstration of the differentiation of protein secondary structure using ROA and/or DOC measurements is given. A great deal of additional work is needed to understand the origin of the signal reported here. Because of the low signal and long measurement times, truly artifact-free measurements are impossible, meaning that future simulations of forward-scattered ROA signal from proteins are key as a comparison. Though the DOC spectra indicated that the origin of the ROA signal may in fact come from achiral depolarization terms, the DOC spectra also show features that are possibly consistent with the protein secondary structures. Simulation of the DOC spectra of proteins would also be needed to further support and understand these results. It is our hope that reporting these initial results will encourage more investigation into the use of forward-scattered ROA of biological molecules.

6

CONCLUSION AND OUTLOOK

Do your work, and then step back.

— Lao Tzu

CONCLUSION

In this thesis, we have discussed the construction and testing of a new ROA instrument, developed a model to understand the contribution of artifacts to ROA, and demonstrated proof-of-concept measurements of SEROA and ROA of proteins. Each of these represents a small, but significant step forward in the advancement of the measurement of ROA. The majority of ROA research today focuses on applications of ROA and while this is, of course, an important aspect of the field, development of the measurement itself should not be discounted. At the time of writing, still only one ROA spectrometer is commercially available, which uses a single laser line and a single scattering angle. The advancements outlined in this thesis lay the groundwork for the development of a new generation of ROA instruments with as much variability and ease-of-use as commercial Raman systems. Only when measurement of ROA at different wavelengths and scattering angles is routine can the true potential of ROA begin to be exploited.

Developing a model to understand artifacts in ROA, and a list of "universal" controls is essential to the expansion of the field. Today, almost all groups performing ROA measurements are related academically to the founders of the field (Laurence Barron, Laurence Nafie and Werner Hug). ROA research is limited to this small number of groups because of the necessary pass-down of information on how to identify and avoid artifacts, as well as the relatively small pool of ROA instruments. While published reports highlighting the issue of artifacts exist, researchers new to the field routinely publish spectra that are likely the result of artifacts. The list of controls outlined in Chapter 3, is useful to groups entering the field as well as reviewers who themselves may be unfamiliar with the details of artifact spectra. The development of a standardized list of controls for ROA instruments levels the playing field for those hoping to work in ROA, and

also helps to reduce the number of published artifact spectra. The Mueller matrix model developed in Chapter 3 is also a user-friendly way to understand how artifacts propagate in optical set-ups, facilitating easier design of new ROA systems.

In Chapters 4 and 5 of this thesis we explored the application of both the newly developed forward-scattered ROA instrument and the artifact model. First, measurements highlighting both the promise and challenge of measuring SEROA in forward-scattering were shown. Perhaps more importantly, the various potential sources of surface-enhancement were discussed. As outlined in the outlook below, once a reliable SEROA system is established, measurement of the DOC will help to improve our understanding of the origin of SEROA signals. The contribution of the various scattering terms in SEROA will likely be very different, and the use of the Mueller matrix model from Chapter 3 will help to elucidate these changes. Much work has to be done to fully understand and utilize surface-enhancement in ROA, but beginning from a clear understanding of artifacts is essential.

In Chapter 5, the measurement of biological molecules in forward-scattering was explored. Again, the developed understanding of artifacts led to important insights. The DOC measurement of various proteins seemed to give information about the protein secondary structure. Though the measurement of biological molecules with ROA has been one of the most active areas of the field, the effects of artifacts and depolarization from proteins has been little explored. Additional experimental and theoretical work could give insight into the potential uses of alternative-angle ROA scattering and the use of DOC as a measurement of protein structure.

This thesis is titled "The Measurement of Raman Optical Activity" because the focus of this work was on improving the measurement itself. A new ROA instrument was developed, as well as a new way of understanding artifacts. The second half of this thesis focused on the applications of the new instrument and applying our understanding of artifacts to surface-enhanced ROA and ROA of biological molecules. As outlined in the next section, further improvements in ROA instrumentation based on the system developed here and utilization of the Mueller-matrix modeling tools, could lead to even more interesting developments. The more advancements we make in the development of ROA measurements, the more ROA's potential can be utilized.

OUTLOOK

6.0.1 *Next Generation of ROA Instruments*

In Chapter 2 we showed the development of the ZROA instrument, the first ROA instrument to utilize high-frequency polarization modulation. This advancement was made possible through use of the Zurich Imaging Polarimeter (ZIMPOL), a CCD-based imaging system originally designed for solar astronomy. The largest advantage of ZIMPOL is the ability to decouple the speed of measurement from the speed of polarization modulation. This ability is enabled by using the CCD rows as charge-storage reservoirs during imaging. Using a higher sensitivity CCD detector would enable even faster and more precise measurement of ROA spectra. In addition, a new sensor architecture could be exploited to reduce the technical complexity of the ZIMPOL camera. Further development of the ZIMPOL system, or systems based on its design, could drastically reduce ROA measurement times and increase measurement precision. The improvement of ZIMPOL would also open up its use in other low-signal and high-frequency modulation applications in spectroscopy.

6.0.2 *Understanding Chirality and the Origin of Life: ROA in Space*

The presence of homochirality (preference for one enantiomer) in biology has led to wide speculation about its origin. [66] One theory is that chiral organic molecules of extraterrestrial origin "seeded" life on Earth, leading to amplification of chirality based on the chirality of this initial "seed" material. [67] Measuring the chirality of organic molecules on the extraterrestrial matter (comets, planets, etc.) would help to test this theory. For this reason, ESA launched a chirality module on the Rossetta spacecraft, consisting of several chromatography columns. But even on Earth, use of chromatography techniques to separate sterioisomers is challenging. An optical instrument would be much easier to incorporate into a spacecraft. A Raman instrument was even included on NASA's Perseverance mission to Mars. An improved and simplified ROA system could potentially be included in future missions to comets or planets to directly study the chirality of organic matter discovered there.

6.0.3 *Beyond Virtual Enantiomers for Artifact Suppression*

In 2002 Werner Hug introduced a scheme to reduce artifacts in ROA by creating "virtual enantiomers" using a system of half-wave plates in his newly designed ROA instrument. [17] This was a huge step towards routine and reliable ROA measurements. In Chapter 3 we introduced an expanded way to understand the origins of artifacts through Mueller matrix modeling. While the model developed in Chapter 3 was purely qualitative, developed for understanding, it is clear that by measuring the totally intensity and the linear depolarization, the circular depolarization term could be calculated. This term could then potentially be scaled and subtracted from non-corrected spectra to obtain artifact-free ROA spectra without the use of virtual enantiomers. This advancement could eliminate the need to multiple moving half-wave plates in ROA instruments, further driving down instrument complexity and thus cost.

6.0.4 *In-Depth Understanding of SEROA*

Several groups have reported measuring SEROA, but significant experimental exploration into the origin of the enhancement is lacking. [43, 44] This is likely because of the challenges associated with ROA measurements in general and SEROA measurements specifically. An in-depth experimental study of SEROA would provide valuable insight into the origin of SEROA signals. Once a reliable SEROA system is established, measurements of the DOC with and without the substrate would allow us to determine if the so-called "SEROA" signal is ROA at all or simply an increased contribution from the depolarization terms.

Once these first experiments were established, a study of the effect of the material (gold, silver, silica, etc.), shape (sphere, rod, star, etc.) and size of the SEROA substrates could be performed. The contributions from the different types of surface-enhancement could qualitatively be understood through careful experimentation. For instance, a substrate could be designed specifically to increase the electric-field gradient and compared against a low electric-field gradient substrate to determine the spectral changes associated with the magnetic-dipole term.

When the origins of SEROA signals are understood, a SEROA substrate could be developed to selectively enhance only the ROA signal. With a

larger dissymmetry ratio, ROA would be as easy to measure as Raman and could be used more widely for diagnostics and drug development.

6.0.5 *SEROA as a Pathway to Understand Complex Fields at Surfaces*

The largest limiting factor in ROA measurements is the weakness of the signal. At first, it seems that SEROA is only a way to solve this, increasing the signal and and allowing lower concentrations to be measured. But, in fact the potential of SEROA is much more. By measuring ROA from multiple scattering angles, the contributions of the different scattering tensors can be isolated. [28] This in turn could be used to measure the selective enhancement of the different scattering terms (α, G and A). In this way SEROA could be used not only as a way to expand the applications of ROA, but also as a measurement in itself.

In a plasmonic analog to the Drexhage experiment, Brechbuhler et al. showed how surface plasmon polaritons (SPPs) emitted from an electric- and magnetic-dipole source were modified by the local environment. [68] In theory ROA could be a similar probe. A measurement of a SEROA substrate from multiple scattering angles would allow for the contributions and enhancement of the electric-dipole, magnetic-dipole and electric-quadrupole terms to be studied. In this way, the things that make SEROA challenging also make it a rich source of information about local electromagnetic fields and density of states.

6.0.6 *ROA and DOC as a probe of Protein Folding and Binding In-Situ*

The study of proteins and biological molecules in solution has been to date one of the most successful applications of ROA. [61] This thesis has shown not only that forward-scattered ROA can also be used for this application, but also that the degree of circularity (DOC) could potentially be a much easier measurement to differentiate between protein secondary structures. Theoretical calculation of the DOC of various secondary structures as well as additional observational experimental studies could verify if the DOC is, in fact, a reliable probe of protein structure. DOC could then be used together with ROA to study structure and binding of proteins in solution.

One of the greatest advantages of Raman-based measurements is that they are particularly suited to measurement in aqueous solution. This is

doubly advantageous for measurements of biological materials. Protein affinity and binding are currently used to test if drug molecules will interact with the designated protein. If ROA or DOC measurements could detect the structural changes in proteins upon binding then they could act as a label free assay to study drug effectiveness. Additionally, because DOC is a much stronger signal than ROA, it could be used in the diagnoses of diseases such as Alzheimer's or Parkinson's, which are caused by protein misfolding. [3] Overall, the potential of ROA, and polarized Raman studies in the understanding of biological materials is just beginning to be exploited. With additional input from simulations and theory and development of instrumentation, applications could expand even further.

A

APPENDIX

A.1   ADDITIONAL DETAILS ON THE ZROA INSTRUMENT

The information in previous publications and theses on ROA instruments was key to the completion of this work. In the spirit of contributing to the next generation of ROA, VOA and chiral investigations, this appendix gives more detailed information about the operation of the ZIMPOL instrument, as well as additional spectra measured on the ZROA tool.

A.1.1   *ZIMPOL Operation*

The basic operational principles of ZIMPOL were described in Chapter 2, here we go into more detail about its operation and calibration procedures.

A.1.1.1   *Description of ZIMPOL Detection System*

The Zurich Imaging Polarimeter (ZIMPOL) allows one to combine high-frequency polarization modulation with a CCD detector. [25] ZIMPOL operates by masking certain rows of the CCD detector and shifting the charges between rows with the polarization modulation frequency. This acts to separate the different polarization states onto different rows of the detector. The basic principle is depicted in the cartoon plot in Figure A.1. The modulation of light of different polarization states by the PEM is shown. In our instrument, the PEM modulation is set to a quarter-wave, and a linear polarizer behind the PEM is set at +45° to the optical axis of the PEM. The quarter-wave modulation means that circularly polarized light (CPL) incident onto the PEM is modulated at the operating frequency (42 kHz). Light linearly polarized along the optical axis of the PEM is not modulated, but light linearly polarized at 45° to the optical axis of the PEM is modulated at twice the operating frequency (shown as the blue and green curves in Figure A.1).

By masking three out of four pixel rows, ZIMPOL effectively creates four images on the CCD which correspond to four time-steps in the PEM modulation. These time-steps (shown in Figure A.1 as p1, p2, p3, and p4) can

then be used to calculate the amount of left- versus right-handed CPL and plus and minus 45° linearly polarized light in the beam incident on the PEM.
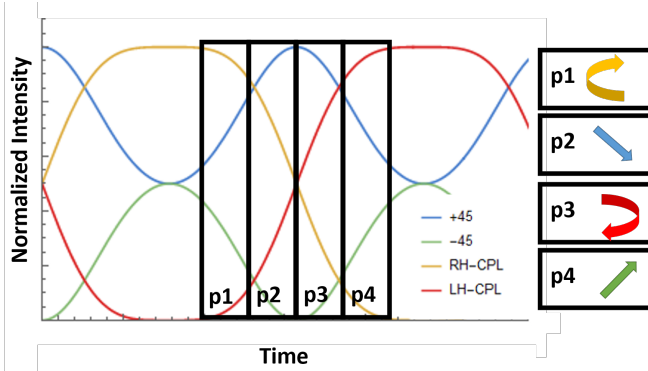

FIGURE A.1: The plot depicts the modulation of different polarization states by the PEM. As time progresses, ZIMPOL allows pixel rows p1, p2, p3, and p4 to detect the various polarization states (right).

In order to convert the raw data into polarization-resolved spectra, a custom python was written during the course of this work for the data processing of the ZROA instrument data. The script first subtracts the dark counts and then separates the full array into four arrays of 140x770 which represent the p1-p4 time steps. The total intensity is calculated by summing up all of the arrays, and the circular and 45° polarized light are calculated as shown in Eqs. A.1-A.3.

$$I = p_1 + p_2 + p_3 + p_4 \tag{A.1}$$

$$I_{CPL} = p_1 + p_2 - p_3 - p_4 \tag{A.2}$$

$$I_{45°} = -p_1 + p_2 + p_3 - p_4 \tag{A.3}$$

After the "polarization arrays" are calculated the phase correction and calibrations steps are performed as described below.

A.1.1.2 *Phase Correction*

In order to correct for any errors in the charge shifting process, each image is collected at two phases (where the "phase" refers to the phase shift in the measurement and modulation frequency). If, as show in Figure A.1, at the first phase the RH-CPL is on the p1 row then in the second phase is set such that LH-CPL is on the p1 row. These two phase measurements are then subtracted from one another to give the corrected values. In order to chose which which two phases the images should be taken at, a phase calibration is performed. During the phase calibration, "pure" circularly polarized light (V1 in Figure A.2) and "pure" 45° are measured and a measurement as made at 1-60 phase shift between the charge shifting frequency on the camera and the frequency of the modulation (PEM). The two phases are then chosen such that the normalized intensities will be positive on one phase and negative at the other.
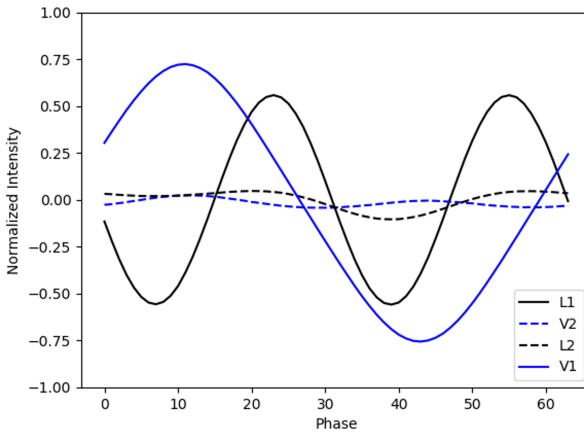

FIGURE A.2: The output of a phase calibration of the ZIMPOL instrument. V1 is the circular signal with incident circularly polarized light. L1 is the 45° signal with incident linearly polarized light. V2 is the circular signal measured with incident 45° polarized light and L2 is the 45° signal with incident circularly polarized light.

An important choice here is if you choose the phases such that you optimize for only the circular signal, or for a combination of both circular

and 45° polarized light. In fact, both of these conditions were tested in the ZROA instrument, it was found that optimizing for measuring for both signals didnt change the sensitivity significantly and so the phases were chosen such that the 45° polarization and the circular polarization were both measured. In order to correct for the different formalized intensities fo the circular and 45° polarized light, an additional polarization calibration is used.

Full Stokes imaging using ZIMPOL would require either the use of a second PEM or the rotation of the existing PEM and two separate measurements. But, as shown in Chapter 3, in solution-based ROA measurements the linear and 45 degree polarization terms in ROA are expected to be equivalent. This means that even with the measurement of three of four total Stokes parameters, this a single measurement with ZIMPOL can give a total picture of the polarization of the scattered light.

A.1.2 *Additional Spectra*

Below are additional spectra from the ZROA instrument, including control measurements of the sample molecule (β-Pinene) measured under different conditions to confirm that the signal was reliable.
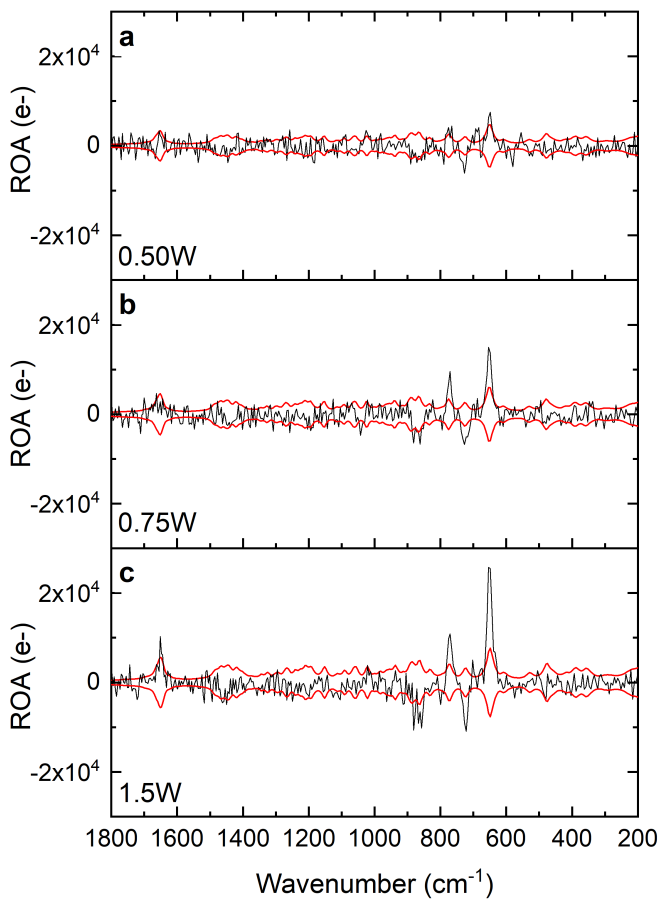
FIGURE A.3: The spectra of (-)-β-pinene at 0.50W (a) ,0.75W(b) and 1.5W (c) in incident laser power. The power reported is that at the laser control.
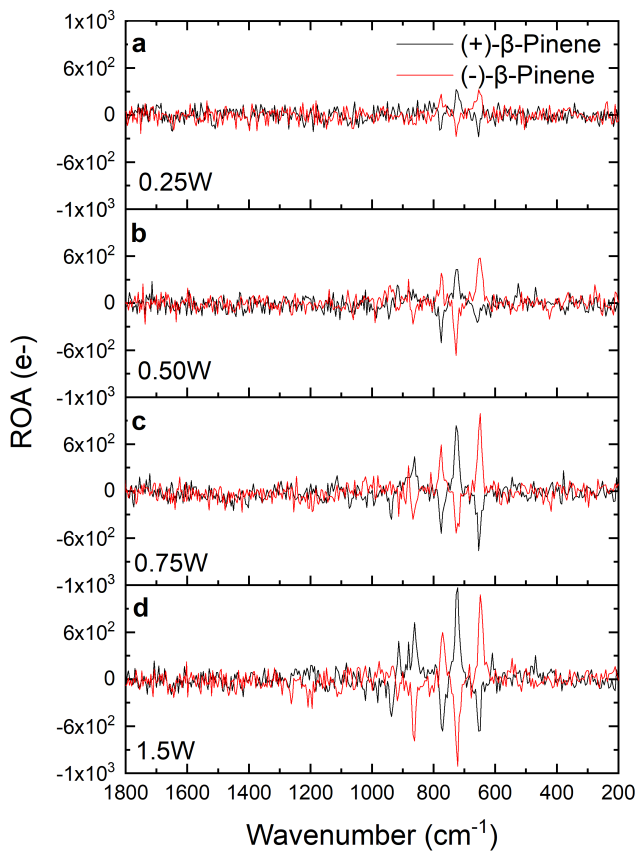
FIGURE A.4: The spectra of (+) and (-) β-pinene measured with various incident laser powers.
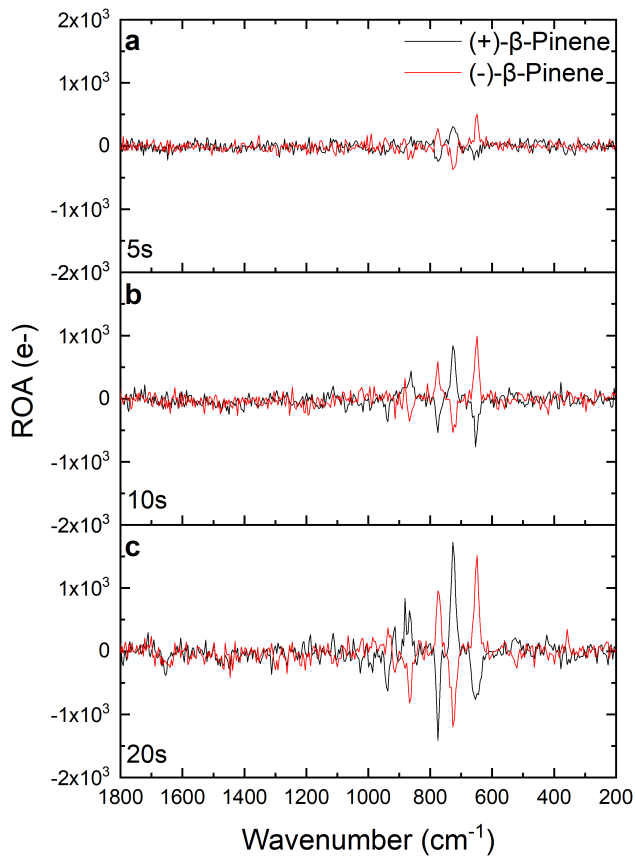
FIGURE A.5: The spectra of (+) and (-) β-pinene measured with 5s(a), 10s (b) and 20s (c) of integration time.
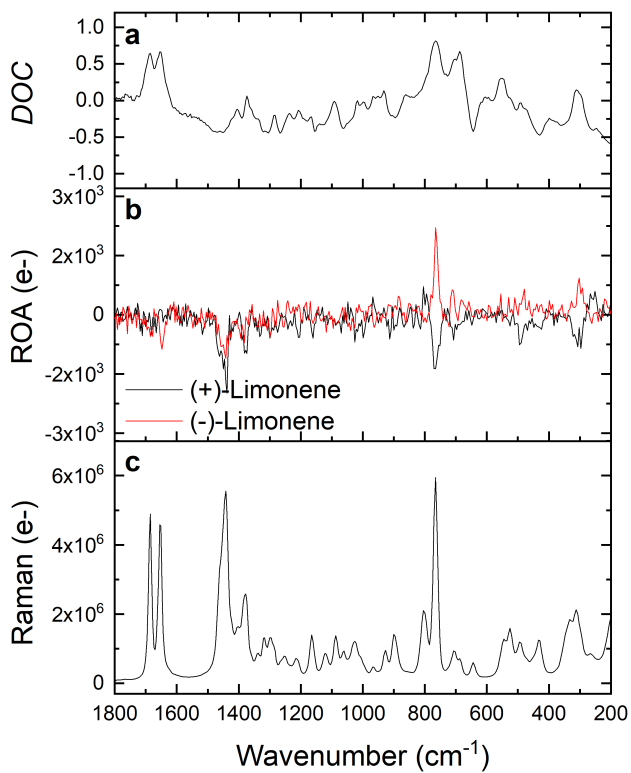
FIGURE A.6: The spectra of (+) and (-) limonene.

.

Component Name	Manufacturer	Part Number
Glan-Taylor laser polarizer	Thor Labs	GL10
Zero-order 532 nm half-wave plate	Thor Labs	WPH10M-532
100 mm focal distance focusing lens	Thor Labs	AC254-100-A-ML
30 mm focal distance collection lens	Thor Labs	AC254-030-A-ML
3 mm right-angle deflection mirror	Thor Labs	MRA03-P01
Photoelastic modulator	Hinds Instruments	II/FS42
Linear polarizer	Thor Labs	LPVISC100-MP2
Dielectric super notch plus Rayleigh filter	Iridian	DSNPF532-25

FIGURE A.7: List of optical parts used in this work with manufacturer and part numbers.

Chemical Name	Manufacturer	CAS Number
Carbon tetrachloride	Sigma Aldrich	56-23-5
Toluene	Sigma Aldrich	108-88-3
(+)-α-Pinene	Sigma Aldrich	7785-70-8
(−)-α-Pinene	Sigma Aldrich	7785-26-4
(+)-β-Pinene	Sigma Aldrich	19902-08-0
(−)-β-Pinene	Sigma Aldrich	18172-67-3
(+)-Limonene	Sigma Aldrich	5989-27-5
(−)-Limonene	Sigma Aldrich	5989-54-8

FIGURE A.8: List of chemicals used with manufacturer and CAS numbers.

A.2   DERIVATION OF ROA MUELLER MATRIX AND ADDITIONAL COM-PARISON SPECTRA

In this appendix, we give more details about so-called "chiral artifacts" including a detailed explanation of the derivation of the Mueller matrix representing

A.2.1   *Derivation of the Mueller Matrices for Raman and ROA*

In order to better understand how the standard Raman scattering tensor can contribute to artifacts in Raman optical activity (ROA) spectroscopy, it is helpful to represent scattering in terms of a Mueller Matrix (MM) and the molecular polarizability tensor invariants. It is worth noting here that similar derivations can, and often have, been done for other types of chiroptical spectroscopies such as CD and VCD and can similarly be very useful in the understanding of those effects. [20]

The most general Mueller Matrix (MM) is shown in A.4 with m00-m33 representing the various elements. [40]

$$MM = \begin{pmatrix} m00 & m01 & m02 & m03 \\ m10 & m11 & m12 & m13 \\ m20 & m21 & m22 & m23 \\ m30 & m31 & m32 & m33 \end{pmatrix} \tag{A.4}$$

As a starting point for understanding Raman and ROA scattering in terms of MM, we use the MMs for forward- and backward-scattering (Eq. A.15 and Eq. A.16) from a single type of asymmetric particle, assuming rotation symmetry, as derived by Savenkov et al. [40]

$$MM_{FS} = \begin{pmatrix} m00 & 0 & 0 & m03 \\ 0 & m11 & -m21 & 0 \\ 0 & m21 & m22 & 0 \\ m30 & 0 & 0 & m33 \end{pmatrix} \tag{A.5}$$

$$MM_{BS} = \begin{pmatrix} m00 & 0 & 0 & m03 \\ 0 & m11 & 0 & 0 \\ 0 & 0 & -m22 & 0 \\ m03 & 0 & 0 & m33 \end{pmatrix} \tag{A.6}$$

Eqs. A.15 and A.16 give a general description of scattering from particles (in our case molecules), but not how that scattering depends on the polarizability of those particles/molecules. In order to include that information we can use the output Stokes vectors for Raman scattering from chiral molecules for forward- and backward scattering as derived by Long in "The Raman Effect". [7]

$$S_{FS}^R = \begin{pmatrix} \frac{\left(45a^2+7\gamma^2\right)+\left(\frac{4}{c}\right)\left(45aG'+\gamma_{G'}^2-\gamma_A^2\right)PS_0\sin[2\chi]}{45} \\ \frac{\left(45a^2+\gamma^2\right)PS_0\cos[2\chi]\cos[2\psi]}{45} \\ \frac{\left(45a^2+\gamma^2\right)PS_0\cos[2\chi]\sin[2\psi]}{45} \\ \frac{\left(45a^2-5\gamma^2\right)PS_0\sin[2\chi]+\left(\frac{4}{c}\right)\left(45aG'+\gamma_{G'}^2-\gamma_A^2\right)}{45} \end{pmatrix} \tag{A.7}$$

$$S_{BS}^R = \begin{pmatrix} \frac{\left(45a^2+7\gamma^2\right)+\left(\frac{8}{c}\right)\left(3\gamma^2+\gamma_A^2\right)PS_0\sin[\chi]}{45} \\ \frac{\left(45a^2+\gamma^2\right)PS_0\cos[2\chi]\cos[2\psi]}{45} \\ \frac{-\left(45a^2+\gamma^2\right)PS_0\cos[2\chi]\mathrm{Sin}[2\psi]}{45} \\ \frac{-\left(45a^2-5\gamma^2\right)PS_0\sin[2\chi]+\left(\frac{8}{c}\right)\left(3\gamma_{G'}^2+\gamma_A^2\right)}{45} \end{pmatrix} \tag{A.8}$$

Eqs. A.7 and A.8 give the expected polarization of light from Raman scattering of chiral molecules in terms of the ellipticity angles ψ, χ of the incident light, the degree of polarization (P) and the tensor invariants: $\gamma, \gamma_A, \gamma_{G'}, aG'$ and a coming from the molecule. A full explanation and derivation of the relevant tensor invariants is beyond the scope of this description, but within the context of this paper it is sufficient to understand that invariants γ and a are related to the electric-dipole–electric-dipole polarizability (α) and will be the only contributions present in achiral molecules. It is important to understand that these terms can lead to a circular component in the scattered light, as seen by their presence in Eqs. A.7 and A.8

in the last term of the stokes vectors, but these contributions are not due to optical activity/chirality, but rather a and γ terms which are present also for achiral molecules. For those more familiar with optics, it can be useful to relate this to the phenomena of anisotropy, where a preferential retardation or absorbance of a given linear state (linear dichroism and linear birefringence) can lead to a circular component in light that is unrelated to the phenomena of optical activity, where optical activity is defined as difference in interaction between left- and right- circularly polarized light.

In chiral molecules the additional terms aG' and $\gamma_{G'}$ are related to the electric-dipole–magnetic-dipole polarizability (G) and γ_A is related to the electric-dipole–electric-quadropole polarizability (A). In both equations the factor S_0 is used to capture the intensity pre-factor and P is the degree of polarization. [7]

In order to define Eqs. A.15 and A.16 in terms of the molecular tensor invariants, we can solve the limiting cases.

First we calculate the expected output from Eqs. A.15 and A.16 with incident unpolarized light.

First for forward scattering:

$$
\begin{pmatrix} m00 \\ 0 \\ 0 \\ m30 \end{pmatrix} = \begin{pmatrix} m00 & 0 & 0 & m03 \\ 0 & m11 & -m21 & 0 \\ 0 & m21 & m22 & 0 \\ m30 & 0 & 0 & m33 \end{pmatrix} \cdot \begin{pmatrix} 1 \\ 0 \\ 0 \\ 0 \end{pmatrix}
\tag{A.9}
$$

Then for backward-scattering:

$$
\begin{pmatrix} m00 \\ 0 \\ 0 \\ m03 \end{pmatrix} = \begin{pmatrix} m00 & 0 & 0 & m03 \\ 0 & m11 & 0 & 0 \\ 0 & 0 & -m22 & 0 \\ m03 & 0 & 0 & m33 \end{pmatrix} \cdot \begin{pmatrix} 1 \\ 0 \\ 0 \\ 0 \end{pmatrix}
\tag{A.10}
$$

Then we can solve Eqs. A.7 and A.8 for the case of unpolarized light when $S_0 = 0$, which leads to, for forward scattering:

$$\begin{pmatrix} m00 \\ 0 \\ 0 \\ m30 \end{pmatrix} = \begin{pmatrix} a^2 + \frac{7\gamma^2}{45} \\ 0 \\ 0 \\ \frac{4(45aG' + \gamma_A^2 + \gamma_{G'})}{45c} \end{pmatrix} \tag{A.11}$$

And for backward scattering:

$$\begin{pmatrix} m00 \\ 0 \\ 0 \\ m03 \end{pmatrix} = \begin{pmatrix} a^2 + \frac{7\gamma^2}{45} \\ 0 \\ 0 \\ \frac{8(\gamma_A^2 + 3\gamma_{G'}^2)}{45c} \end{pmatrix} \tag{A.12}$$

By solving for the limiting case of unpolarized light, we are able to solve for two of the general terms in each of the MM equations. Similarly when we solve for the case of incident circularly polarized light ($S_0 = 1, \chi = \frac{\pi}{4}$ and $\psi = 0$).

For forward-scattering:

$$\begin{pmatrix} m00 + m03 \\ 0 \\ 0 \\ m30 + m33 \end{pmatrix} = \begin{pmatrix} a^2 + \frac{7\gamma^2}{45} + \frac{4(45aG' + \gamma_A^2 + \gamma_{G'}^2)}{45c} \\ 0 \\ 0 \\ a^2 - \frac{\gamma^2}{9} + \frac{4(45aG' + \gamma_A^2 + \gamma_{G'}^2)}{45c} \end{pmatrix} \tag{A.13}$$

So that, for forward scattering: $m03 = \frac{4(45aG' - \gamma_A^2 + \gamma_{G'}^2)}{45c}$ and $m33 = a^2 - \frac{\gamma^2}{9}$.

When we follow the same procedure for backward-scattering:

$$\begin{pmatrix} m00 + m03 \\ 0 \\ 0 \\ m30 + m33 \end{pmatrix} = \begin{pmatrix} a^2 + \frac{7\gamma^2}{45} + \frac{8(\gamma_A^2 + 3\gamma_{G'}^2)}{45c} \\ 0 \\ 0 \\ -a^2 + \frac{\gamma^2}{9} + \frac{8(\gamma_A^2 + 3\gamma_{G'}^2)}{45c} \end{pmatrix} \tag{A.14}$$

From which we can show that for backwards-scattering, $m33 = -a^2 + \frac{\gamma^2}{9}$.

Finally we can again solve for both forward and backward scattering for linearly polarized light, and 45 degree polarized light, such that we get MM^R_{FS} and MM^R_{BS} as shown below.

$$MM^R_{FS} = \begin{pmatrix} q & 0 & 0 & fw \\ 0 & e & 0 & 0 \\ 0 & 0 & e & 0 \\ fw & 0 & 0 & r \end{pmatrix} \tag{A.15}$$

$$MM^R_{BS} = \begin{pmatrix} q & 0 & 0 & bw \\ 0 & e & 0 & 0 \\ 0 & 0 & -e & 0 \\ bw & 0 & 0 & -r \end{pmatrix} \tag{A.16}$$

Where the variables q,e,r,fw and bw are defined as follows:

$q = a^2 + \frac{7\gamma^2}{45}$, $fw = \frac{4(45aG' - \gamma_A^2 + \gamma_{G'}^2)}{45c}$, $bw = \frac{8(\gamma_A^2 + 3\gamma_{G'}^2)}{45c}$ and $e = \frac{45a^2 + \gamma^2}{45}$, $r = a^2 - \frac{\gamma^2}{9}$

A.2.2 *Explaining Virtual Enantiomers using the Mueller Matrices*

The virtual enantiomer scheme introduced by Werner Hug allows the routine measurement of ROA through the correction of small offsets by subtracting optically created ("virtual") enantiomers from each other. [17] The core of Hug's technique is the use of half-wave plates, which reverse the sense of circular polarization. Below is a brief summary of the virtual enantiomer correction scheme including the MM for forward scattering ROA.

A.2.3 *S2.1: Virtual Enantiomers with Perfect HWPs*

The principle of virtual enantiomers is that by inserting a half-wave plate you reverse the sense of circular polarization, thus creating an optical (ie.

"virtual") enantiomer. This can be done using four measurements (4-phase) or two measurements (2-phase). The reader is encouraged to consult Hug's paper for more details, here we will only briefly describe the 2-phase correction schemes using the MMs for ROA scattering in the forward direction.

The Mueller matrix for an ideal half-wave plate is given in Eq. A.17 below. [10]

$$MM_{HWP}^{ideal} = \begin{pmatrix} 1 & 0 & 0 & 0 \\ 0 & 1 & 0 & 0 \\ 0 & 0 & -1 & 0 \\ 0 & 0 & 0 & -1 \end{pmatrix} \tag{A.17}$$

For a 2-phase correction scheme, two measurements are taken, one with HWPs before and after the sample, and one with no HWPs. Using the general stokes vector $S = I, Q, U, V$ to represent the incident light, the two measurements S[00] and S[11] are shown below.

$$S[00] = \begin{pmatrix} Iq + V(fw) \\ eQ \\ eU \\ I(fw) + rV \end{pmatrix} = \begin{pmatrix} q & 0 & 0 & fw \\ 0 & e & 0 & 0 \\ 0 & 0 & e & 0 \\ fw & 0 & 0 & r \end{pmatrix} \cdot \begin{pmatrix} I \\ Q \\ U \\ V \end{pmatrix} \tag{A.18}$$

$$S[11] = \begin{pmatrix} Iq - V(fw) \\ eQ \\ eU \\ -I(fw) + rV \end{pmatrix} = \begin{pmatrix} 1 & 0 & 0 & 0 \\ 0 & 1 & 0 & 0 \\ 0 & 0 & -1 & 0 \\ 0 & 0 & 0 & -1 \end{pmatrix} \begin{pmatrix} q & 0 & 0 & fw \\ 0 & e & 0 & 0 \\ 0 & 0 & e & 0 \\ fw & 0 & 0 & r \end{pmatrix} \cdot \begin{pmatrix} 1 & 0 & 0 & 0 \\ 0 & 1 & 0 & 0 \\ 0 & 0 & -1 & 0 \\ 0 & 0 & 0 & -1 \end{pmatrix} \begin{pmatrix} I \\ Q \\ U \\ V \end{pmatrix} \tag{A.19}$$

Then, to solve for the total intensity and circular component in the scattering light:

$$S_3^{out} = .5(S[00]_3 - S[11]_3) = .5(Iq + V(fw) - (-I(fw) + rV)) = I * fw \tag{A.20}$$

$$S_0^{out} = .5(S[00]_0 + S[11]_0) = .5(Iq + V(fw) + (Iq - V(fw))) = I * q \tag{A.21}$$

Eqs. A.20 and A.21, show that with the virtual enantiomer scheme, any contribution from a circular component in the incident light (V) cancels out, and the only contribution to the circular component in the scattered light is fw, the ROA scattering term and I, the total incident intensity. In the main text of the paper, this is confirmed by looking at ROA spectra with and without VE correction. But we also show, that for light with an incident polarization component above a certain level, the VE scheme no longer corrects for the artifacts. This is because real half wave plates have errors in retardation , which is explained in detail in the next section.

A.2.4 *Virtual Enantiomers with Realistic HWPs*

The general Mueller matrix for a waveplate is given in Eq. A.22, where ϕ is π for a perfect half-wave plate and $\frac{\pi}{2}$ for a perfect-quarter wave retarder. [10]

$$
MM_{WP}^{general} = \begin{pmatrix} 1 & 0 & 0 & 0 \\ 0 & 1 & 0 & 0 \\ 0 & 0 & cos(\phi) & -sin(\phi) \\ 0 & 0 & sin(\phi) & cos(\phi) \end{pmatrix}
\tag{A.22}
$$

For a standard, zero-order quartz half waveplate from Thorlabs, a typical upper bound of the retardance error is from $.993\pi$ to 1.007π. Correcting for errors introduced from the half-wave plates themselves is one of the reasons that 4-phase correction is most often used instead of two phase. [17] By using a lower bound for the retardance error and setting $\phi = .993\pi$, Eq. A.23 can be used instead of Eq. A.17.

$$
MM_{HWP}^{real} = \begin{pmatrix} 1 & 0 & 0 & 0 \\ 0 & 1 & 0 & 0 \\ 0 & 0 & -0.999684 & -0.0251301 \\ 0 & 0 & 0.0251301 & -0.999684 \end{pmatrix}
\tag{A.23}
$$

Using this Mueller matrix for the half-wave plates as outlined above for the two-phase virtual enantiomer scheme, the following equation for the circular component in the scattered light, with incident elliptically polarized light characterized by ellipticity angles χ and ϕ.

$$S_3^{out} \propto -fw + (-0.001e + r)P\sin(2\chi) - 0.03(e + r)P\cos(2\chi)\sin(2\psi)$$
$$(\text{A.24})$$

As discussed in the main text, this shows that for very large circular components in the incident light, the virtual enantiomer scheme is no longer sufficient to correct for the offsets.

A.3   ADDITIONAL EXAMPLES OF ARTIFACT SPECTRA

In order to further aid in the understanding of instrumental artifacts, and to act as a resource we have included several additional spectra here of artifacts. All of the measurements are taken on the Z-ROA instrument in forward scattering.

In Figure A.9 four measurements are shown, with different types of artifacts, and no virtual-enantiomer correction.
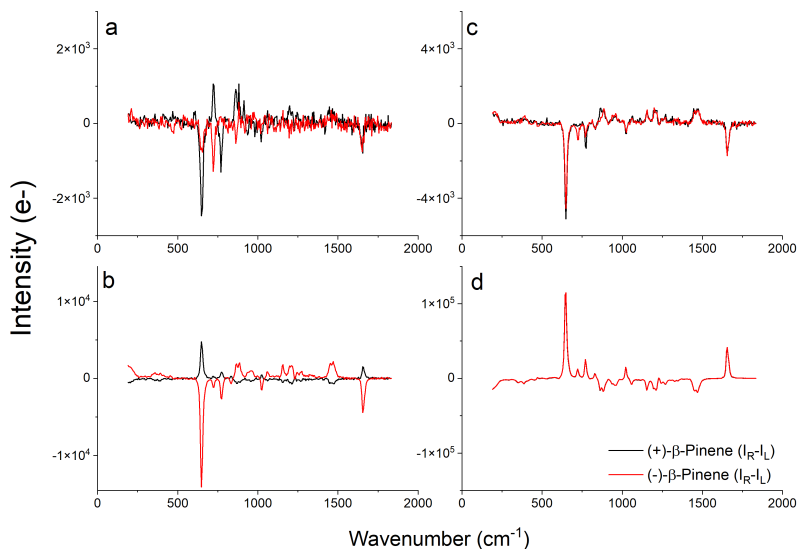
FIGURE A.9: Here four measurements of the enantiomers of β-pinene are shown, with no virtual enantiomer correction. In (a) the artifact level is very low, and the only artifact is the one caused by the strongly polarized mode around 640 cm^{-1}, otherwise the bands of the two enantiomers are flipped. In (b) a static source of birefringence (a quarter-wave plate) is interacting with a time varying degree of incident linear polarization, this creates "mirror" spectra that are not the result of ROA(fw) but rather the circular depolarization (r) term. In (c) the incident light a small static source of circular polarization, but the degree of polarization is small enough that there are still difference between the spectra of the enantiomers. (d) Shows spectra with incident fully circularly polarized light, the spectra of the two enantiomers is identical. The measurement time is approximately 3 minutes, with 1.5 W of incident 532 nm laser power.

Figure A.10 the same four measurements are shown, but with 2-phase virtual enantiomer correction. Both (a) and (c) are correctable artifacts, and the VE corrected spectra are consistent with theory and results from other instruments. Figure A.10(b) and (d) show that they are non-VE correctable artifacts, even though (b) is mirror image spectra of the enantiomers the flipping and the intensities of the peaks are consistent with the circular depolarization term(r) rather than the ROA scattering term(fw).
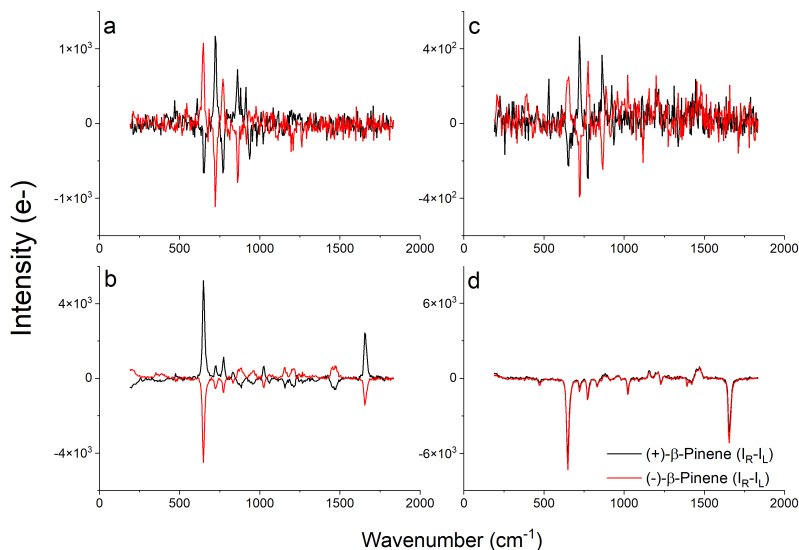
FIGURE A.10: Here four measurements of the enantiomers of β-pinene are shown, this time with 2-phase virtual enantiomer correction. In(a) and (c) the artifacts are correctable, and the corrected spectra show the expected relative peak flipping and intensities. In (b) and (d) the artifacts were not corrected by virtual enantiomers. Though the spectra in (b) are flipped from one another- the intensities of the peaks and the flipping pattern do not match with other reports, or theoretically predicted spectra. The measurement time is approximately 6 minutes, with 1.5 W of incident 532 nm laser power.

In Figure A.10 (b) illustrates the importance of instrumental controls, as this type of artifact is easily mistaken for true signal. Though a time varying incident polarization, combined with birefringence may seem an unlikely scenario this exact artifact was encountered often in the construction of the Z-ROA instrument. Figure A.9 (c) and Figure A.10 (c) also illustrate an important point, that a slightly larger amount of constant circular polarization is still correctable using the VE scheme.

A.3.1   *Instrumental Comparisons*

A key component to understanding artifacts, and differentiating them from so-called "true" signal, is the ability to compare measurements across

instruments. For the convenience of the reader, we have consolidated data from several instruments here using standardly available chiral and achiral molecules. The experimental conditions and optical configurations are given here in detail in the hopes of facilitating easier control measurements for new instruments/techniques in the future.

A.3.2   *Participating Instruments*

In total, we had participation from three research groups, four instruments and six instrument configurations. A summary of instrument comparisons and the naming scheme used is given in Table A.1.

No.	Instrument Name	University	Configuration	Scattering Angle	Spectrometer	Laser
1	G-ROA-FW	University of Geneva	SCP	$0°$	Andor Holospec	Cheetah-X 532nm Picosecond
2	Z-ROA	ETH Zürich	SCP	$0°$	Andor Holospec	Coherent Verdi 2W 532nm CW
3	G-ROA-BW	University of Geneva	SCP	$180°$	Andor Holospec	Cheetah-X 532nm Picosecond
4	A-BT-ChiralRaman2x	University of Antwerp	SCP	$180°$	--	Laser Quantum Opus 532nm
5	A-ROA-Holo	University of Antwerp	SCP	$180°$	Andor Holospec	
6	A-ROA-Kym	University of Antwerp	SCP	$180°$	Andor Kymera 32Bi	

TABLE A.1: An overview of participating instruments and instrument configurations.

Additionally, below is a summary of the measurement conditions for each instrument.

A.3.2.1   *G-ROA-FW and G-ROA-BW*

The details of the G-ROA instrument are given in detail in the thesis of Haesler. [30] The same instrument is able to measure both in backward (G-ROA-BW) and forward (G-ROA-FW) scattering configurations.The measurements are made with neat liquids, as purchased, in a Hellma microcell made of quartz with a 5mm path length. The laser intensity was monitored continuously through a power meter placed after the sample. The CCD cameras (one camera for each measurement configuration) were calibrated using Hg(6035) and Ne(6032) calibration lamps. The Raman and ROA

spectra were Jacobian corrected and the resolution of the cameras was c.a. $13cm^{-1}$. All measurements are 4-phase corrected unless otherwise noted.

A.3.2.2 *Z-ROA*

The Z-ROA instrument is a forward-scattering instrument using a high-frequency polarization modulation scheme, as detailed in Lightner et al. [18]. The samples are also neat liquids, measured as purchased in standard glass vials with a c.a. 10mm path length. The camera is also calibrated using a Hg calibration lamp, as well as reference Raman spectra of pinene. The spectra are Jacobian corrected. The reported power is the given output at the laser, confirmed with a power meter at the laser output. All measurements are 2-phase unless otherwise noted.

A.3.2.3 *A-ROA-Holo and A-ROA-Kym*

The Antwerp home-built ROA is a backscattering instrument with two spectrometer configurations possible , the Andor Holospec and the Kymera 328i. All measurements were made with 4-phase correction.

A.3.2.4 *A-BT-ChiralRaman2x*

The ChiralRaman2x is the only commercially available ROA instrument at the time of writing , it is market by BioTools and operates in backscattering. All measurements are made in 4-phase.

A.3.3 *Comparison Data*

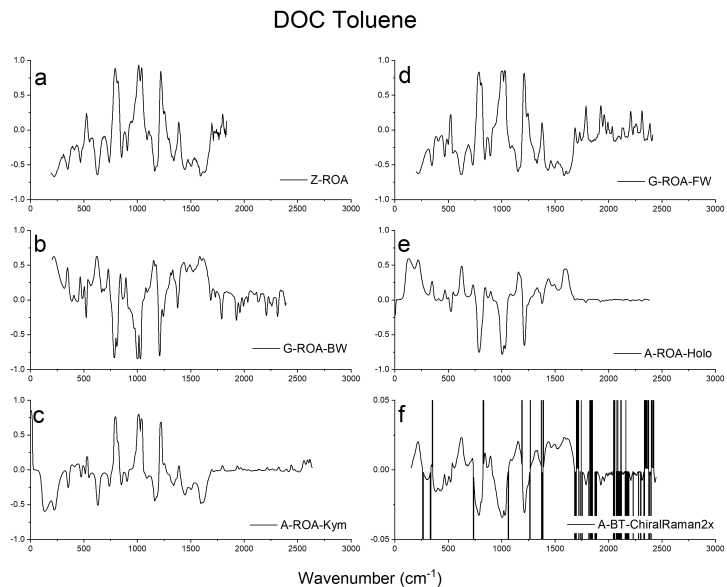Below we give the spectra of several chiral and achiral molecules.

FIGURE A.11: Here the degree of circularity (DOC), which is measured with incident circular polarization is given for toluene measured with on all participating instruments. The ChiralRaman spectra has much lower DOC values because a scaling factor is used which is not accessible to the user, the raw spectra is shown here.
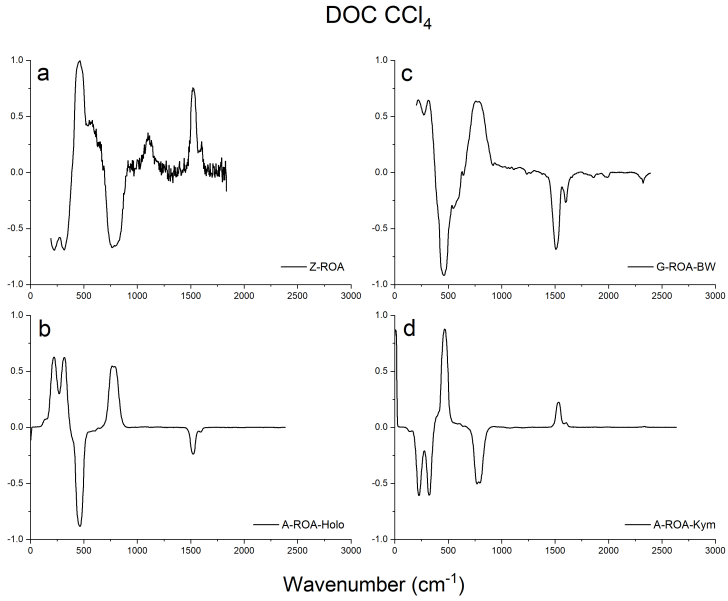
FIGURE A.12: Here the degree of circularity (DOC), with incident circularly polarized light, is shown for CCl_4 for select instruments.
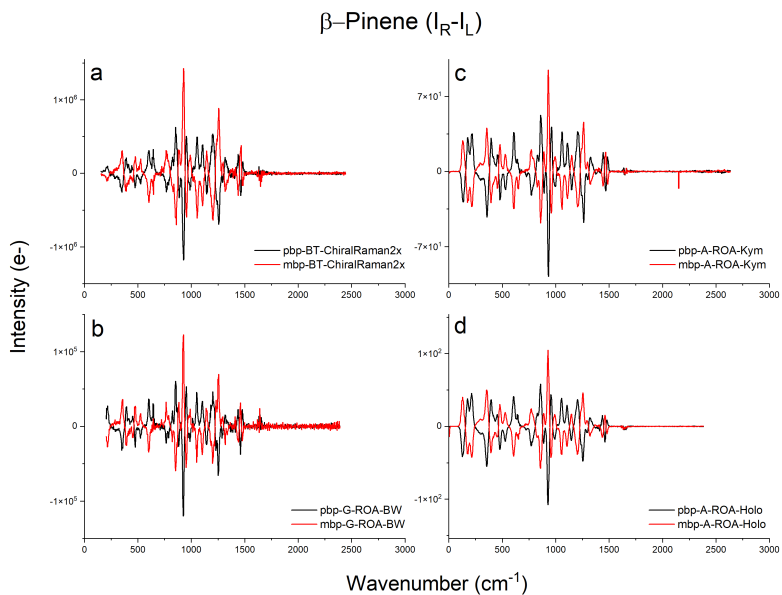
FIGURE A.13: Here the ROA spectrum of β-pinene is shown for all participating back-scattering instruments.
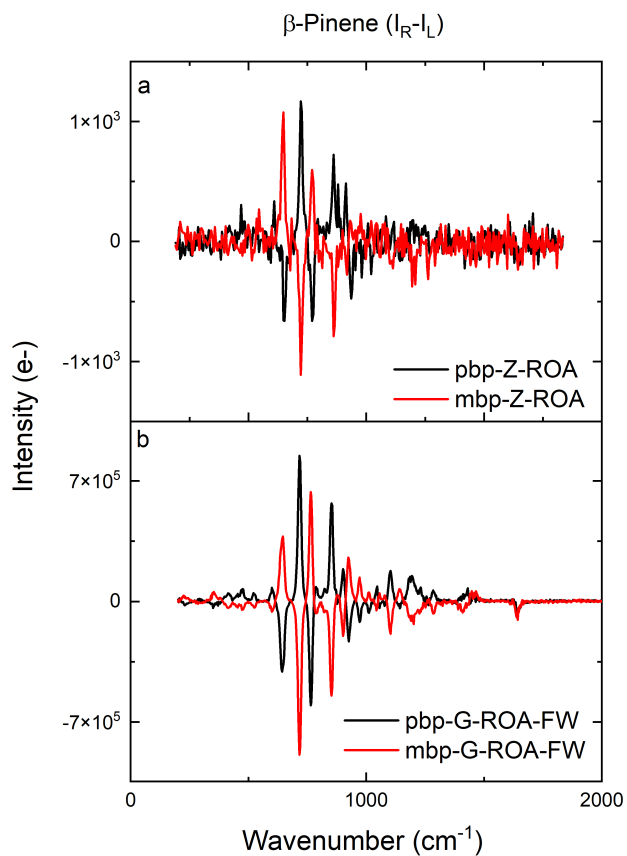
FIGURE A.14: Here the ROA spectra of β-Pinene for the participating forward-scattering instruments.
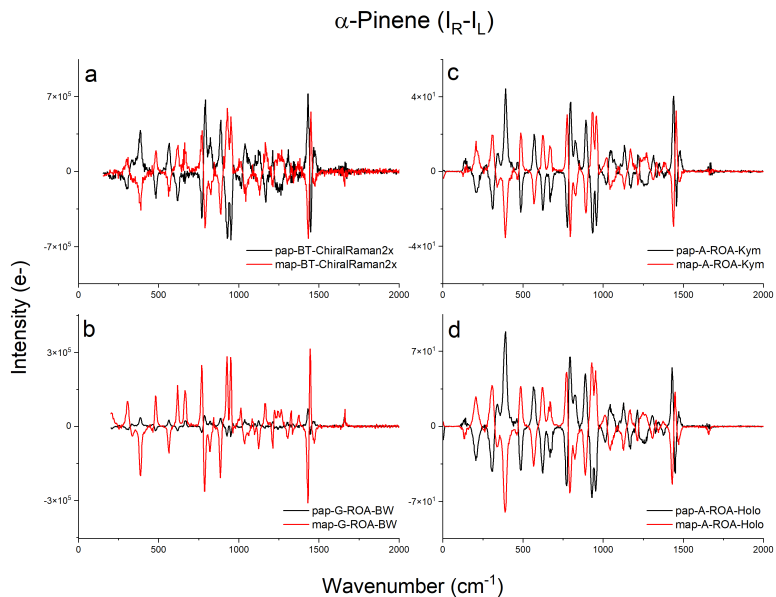
FIGURE A.15: Here the ROA spectrum of *α*-pinene is shown for all participating back-scattering instruments. The G-ROA measurements are shown here without scaling for the difference of total Raman intensity, which is why the (+)*α*-Pinene spectra as a lower signal.
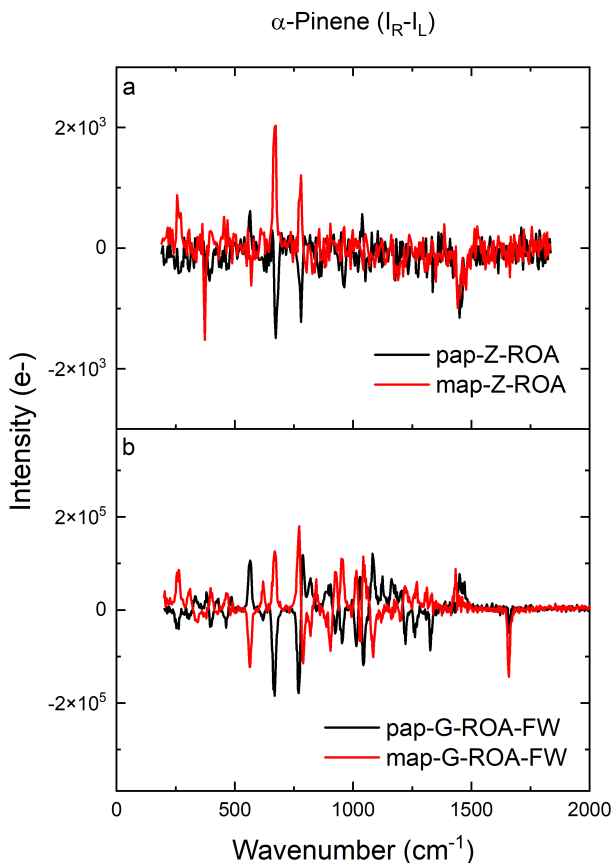
FIGURE A.16: Here the ROA spectra of α-Pinene for the participating forward-scattering instruments.The spectral difference between the two instruments is possibly due to difference in collection efficiencies, but warrants further investigation.

Figure A.17 shows the ROA spectra of phenylethanol collected for all of the back-scattering instruments, readers should be cautious when using phenylethanol as a reference as it can often contain an impurity that interferes with the spectra.
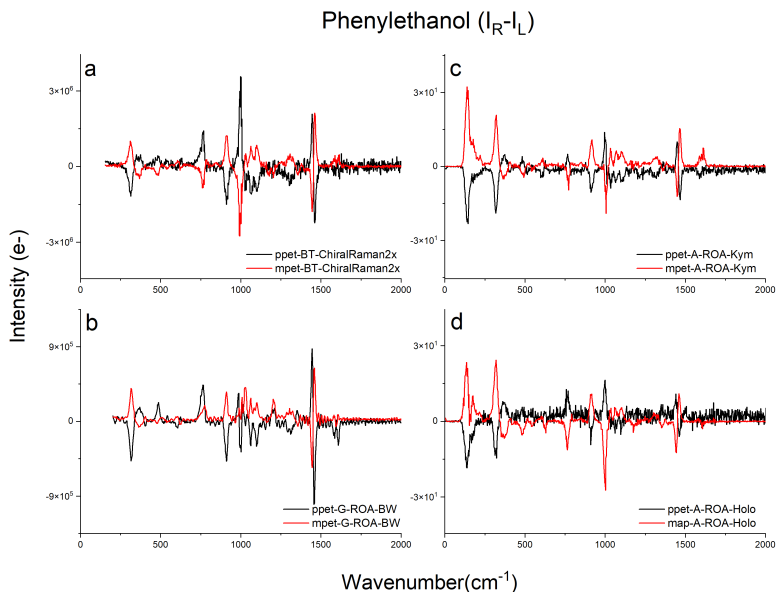
FIGURE A.17: Here the ROA spectra of phenylethanol (pet) is shown for all of the participating back-scattering instruments.

The virtual enantiomer scheme is not only useful to eliminate artifacts but also to understand where artifacts originate in the optical path across different instruments. Figures A.18- A.22 show the separated virtual enantiomer spectra each of the participating instruments for β-pinene. the exception is the ChiralROA2x which does nto have the functionality to report the virtual enantiomers separately.

FIGURE A.18: Here spectra of each of four possible virtual enantiomers is shown for β-pinene measured with the Z-ROA instrument. The top panel shows the two phase corrected spectra and the bottom panel shows the DOC for β-pinene.

FIGURE A.19: Here spectra of each of four possible virtual enantiomers is shown for *β*-pinene measured with the G-ROA-FW instrument. The top panel shows the four-phase corrected spectra and the bottom panel shows the DOC for *β*-pinene.
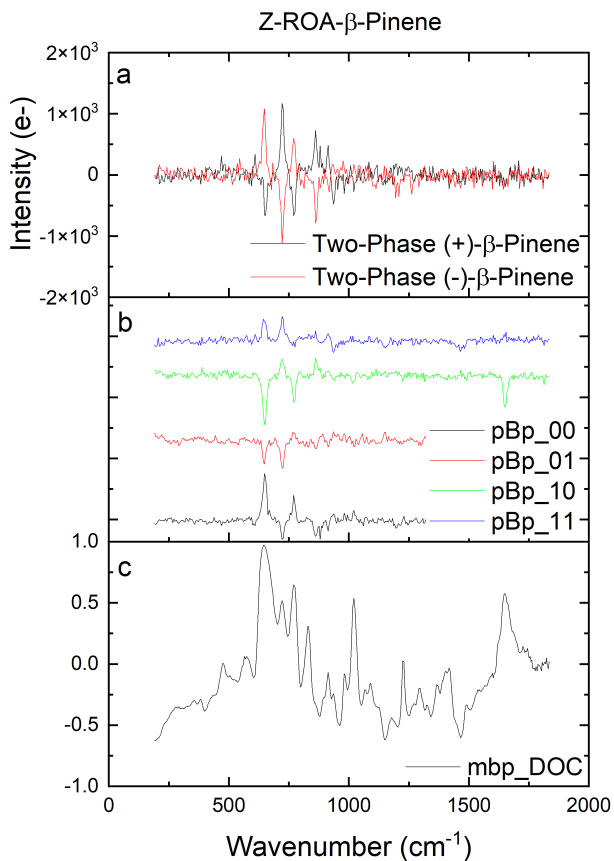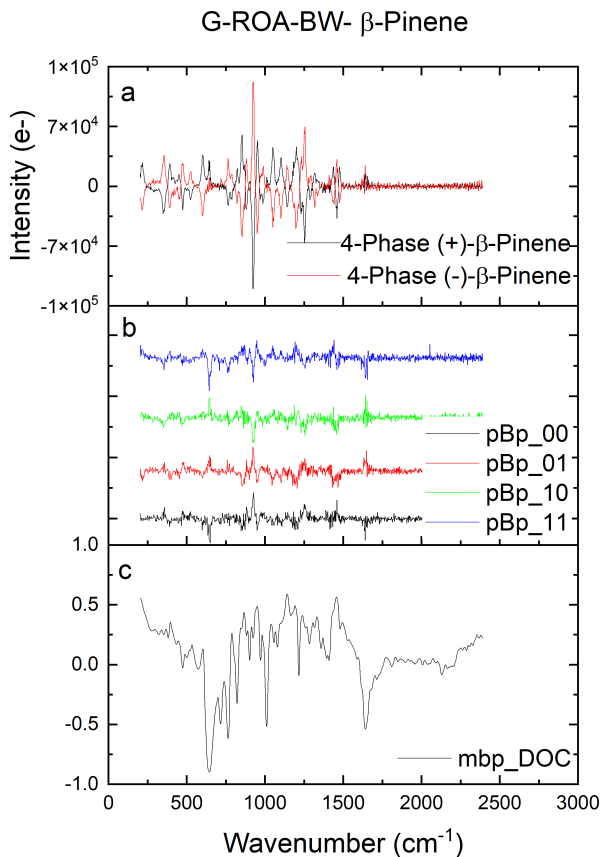
FIGURE A.20: Here spectra of each of four possible virtual enantiomers is shown for β-pinene measured with the G-ROA-BW instrument. The top panel shows the four-phase corrected spectra and the bottom panel shows the DOC for β-pinene.
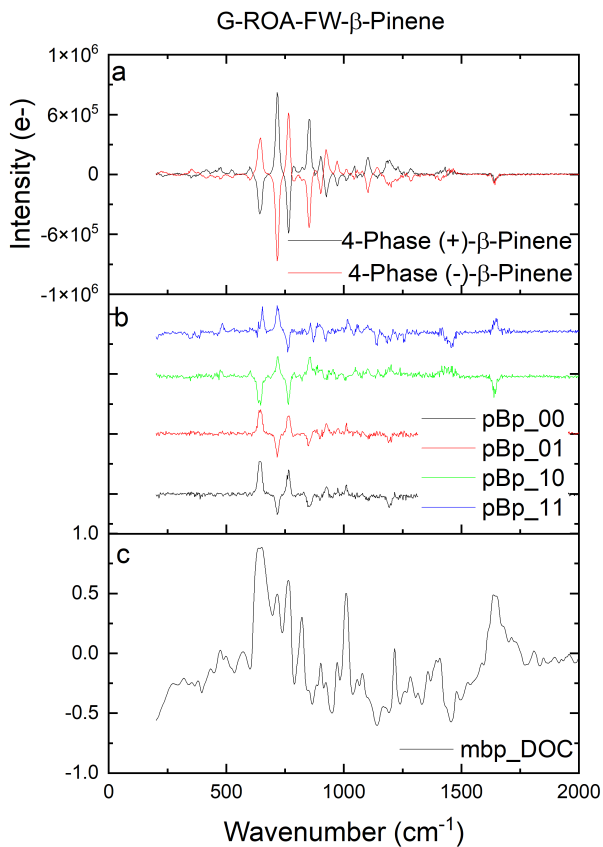
FIGURE A.21: Here spectra of each of four possible virtual enantiomers is shown for *β*-pinene measured with the A-ROA-Kym instrument. The top panel shows the four-phase corrected spectra and the bottom panel shows the DOC for *β*-pinene.

FIGURE A.22: Here spectra of each of four possible virtual enantiomers is shown for β-pinene measured with the A-ROA-Holo instrument. The top panel shows the four-phase corrected spectra and the bottom panel shows the DOC for β-pinene.
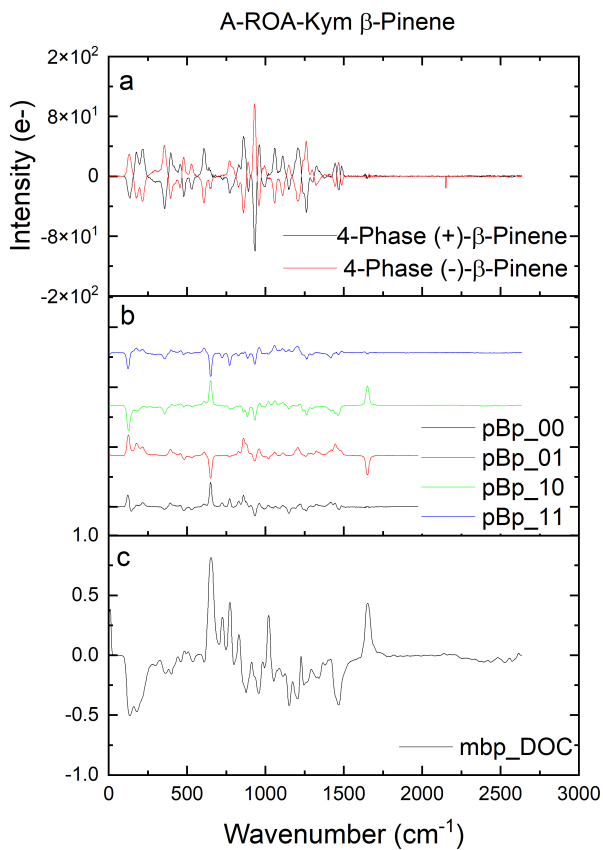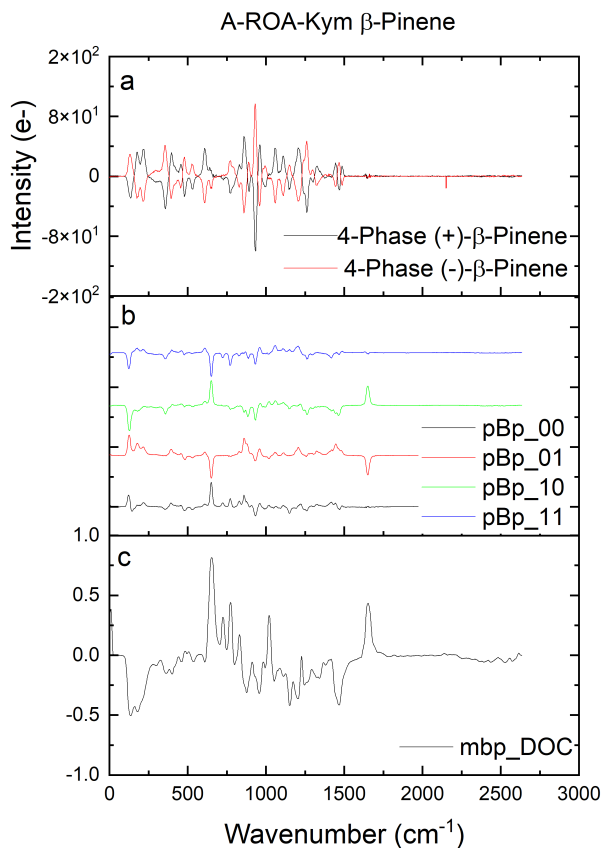
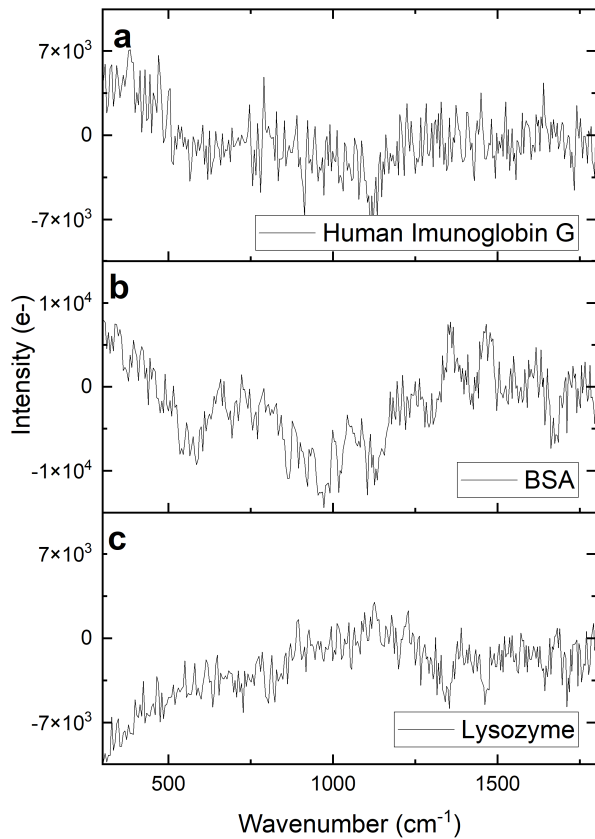## A.4   FORWARD-SCATTERED ROA OF BIOLOGICAL MOLECULES

FIGURE A.23: The raw (un-smoothed) ROA spectra of hIG, lysozyme and BSA.

A.5 HELPFUL TIPS FOR BUILDING ROA INSTRUMENTS

Though we have tried to include the vital information relating to the construction of our ROA instrument in Chapters 2 and details on control measurements in Chapter 3, there are a few other helpful tips that are too specific for a literature paper and two few for an additional thesis chapter. The list below is for those endeavoring to build a new ROA instrument, or other chiroptical set-up requiring similar precision.

1. A tool is only as precise as the best linear polarizer.

   - The linear polarizer after the laser needs to be *at least* an order-of-magnitude higher in extinction ratio than the effect you are measuring. If you are measuring an effect with dissymmetry of 10^{-2} then your polarizer needs to have an extinction ratio of at least 1:1,000.

   - Film polarizers have low damage thresholds— proceed with caution.

2. Prism polarizers are not the same as film polarizers.

   - Glan-taylor prisms have extinction ratios of 1:100,000 *only* when the incident polarization is at a specific angle to the prism. You need to put a half-wave plate before the Glan to achieve the best polarization (this will be noticeable in ROA).

   - Glan-taylor prisms and most other polarizing prisms have limited angle-of-incidence, this can lead to challenging alignment issues, make sure your laser is well aligned when going through your polarizing prism.

   - Make sure to dump the o-ray beam.

3. Laser power is often controlled via a half-wave plate and polarizer.

   - This can lead to power-dependent polarization artifacts, because the degree of polarizer varies with power.

   - If your polarizer after the laser has a high enough extinction ratio this shouldn't matter.

4. A few likely sources of polarization issues:

- **Objective lenses**, even those with "low birifringence" typically introduce too much error for use in ROA (or similarly weak effects).

- **Mirrors** almost always cause polarization issues, uncoated silver is the best but even uncoated silver mirrors need to be compensated.

- **Sample holders**, reduce strain if possible, chose amorphous materials, always control by testing with multiple sample holders.

- **The sample!** See Chapter 3.

5. A PEM and diode, connected with an oscilloscope is a useful way to hunt down polarization artifacts.

6. Yes, you do need a system to create depolarized light.

   - This is true even if you are measuring ICP. Detectors almost universally have some degree of polarization preference, a linear polarizer or rotating half-wave plate before your detector will help eliminate the impact of this.

7. Sample volume is important, and tricky when dealing with liquids.

   - Make sure to have overlapping focal points to collect from a focal volume in your liquid.

   - Different liquids have different refractive indices, which will shift your focal point.

BIBLIOGRAPHY

1. Gandorfer, A. M., Povel, H. P., Steiner, P., Aebersold, F., Egger, U., Feller, A., Gisler, D., Hagenbuch, S. & Stenflo, J. O. Solar polarimetry in the near UV with the Zurich Imaging Polarimeter ZIMPOL II. *Astronomy & Astrophysics* **422**, 703 (2004).

2. Hakonen, A., Andersson, P., Schmidt, M., Rindzevicius, T. & Käll, M. Explosive and chemical threat detection by surface-enhanced Raman scattering: A review. *Analytica Chimica Acta* **893** (2015).

3. Habartová, L., Hrubešová, K., Syslová, K., Vondroušová, J., Fišar, Z., Jirák, R., Raboch, J. & Setnička, V. Blood-based molecular signature of Alzheimer's disease via spectroscopy and metabolomics. *Clinical Biochemistry* **72**, 58 (2019).

4. Quack, M. Frontiers in spectroscopy. *Faraday Discussions* **150**, 533 (2011).

5. Long, D. A. Early history of the Raman effect. *International Reviews in Physical Chemistry* **7**, 317 (1988).

6. Barron, L. D. & Barron, L. D. *Molecular light scattering and optical activity* (2004).

7. Long, D. A. *The Raman effect* (John Wiley and Sons LTD, West Sussex, 2002).

8. Szilágyi, A. *EMANIM: Interactive visualization of electromagnetic waves* https://emanim.szialab.org.

9. Kenyon, I. *The light fantastic: a modern introduction to classical and quantum optics* (Oxford University Press, Inc., USA, 2008).

10. Collett, E. *Field guide to polarization* (SPIE—The International Society for Optical Engineering, Washington,USA, 2005).

11. Pun, A. B., Mule, A. S., Held, J. T. & Norris, D. J. Core/shell magic-sized CdSe nanocrystals. *Nano Letters* **21** (2021).

12. Miessler, G. L. *Inorganic chemistry* (Pearson Prentice Hall, New Jersey, 2003).

13. Bailey, J. Chirality and the origin of life. *Acta Astronautica* **46** (2000).

14. Hecht, L., Barron, L. D., Blanch, E. W., Bell, A. F. & Day, L. A. Raman optical activity instrument for studies of biopolymer structure and dynamics. *Journal of Raman Spectroscopy* **30**, 815 (1999).

15. Barron, L. & Buckingham, A. Rayleigh and Raman optical activity. *Annual Review of Physical Chemistry* **26**, 381 (1975).

16. Hug, W. & Hangartner, G. A novel high-throughput raman spectrometer for polarization difference measurements. *Journal of Raman Spectroscopy* **30**, 841 (1999).

17. Hug, W. Virtual enantiomers as the solution of optical activity's deterministic offset problem. *Applied Spectroscopy* **57**, 1 (2002).

18. Lightner, C. R., Gisler, D., Meyer, S. A., Niese, H., Keitel, R. C. & Norris, D. J. Measurement of Raman optical activity with high-frequency polarization modulation. *The Journal of Physical Chemistry A* **125**, 8132 (2021).

19. Poulikakos, L. V., Gutsche, P., McPeak, K. M., Burger, S., Niegemann, J., Hafner, C. & Norris, D. J. Optical chirality flux as a useful far-field probe of chiral near fields. *ACS Photonics* **3**, 1619 (2016).

20. Nafie, L. A. *Vibrational optical activity* (Wiley Online Library, Syracuse, 2011).

21. Crosby, K. W. and Hlpps G. A. Applications of the photoelastic modulator to polarization spectroscopy. *Journal of Physical Chemistry*, 555 (1979).

22. Stenflo, J. Solar polarimetry with ZIMPOL. *Memorie della Societa Astronomica Italiana*, 183 (2007).

23. Kemp, J. & Barbour, M. A photoelastic-modulator polarimeter at Pine Mountain observatory. *Publications of the Astronomical Society of the Pacific* **93**, 521 (1981).

24. Barron, L., Torrance, J. & Cutler, D. A new multichannel Raman optical activity instrument. *Journal of Raman Spectroscopy* **18**, 281 (1987).

25. Povel, H., Aebersold, H. & Stenflo, J. O. Charge-coupled device image sensor as a demodulator in a 2-D polarimeter with a piezoelastic modulator. *Applied optics* **29**, 1186 (1990).

26. Barron, L. D., Hecht, L., McColl, I. H. & Blanch, E. W. Raman optical activity comes of age. *Molecular Physics* **102**, 731 (2004).

27. Spencer, K. M., Freedman, T. B. & Nafie, L. A. Scattered circular polarization Raman optical activity. *Chemical Physics Letters* **149**, 367 (1988).

28. Hecht, L. & Barron, L. An analysis of modulation experiments for Raman optical activity. *Applied Spectroscopy* **44**, 483 (1989).

29. Hug, W. Encyclopedia of spectroscopy and spectrometry (Third Edition). *Vibrational, Rotational and Raman Spectroscopies: Article Titles: R*, 881 (2017).

30. Haesler, J. *Construction of a new forward and backward scattering Raman optical activity spectrometer and graphical analysis of measured and calculated spectra for (R)-[2H1,2H2,2H3]-Neopentane* PhD thesis (2006).

31. Barron, L., Hecht, L., Gargaro, A. & Hug, W. Vibrational raman optical activity in forward scattering: trans-pinane and -pinene. *Journal of Raman Spectroscopy* **21**, 375 (1990).

32. Ramelli, R., Balemi, S., Bianda, M., Defilippis, I., Gamma, L., Hagenbuch, S., Rogantini, M., Steiner, P. & Stenflo, J. O. ZIMPOL-3: a powerful solar polarimeter. **21**, 375 (2010).

33. Yang, N., Tang, Y. & Cohen, A. E. Spectroscopy in sculpted fields. *Nano Today* **4**, 269 (2009).

34. Tang, Y. & Cohen, A. E. Optical chirality and its interaction with matter. *Physical Review Letters* **104**, 163901 (2010).

35. Wade, J., Brandt, J., Reger, D., Zinna, F., Amsharov, K., Jux, N., Andrews, D. & Fuchter, M. J. 500-fold amplification of small molecule circularly polarized luminescence through circularly polarized FRET. *Angewandte Chemie* (2020).

36. Lindon, J., Tranter, G. & Koppenaal, D. *Encyclopedia of spectroscopy and spectrometry* (Elsevier Science, 2016).

37. Keiderling, T. A. Instrumentation for vibrational circular dichroism spectroscopy: method comparison and newer developments. *Molecules* **23**, 2404 (2018).

38. Hirschmann, M., Merten, C. & Thiele, C. M. Treating anisotropic artefacts in circular dichroism spectroscopy enables investigation of lyotropic liquid crystalline polyaspartate solutions. *Soft Matter* **17**, 2849 (2021).

39. Wilson, J. C., Gutsche, P., Herrmann, S., Burger, S. & McPeak, K. M. Correlation of circular differential optical absorption with geometric chirality in plasmonic meta-atoms. *Opt. Express* **27**, 5097 (2019).

40. Savenkov, S. N. in *Light Scattering Reviews 4: Single Light Scattering and Radiative Transfer* (ed Kokhanovsky, A. A.) 71 (Springer Berlin Heidelberg, Berlin, Heidelberg, 2009).

41. Efrima, S. The effect of large electric field gradients on the Raman optical activity of molecules adsorbed on metal surfaces. *Chemical Physics Letters* **102**, 79 (1983).

42. Abdali, S. & Blanch, E. Surface enhanced Raman optical activity (SEROA). *Chemical Society Reviews* **37**, 980 (2008).

43. Pour, S., Bell, S. E. & Blanch, E. W. Use of a hydrogel polymer for reproducible surface enhanced Raman optical activity (SEROA). *Chemical Communications* **47**, 4754 (2011).

44. Das, M., Gangopadhyay, D., Šebestík, J., Habartová, L., Michal, P., Kapitán, J. & Bouř, P. Chiral detection by induced surface-enhanced Raman optical activity. *Chemical Communications* (2021).

45. Johannessen, C., White, P. C. & Abdali, S. Resonance Raman Optical Activity and Surface Enhanced Resonance Raman Optical Activity Analysis of Cytochrome c. *The Journal of Physical Chemistry A* **111**, 7771 (2007).

46. Schlücker, S. Surface-enhanced Raman spectroscopy:concepts and chemical applications. *Angewandte Chemie International Edition* **53**. Write quick summary here: 4756 (2014).

47. Pour, S., Rocks, L., Faulds, K., Graham, D., Parchaňský, V., Bouř, P. & Blanch, E. W. Through-space transfer of chiral information mediated by a plasmonic nanomaterial. *Nature Chemistry* **7**, 591 (2015).

48. Xiao, T.-H., Cheng, Z., Luo, Z., Isozaki, A., Hiramatsu, K., Itoh, T., Nomura, M., Iwamoto, S. & Goda, K. All-dielectric chiral-field-enhanced Raman optical activity. *Nature Communications* **12**, 3062 (2021).

49. Wan, L., Wade, J., Salerno, F., Arteaga, O., Laidlaw, B., Wang, X., Penfold, T., Fuchter, M. J. & Campbell, A. J. Inverting the handedness of circularly polarized luminescence from light-emitting polymers using film thickness. *ACS Nano* **13**, 8099 (2019).

50. Ernst, K.-H. Molecular chirality at surfaces. *Physica Status Solidi (b)* **249**, 2057 (2012).

51. Fleischmann, M., Hendra, P. & McQuillan, A. Raman spectra of pyridine adsorbed at a silver electrode. *Chemical Physics Letters* **26**, 163 (1974).

52. Moskovits, M. Persistent misconceptions regarding SERS. *Physical Chemistry Chemical Physics* **15**, 5301 (2012).

53. Sidler, D., Bleiziffer, P. & Riniker, S. Beyond Rosenfeld equation: computation of vibrational circular dichroism spectra for anisotropic solutions. *Journal of Chemical Theory and Computation* (2019).

54. Ru, E. & Etchegoin, P. Rigorous justification of the |E|4 enhancement factor in Surface Enhanced Raman Spectroscopy. *Chemical Physics Letters* **423**, 63 (2006).

55. Che, D. & Nafie, L. A. Isolation of Raman optical activity invariants. *Chemical Physics Letters* **189**, 35 (1992).

56. Li, J. F., Tian, X. D., Li, S. B., Anema, J. R., Yang, Z. L., Ding, Y., Wu, Y. F., Zeng, Y. M., Chen, Q. Z., Ren, B., Wang, Z. L. & Tian, Z. Q. Surface analysis using shell-isolated nanoparticle-enhanced Raman spectroscopy. *Nature Protocols* **8**, 52 (2013).

57. Shao, Q. & Hall, C. K. Binding preferences of amino acids for gold nanoparticles: a molecular simulation study. *Langmuir* **32**, 7888 (2016).

58. Sennakesavan, G., Mostakhdemin, M., Dkhar, L., Seyfoddin, A. & Fatihhi, S. Acrylic acid/acrylamide based hydrogels and its properties - A review. *Polymer Degradation and Stability* **180**, 109308 (2020).

59. Brooks, W., Guida, W. & Daniel, K. The significance of chirality in drug design and development. *Current Topics in Medicinal Chemistry* **11**, 760 (2011).

60. Batista, A. N., Jr, J. M., Bolzani, V. S., Furlan, M. & Blanch, E. W. Selective DMSO-induced conformational changes in proteins from Raman optical activity. *Physical Chemistry Chemical Physics* **15** (2013).

61. Barron, L. D. The development of biomolecular Raman optical activity spectroscopy. *Biomedical Spectroscopy and Imaging* **4**, 223 (2015).

62. Stollar, E. J. & Smith, D. P. Uncovering protein structure. *Essays in Biochemistry* **64**, 649 (2020).

63. Diamond, R. Real-space refinement of the structure of hen egg-white lysozyme. *Journal of Molecular Biology* **82** (1974).

64. Harris, L. J., Larson, S. B., Hasel, K. W. & McPherson, A. Refined Structure of an intact IgG2a monoclonal antibody. *Biochemistry* **36**, 1581 (1997).

65. Bujacz, A. Structures of bovine, equine and leporine serum albumin. *Acta Crystallographica Section D: Biological Crystallography* **68**, 1278 (2012).

66. Mason, S. The origin of chirality in nature. *Trends in Pharmacological Sciences* **7**, 20 (1986).

67. Myrgorodska, I., Meinert, C., Martins, Z., d'Hendecourt, L. L. S. & Meierhenrich, U. J. Molecular chirality in meteorites and interstellar ices, and the chirality experiment on board the ESA cometary Rosetta mission. *Angewandte Chemie International Edition* **54**, 1402 (2015).

68. Brechbühler, R., Rabouw, F. T., Rohner, P., Feber, B. l., Poulikakos, D. & Norris, D. J. Two-dimensional Drexhage experiment for electric- and magnetic-dipole sources on plasmonic interfaces. *Physical Review Letters* **121** (2018).

CURRICULUM VITAE

PERSONAL DATA

Name	Carin R. Lightner
Date of Birth	March 6, 1991
Place of Birth	Pullman, Washington, USA
Citizen of	The United States of America

EDUCATION

ETH Zurich *D.Sc. Mechanical and Process Engineering* Feb. 2018 - June 2022
Cornell University *M.Sc. in Materials Science and Engineering* Aug. 2012 - July 2014
Iowa State University *B.Sc. in Chemical Engineering* Aug. 2008 - May 2012

EMPLOYMENT

Process Engineer at Applied Materials, Singapore
January 2016 - December 2016
Process Engineer at Applied Materials, California
April 2015 - January 2016
Engineering Intern at Evonik Industries, Germany
July 2014 - December 2014
Engineering Intern at Brueckner Maschinenbau, Germany
May 2012 - August 2012

PUBLICATIONS

First Author Papers

- Lightner, C. R.; Gisler, D.; Meyer, S. A.; Niese, H.; Keitel, R. C.; Norris, D. J. Measurement of Raman Optical Activity with High-Frequency Polarization Modulation. J Phys Chem 2021, 125 (36), 8132–8139.

Contributing Papers

- Michel, A. U.; Meyer, S.; Essing, N.; Lassaline, N.; Lightner, C. R.; Bisig, S.; Norris, D. J.; Chigrin, D. N. The Potential of Combining Thermal Scanning Probes and Phase-Change Materials for Tunable Metasurfaces. Adv Opt Mater 2021, 9 (2), 2001243.

- Lightner, C.R. ; Altun, A.O.; Park, H.G.; 2019. Molecular Sensing by SERS Using Entangled Nanofibers, in: . pp. 795–823.

- Wyss, R. M.; Parzefall, M.; Schlichting, K.-P.; Gruber, C. M.; Busschaert, S.; Lightner, C. R.; Lortscher, E.; Novotny, L.; Heeg, S. Freestanding and Permeable Nanoporous Gold Membranes for Surface-Enhanced Raman Scattering. Acs Appl Mater Inter 2022..

Patents

- Lightner, Carin; Gisler, Daniel; Norris, David; Optical Activity Measurement with Frequency Modulation, EP3907492A1

Conference Contributions and Awards:

- Young Investigator Pitch, ETH Raman Workshop 2021
- Poster Prize, ChiralMat2021, May 2021
- Awarded Talk, Seeds for CD Lecture Series, October 2020